

Table of Contents

| | |
|--|-----|
| ABSTRACT | iii |
| RÉSUMÉ..... | v |
| ACKNOWLEDGEMENT | vii |
| LIST OF FIGURES..... | xii |
| LIST OF TABLES | xvi |
| SECTION A | 1 |
| Chapter.1 | 2 |
| Introduction of Hydrogen Economy and Hydrogen storage Materials | 2 |
| 1. 1 Introduction of Hydrogen Economy | 2 |
| 1.1.1 Hydrogen Production and Storage | 3 |
| 1.2 Hydrogen Storage in Metal hydrides | 5 |
| 1.2.1 Hydrogen Storage in body centred solid solution alloys..... | 8 |
| 1.2.2 Hydrogenation characteristics of bcc alloy | 8 |
| 1.2.3 Laves phase related bcc solid solution | 10 |
| 1.3 Aim and structure of the thesis..... | 11 |
| Chapter 2 | 12 |
| Description of the Experimental Techniques used for Material Synthesis and Characterization | 12 |
| 2.1 Alloy synthesis by arc-melting..... | 12 |
| 2.2 X-ray Diffraction..... | 13 |
| 2.3 Scanning Electron Microscopy | 17 |
| 2.3.1 Secondary electron emission mode..... | 18 |
| 2.3.2 Backscattered electrons mode | 18 |
| 2.3.3 Energy Dispersive X-ray analysis | 18 |
| 2.4 Extended X-ray absorption fine structure Spectroscopy..... | 19 |
| 2.4.1 EXAFS Principle..... | 20 |
| 2.5 Sievert's type apparatus for hydrogen measurements..... | 22 |
| 2.6 Neutron Diffraction | 23 |
| Chapter 3 | 27 |

| | |
|--|----|
| Structural, microstructural and hydrogenation characteristics of Ti-V-Cr alloy added with Zr-Ni..... | 27 |
| 3.1 Introduction..... | 27 |
| 3.2 Results and discussion..... | 27 |
| 3.2.1 Morphology..... | 28 |
| 3.2.2 Crystal Structure..... | 33 |
| 3.2.3 First Hydrogenation..... | 36 |
| 3.2.4 Pressure composition temperature (PCT) | 40 |
| 3.3 Conclusions..... | 41 |
| Chapter 4 | 43 |
| Investigation of the microstructure, crystal structure and hydrogenation kinetics of Ti-V-Cr alloy with Zr addition..... | 43 |
| 4.1 Introduction..... | 43 |
| 4.2 Results and Discussion..... | 43 |
| 4.2.1 Morphology..... | 43 |
| 4.2.2 Crystal Structure..... | 49 |
| 4.2.3 First Hydrogenation..... | 51 |
| 4.2.4 Comparison between Zr and 7Zr+10Ni additive..... | 56 |
| 4.3 Conclusions..... | 57 |
| Chapter 5 | 59 |
| Neutron, and EXAFS studies of $Ti_{50}V_{20}Cr_{30}$ added with 4wt. % of 7Zr+10Ni | 59 |
| 5.1 Introduction..... | 59 |
| 5.2. Neutron study on $Ti_{50}V_{20}Cr_{30}$ | 60 |
| 5.3 Results and discussion of 50TiM and 50TiBP | 64 |
| 5.3.1Morphology of 50TiM and 50TiBP | 65 |
| 5.3.2 First Hydrogenation..... | 68 |
| 5.3.3 EXAFS | 69 |
| 5.4 Conclusions..... | 70 |
| Chapter 6 | 72 |
| Conclusion and future work | 72 |
| 6.1 Conclusion..... | 72 |

| | |
|-----------------------|-----|
| 6.2 Future work | 73 |
| SECTION B | 74 |
| Articles | 75 |
| Article 1 | 76 |
| Article 2 | 83 |
| REFERENCES:..... | 102 |

LIST OF FIGURES

| | |
|---|----|
| Fig 1.1 Pressure composition temperature (PCT isotherm)..... | 7 |
| Fig.1.2 PCT diagram of V metal..... | 9 |
| Fig 2.1 Arc-melting machine..... | 13 |
| Fig 2.2 Schematic diagram of X-ray diffractometer..... | 14 |
| Fig 2.3 The Bragg-Brentano Parafocusing Circles of a X- ray goniometer.... | 16 |
| Fig 2.4 Types of the interaction of electron beam while incident on the specimen..... | 17 |
| Fig.2.5 Schematic diagram of EXAFS..... | 19 |
| Fig.2.6 Schematic presentation of X-ray absorption spectrum..... | 20 |
| Fig 2.7 Schematic illustration of EXAFS phenomenon..... | 21 |
| Fig.2.8 Homemade Sievert's type apparatus..... | 22 |
| Fig.2.9 Different scattering length as a function of atomic weight..... | 25 |
| Fig.2.10 A schematic diagram of the constant wave length diffractometer.... | 26 |
| Fig.2.11. A schematic presentation of neutron diffraction pattern..... | 26 |
| Fig 3.1 Backscattered electron micrograph and elemental probe analysis of $Ti_xV_{70-x}Cr_{30}$ (x = 10, 20)..... | 28 |
| Fig 3.2 Backscattered electron micrograph and elemental probe analysis of $Ti_xV_{70-x}Cr_{30}$ (x = 30, 40 and 50) | 30 |

| | |
|--|----|
| Fig 3.3 Chemical analysis of the elements in Matrix (a) and Bright phase (b) with varying Ti concentration x..... | 33 |
| Fig.3.4 XRD pattern of the $Ti_xV_{70-x}Cr_{30}$ ($x = 10, 20, 30, 40, 50$) alloys with additive in (a) as-cast and (b) hydrided state..... | 34 |
| Fig.3.5 Plot of lattice parameter and average atomic radius as a function of Ti concentration (x). The straight line is a linear fit of the experimental points..... | 36 |
| Fig.3.6 Activation curve of the $Ti_xV_{70-x}Cr_{30}$ ($x = 10, 20, 30, 40, 50$) alloys with additive, under 2 MPa of hydrogen at 22 °C..... | 37 |
| Fig.3.7 Ti-content versus lattice parameter and absorption capacity of $Ti_xV_{70-x}Cr_{30}$ ($x = 10$ to 50)..... | 37 |
| Fig.3.8 Desorption PCT curves of $Ti_xV_{70-x}Cr_{30}$ ($x= 40, 50$) alloy added with 4 wt.% of 7Zr+10Ni at 150° C..... | 41 |
| Fig.4.1: Backscattered electrons micrograph of the alloys $Ti_xV_{70-x}Cr_{30}$ ($x = 10, 20, 30, 40, 50$), added with 4 wt.% of Zr..... | 44 |
| Fig.4.2: Higher magnification backscattered electrons micrograph of the alloys $Ti_xV_{70-x}Cr_{30}$ ($x = 10, 20, 30, 40, 50$), added with 4 wt.% of Zr..... | 45 |

| | |
|---|----|
| Fig.4.3. Chemical analysis of the elements in Matrix (a) and Bright phase (b) with varying Ti concentration x..... | 48 |
| Fig.4.4 XRD pattern of $Ti_xV_{70-x}Cr_{30}$ ($x = 10$ to 50) alloys added with 4 wt.% of Zr in (a) as-cast and (b) hydride state..... | 49 |
| Fig.4.5: Lattice parameter and average atomic radius of bcc phase as a function of Ti-content (x)..... | 51 |
| Fig.4.6. Activation curve of the $Ti_xV_{70-x}Cr_{30}$ ($x = 10, 20, 30, 40, 50$) alloys added with 4 wt.% of Zr, under 20 bar of hydrogen at $22\text{ }^{\circ}C$ | 52 |
| Fig 4.7: For $Ti_xV_{70-x}Cr_{30}$ ($x = 20$ to 50) alloy, volume of hydrogen atom in fcc phase..... | 55 |
| Fig.4.8: First hydrogenation kinetics of $Ti_{40}V_{30}Cr_{30}$ alloy (a) without additive (b) with 4 wt.% of Zr (c) with 4 wt.% of 7Zr+10Ni, under 20 bar of hydrogen at $22\text{ }^{\circ}C$ | 57 |
| Fig.5.1: Desorption neutron diffraction pattern of fully deuterated $Ti_{50}V_{20}Cr_{30}$ alloy | 63 |
| Fig.5.2 Relation between (a) fcc lattice parameter, D-occupancy versus temperature (b) Al cell parameter versus temperature..... | 64 |

| | |
|---|----|
| Fig.5.3: Backscattered electron micrographs of 50TiM (a) and 50TiBP (b) | 65 |
| | |
| Fig.5.4: Activations curves of the 50TiBP and 50TiM, under 20 bars of hydrogen at 22 °C..... | 69 |
| Fig.5.5: EXAFS spectra at Ti K edge for the 50TiBP in as-cast hydrogenated and desorbed state. (a) Normalized EXAFS spectra (b) R space oscillations... | 70 |

LIST OF TABLES

| | |
|---|----|
| Table 1.1 Combustion and explosion properties of hydrogen, methane and gasoline fuels..... | 3 |
| Table 1.2: Hydrogen storage technologies..... | 4 |
| Table 3.1 Nominal and measured atomic percentage of the as-cast sample $Ti_{10}V_{60}Cr_{30}$. Error on the measured values is ± 0.5 at.% | 29 |
| Table 3.2 Nominal and measured atomic percentage of the as-cast sample $Ti_{20}V_{50}Cr_{30}$. Error on the measured values is ± 0.5 at.%..... | 29 |
| Table 3.3 Nominal and measured atomic percentage of the as-cast sample $Ti_{30}V_{40}Cr_{30}$. Error on the measured values is ± 0.5 at.%..... | 31 |
| Table 3.4 Nominal and measured atomic percentage of the as-cast sample $Ti_{40}V_{30}Cr_{30}$. Error on the measured values is ± 0.5 at.%..... | 31 |
| Table 3.5 Nominal and measured atomic percentage of the as-cast sample $Ti_{50}V_{20}Cr_{30}$. Error on the measured values is ± 0.5 at.%..... | 32 |
| Table.3.6 Percentage of the observed phases for the alloy $Ti_xV_{70-x}Cr_{30}$ ($x = 10$ to 50), added with $7Zr+10Ni$, as calculated by Image j. Number in parentheses is the uncertainty on the last significant digit..... | 32 |
| Table.3.7 Crystal parameters of the $Ti_xV_{70-x}Cr_{30}$ ($x = 10$ to 50) alloys in as-cast state. Number in parentheses is the uncertainties on the last significant digit..... | 35 |
| Table.3.8 Crystal parameters of the $Ti_xV_{70-x}Cr_{30}$ ($x = 10$ to 50) alloys in hydrided state. Number in parentheses is the uncertainties on the last significant digit..... | 38 |

| | |
|---|----|
| Table.3.9 Calculated and experimentally obtained storage capacity of each alloy. Number in parentheses is the uncertainties on the last significant digit.. | 40 |
| Table 4.1: Percentage of the observed phases for the alloy $Ti_xV_{70-x}Cr_{30}$ ($x=10$ to 50) added with 4 wt.% of Zr, as determined by imagej. Error on the measured values is ± 0.5 at.%. For inhomogeneous phases, the higher/lower values are indicated..... | 45 |
| Table 4.2: Nominal and measured atomic percentage of the as-cast samples $Ti_{10}V_{60}Cr_{30}$ added with 4 wt.% of Zr. Error on measured value is ± 0.5 at.%.. | 46 |
| Table 4.3: Nominal and measured atomic percentage of the as-cast samples $Ti_{20}V_{50}Cr_{30}$ added with 4 wt.% of Zr. Error on measured value is ± 0.5 at.%.. | 46 |
| Table 4.4: Nominal and measured atomic percentage of the as-cast samples $Ti_{30}V_{40}Cr_{30}$ added with 4 wt.% of Zr. Error on measured value is ± 0.5 at.%... | 47 |
| Table 4.5: Nominal and measured atomic percentage of the as-cast samples $Ti_{40}V_{30}Cr_{30}$ added with 4 wt.% of Zr. Error on measured value is ± 0.5 at.%.. | 47 |
| Table 4.6: Nominal and measured atomic percentage of the as-cast samples $Ti_{50}V_{20}Cr_{30}$ added with 4 wt.% of Zr. Error on measured value is ± 0.5 at.%.. | 48 |
| Table 4.7: Crystal parameters of $Ti_xV_{70-x}Cr_{30}$ ($x = 10$ to 50) alloy added with 4 wt.% of Zr. Number in the parenthesis is the error on the last significant digit..... | 50 |
| Table 4.8: Crystal parameter of $Ti_xV_{70-x}Cr_{30}$ ($x = 10$ to 50) alloy added with 4 wt.% of Zr in hydride state. Numbers in parentheses is the error on the last significant digit..... | 53 |
| Table 5.1: Average scattering length of the different phases of $Ti_{50}V_{20}Cr_{30}$... | 60 |

| | |
|---|----|
| Table 5.2 Nominal and measured atomic percentage of the 50TiM. Error on the measured values is ± 0.5 | 66 |
| Table 5.3 Nominal and measured atomic percentage of the 50TiBP. Error on the measured values is ± 0.5 | 67 |
| Table.5.4 Percentage of the observed phases for the alloy 50TiM and 50TiBP, as calculated by Image j. Number in parentheses is the uncertainty on the last significant digit..... | 67 |

SECTION A

Chapter.1

Introduction of Hydrogen Economy and Hydrogen storage Materials

1. 1 Introduction of Hydrogen Economy

Constant use of hydrocarbon fuels is responsible, to a large extent, for air pollution and global warming. Hydrogen as an energy vector is a promising way to solve these environmental issues [1]. It could be used in conjunction with renewable energies, mainly solar and wind. Transportation and storage of these energy sources is a problem which could be solved by using hydrogen as energy storage and/or energy vector [2]. Hydrogen has a wide range of other utilization in the energy field such as in heat storage, isotope separation, Ni-MH batteries, heat actuators, etc .

Hydrogen is colourless, tasteless, odourless, nontoxic, nonmetallic and highly combustible diatomic gas at ambient temperature and pressure[1]. Hydrogen is the most abundant element in the universe but on the earth, hydrogen exists only in molecular form such as water and molecular compound. It should thus be extracted from these compounds in some way. Combustion and explosion properties of hydrogen are compared with the methane and gasoline fuels in table 1.1[3]. It can be seen from the table that hydrogen has very small density (0.084 kg/m^3) compared to the other natural gases. It means that to store only 1 kg of hydrogen at ambient pressure, a volume of 11.9 m^3 is required. Hydrogen has very low critical temperature ($T_c = 30.0\text{K}$), high diffusivity, wide range of flammability and high burning velocity compared to other natural gases[3]. Hydrogen combustion is completely carbon free and gives a gravimetric energy density between 120 MJ/kg and 142 MJ/kg which is three times higher than the gravimetric energy density of petroleum [4]. Hydrogen ignition energy is only 0.017 mJ for mixtures with air, which is smaller than the other hydrocarbon fuels, but the flame temperature of hydrogen and other fuels is very similar.

| Properties | Hydrogen | Methane | Gasoline |
|--|----------|---------|-------------------------------|
| Density [kg/m^3] (STP) | 0.084 | 0.65 | 4.4 (1000kPa & 15.5 °C) |
| Diffusion coefficient [cm^2/s] | 0.61 | 0.16 | 0.05 |
| Flammability limit in air [vol%] | 4-75 | 5.3-15 | 1-7.6 |
| Minimum energy for ignition in air [mj] | 0.02 | 0.29 | 0.24 |
| Maximum burning velocity in air [m/s] | 3.46 | 0.45 | 1.76 |
| Flame temp in air [k] | 2318 | 2148 | 2470 |

Table 1.1 Combustion and explosion properties of hydrogen, methane and gasoline fuels.

1.1.1 Hydrogen Production and Storage

There are several methods to produce hydrogen such as: electrolysis and thermolysis but currently the method mostly used by the industry is steam reforming [5]. Natural gases are the cheapest source for hydrogen production, but the major byproducts of this process are CO_2 , CO and other greenhouse gasses. Hydrogen production by electrolysis method is a clean means of production but it consumes a huge amount of electricity which is itself a big issue.

On the other hand, due to the low hydrogen density (0.089 gm/l), hydrogen storage is also an important challenge. There are presently three main techniques for hydrogen storage: high pressure, cryogenics and solid state [1]. These technologies are reported in table 1.2 with their typical operating temperature and pressure [3].

| Technology | Mass (%) | Operating temperature (°C) | Pressure (bar) | Hydrogen density (Kg/m ³) |
|---|----------|----------------------------|----------------|---------------------------------------|
| High-pressure cylinder | 13 | 25 | 100 | 33 |
| Liquid hydrogen | 100 | -252 | 1 | 70 |
| High surface area material | 2-5 | -196 | 15-50 | 20 |
| Low temperature metal hydrides (LaNi ₅ H ₆) | 2 | 25 | 2-9 | 99 |
| High temperature metal hydrides (Mg ₂ FeH ₆) | 7 | ~300 | 2-10 | 150 |
| Complex hydride | 18 | >100 | 1 | 150 |

Table 1.2: Hydrogen storage technologies

High pressure storage method is presently the most commonly used method. The conventional steel cylinders are operated at maximum 200 bar pressure. For mobile applications, their size and weight make them impractical [6]. However, light weight composite gas cylinders have been developed and are now used in mobile applications. They can sustain up to 700 bars of pressure, but they are more expensive than the conventional steel cylinders.

For the cryogenic storage, very low temperature (<-253°C) and super insulating containers are required which makes this method very expensive. However, this is the method used to transport large quantities of hydrogen over long distances when hydrogen pipeline is not available.

Hydrogen storage in solid state materials is a promising and convenient way to replace high pressure and cryogenic storage [1]. There are two different routes for the solid-state hydrogen storage. The first is in which molecular hydrogen interacts with the

surface of the material with the weak Van der Waals force (physisorption) and the second is in which chemical interaction (chemisorption) of the atomic hydrogen takes place with simple or complex metallic alloys. Physisorption or adsorption is a surface phenomenon which occurs at very low temperature (-195 °C). This type of interaction leads to the low adsorption enthalpy which lies between 1 and 10 kJ/mol. The main focus of this thesis being on chemisorption, the following discussion will be limited to this storage technique.

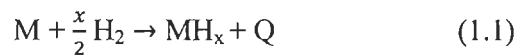
1.2 Hydrogen Storage in Metal hydrides

Metal hydrides have been studied for several applications such as for gas separation and purification, temperature sensing, thermal compression, and refrigeration. However, the main application for metal hydrides is hydrogen storage [7-9]. Depending upon the bonding between hydrogen and metal atom, hydrides are classified as ionic hydride, covalent hydride and metallic hydrides [10]. Most of the hydrides studied for hydrogen storage are metallic hydrides [11]. In metallic hydrides, hydrogen atoms interact with metal atoms and make a metallic bond.

1.2.1 Thermodynamics of Metal Hydrides or Pressure composition

Temperature (PCT)

Many metals and alloys react with hydrogen according to the following schematic reaction:



Here M is a metal, solid solution alloy or intermetallic compound, MH_x is a hydride, x is the metal to hydrogen ratio and Q is the heat of the reaction[10].

When a metal is in contact with hydrogen, the hydrogen molecule firstly interacts with the surface through weak Van-der Waals interaction which is known as the physisorption phenomenon. In the case of metal hydride formation, hydrogen overcomes the activation barrier and molecular hydrogen dissociate into hydrogen atoms. After this dissociation, the hydrogen atom diffuses into the bulk and makes M-H (metal hydrogen) solid

solution which is known as the α phase. This is schematically represented in figure 1.1. With increasing pressure, the hydrogen concentration increases and at the plateau pressure there is nucleation of the hydride phase. This phase is usually called the β phase. In the plateau region α and β phases coexist, and the length of this plateau region gives us information about the reversible capacity of the hydride. At the plateau region, the total number of phases are three (α , β and hydrogen gas) and total number of components are two (metal and hydrogen). Phase formation in metal hydride system can be understood by the Gibb's phase rule which is:

$$F = C - P + 2 \quad (1.2)$$

where, F is the degree of freedom, C is the number of components and P is the number of phases.

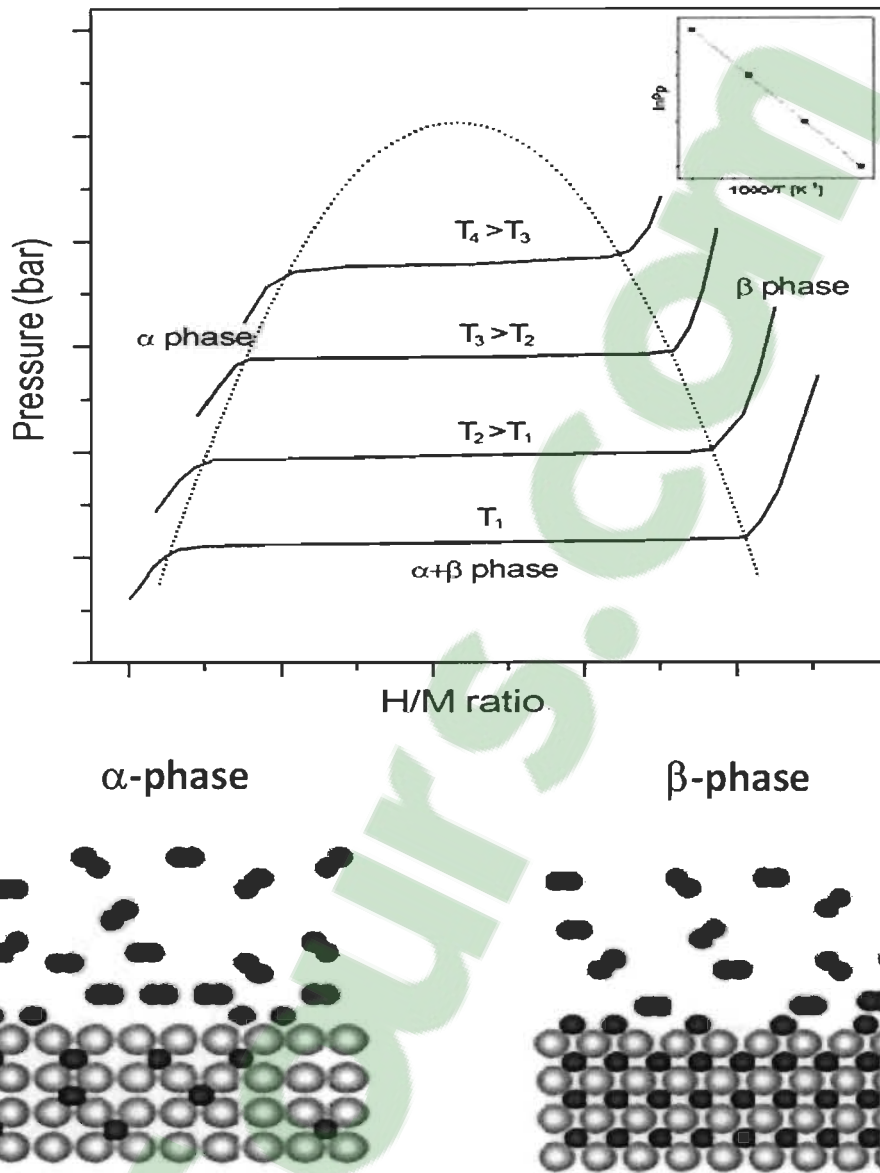


Fig 1.1 Pressure composition temperature (PCT isotherm)

Referring to figure 1.1 and according to the Gibb's rule when the α and β phases coexist there is just one degree of freedom thus giving a plateau region in the pressure-composition diagram. In α and β regions, the total degree of freedom is 2. Therefore, in these regions, hydrogen concentration rises with increasing hydrogen pressure.

As the temperature increases, the plateau pressure of the hydride also increases and at a certain temperature the plateau region completely disappears. This temperature is known as the critical temperature of the hydride. Therefore below the critical temperature, by taking the middle point of the plateau region of each isotherm a graph $\ln P_{eq}$ versus $1/T$ can be plotted. This graph is known as Van't Hoff plot by which enthalpy ΔH and entropy ΔS of the hydride are calculated. According to the Van't Hoff law [10]:

$$\ln P_{eq} = \frac{\Delta H}{RT} - \frac{\Delta S}{R} \quad (1.3)$$

Here enthalpy and entropy are the slope and intercept of the straight line plotting $\ln P_{eq}$ versus $1/T$ [10]. P_{eq} is the equilibrium hydrogen pressure, T is the thermodynamic temperature and R is the gas constant (8.3145 J/K mol).

1.2.1 Hydrogen Storage in body centred solid solution alloys

A solid solution alloy is formed by dissolving the one or more solute elements into a solvent element [12]. For solid solution formation, it is not necessary to have a stoichiometric or near stoichiometric alloy composition.

For hydrogen storage applications, various compositional solid solution alloys such as Pd, Ti and Zr based alloys have been studied [13-17]. In 1982, Ono et.al reported the hydrogen absorption properties of Ti-V solid solution alloy [18]. They measured the pressure composition temperature (PCT) curve of $Ti_{0.4}V_{0.6}$ alloy and observed that this alloy took a very long time to attain the equilibrium pressure [19]. This measurement emphasized on the slow reaction rate of this alloy. Therefore, due to their slow reaction rate, Ti-V-based alloy was not found suitable for practical application. In 1988, Libowitz and Maeland investigated the effect of the addition of transition elements (Fe, Mn, Cr, Co, Ni) in Ti-V-based alloy and observed that addition of a third element improves the hydrogenation kinetics [20, 21].

1.2.2 Hydrogenation characteristics of bcc alloy

Generally in the PCT isotherm of body centred metal and alloys, two plateaus are present [10]. As an example, the pressure composition isotherm of vanadium is shown in

figure 1.2 [19]. Vanadium shows two plateaus at two different equilibrium pressure [19]. Equilibrium pressure of the first plateau, corresponding to the monohydride, is 0.1 Pa at 80 °C as seen in figure 1.2 (a) [22]. The second plateau which is due to the formation of the dihydride is at much higher pressure; for example, 2 MPa at 78 °C as shown in figure 1.2 (b) [22].

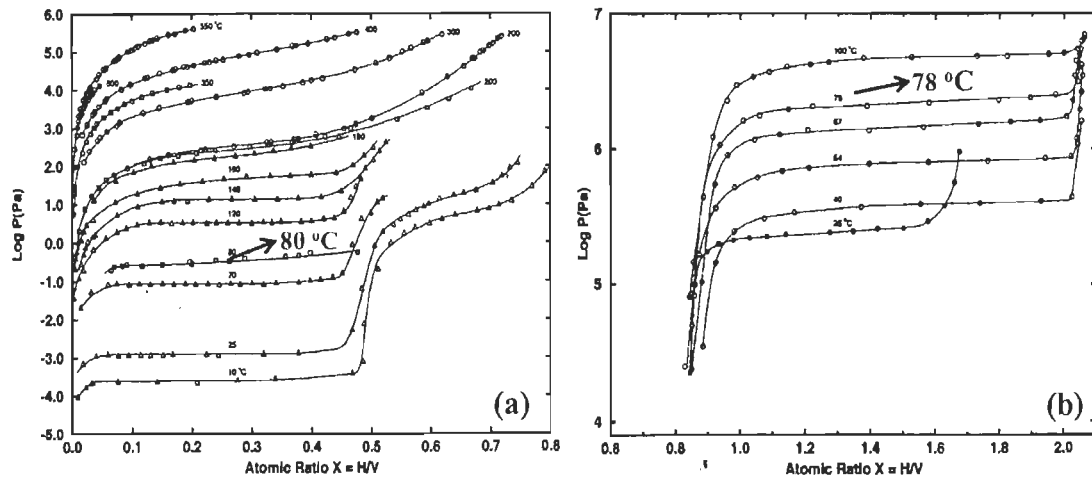


Fig.1.2 PCT diagram of V metal.

As the plateau of the monohydride phase is usually at a pressure much lower than one bar, this makes it impossible to desorb in most practical applications. The dihydride plateau is at much higher pressure and this phase could be desorbed under a few bars of hydrogen pressure. Reversible capacity is defined by the capacity that could be absorbed and desorbed under the operational conditions of the hydride tank. Therefore, two plateaus in PCT are undesirable.

Besides two plateaus in PCT, difficulty in first hydrogenation (activation) is also an important problem with these alloys. Generally, the surface of the alloy is covered by an oxide layer. During the activation, hydrogen has to break the oxide layer to be absorbed in the bulk of the alloy [23]. To solve the activation problem, heat treatment between 300 and 750 °C is usually required for bcc alloys which is not desirable for practical applications [24, 25].

For utilization of bcc alloys for hydrogen storage, the destabilization of the monohydride (in order to improve the reversible capacity) and making the activation possible at room temperature are two important aspects that have to be improved.

1.2.3 Laves phase related bcc solid solution

In 1995 Tsukahara et al. studied the V-based multi-phase alloys to make the electrodes for Ni-metal hydride batteries and observed different phases for the different alloy composition [26-29]. For $\text{TiV}_3\text{Ni}_{0.56}\text{Hf}_x$, ($x = 0.046, 0.24$) alloy they observed the presence of bcc phase with C14 laves phase [28]. They found that the combined effect of bcc and C14 laves phases was helpful to obtain higher electrode capacity.

Iba and Akiba in 1997 reported that alloys having a bcc solid solution phase along with Laves phases are very promising for hydrogen storage and they named these kind of bcc phase 'Laves phase related bcc solid solution' to distinguish them from simple bcc phase that is observed in Ti-V system [19]. In their study, they found that Ti-V-Cr alloys have smaller hysteresis than Ti-V-Mn alloys which makes them more suitable for the practical application [19].

It was reported that Ti-V-Cr alloys absorb up to 3.7 wt.% of hydrogen, but their reversible capacity is around 2.4 wt.% [18, 30, 31]. In order to see the effect of additional phase on sorption kinetics of bcc alloy, Miraglia et al. remelted Ti-V-Cr bcc alloy with 4 wt.% of $\text{Zr}_7\text{Ni}_{10}$ [23]. They reported that due to the addition of $\text{Zr}_7\text{Ni}_{10}$, a secondary phase was formed which made the activation possible without prior heat treatment.

Activation kinetics and storage capacity are also affected by the differences in chemical composition. Many groups have studied the effect of different elementary composition on the hydrogenation characteristics of bcc alloys and reported that variation in chemical composition has a direct effect on the plateau pressure and sorption kinetics [19, 31-33]. Yu et al. studied the effect of V-content in Ti-V-Cr-Mn alloy [34]. They found that a higher proportion of vanadium increased the hydrogen capacity, but this made the first hydrogenation much slower.

1.3 Aim and structure of the thesis

The main objective of the thesis is to understand the effect of 7Zr+10Ni and Zr, additives on the microstructure and hydrogen storage properties of Ti-V-Cr alloy. Another objective of this thesis is to study the effect of Ti/V ratio on the hydrogen capacity and first hydrogenation behaviour. The reason for changing the Ti/V ratio is that vanadium is an expensive element. Thus, it is advisable to optimize the Ti/V ratio to obtain the highest hydrogen capacity for the lowest possible vanadium content.

The thesis is made of five chapters. In this first chapter the introduction and basic idea of the research were given. In the second chapter, details of all the experimental techniques are reported. In the third chapter, the effect of 7Zr+10Ni on $Ti_xV_{70-x}Cr_{30}$ is discussed. In the fourth chapter, the effect of the addition of Zr on Ti-V-Cr alloy is shown. In the fifth chapter neutron, and EXAFS studies on $Ti_{50}V_{20}Cr_{30}$ alloy added with 4wt.% of 7Zr+10Ni are reported.

Chapter 2

Description of the Experimental Techniques used for Material Synthesis and Characterization

This chapter presents all the experimental techniques that have been used for material synthesis and characterization. Namely:

- (i) Arc melting for the synthesis of the Ti-V-Cr alloys.
- (ii) X-ray diffraction for the characterization of the crystal structure of the alloys.
- (iii) Scanning Electron Microscopy (SEM) and associated Energy Dispersive Spectroscopy (EDS) for the microstructure and elemental composition of the alloys.
- (iv) Extended X-ray Absorption Fine Structure spectroscopy (EXAFS) used to determine the local atomic structure of the alloy .
- (vi) Sievert's type apparatus for measuring the hydrogenation properties.
- (vii) Neutron diffraction for the phase identification and localization of hydrogen in the crystal structure.

2.1 Alloy synthesis by arc-melting

All raw elements Ti (99.9%), V (99.7%), Cr (99%), Zr (99.2%) and Ni (99.9 %) were purchased from Alfa-Aesar. All syntheses were done by mixing the raw elements in the desired proportion and melting them together.

Arc-melting is a technique which is used in laboratories and industries for alloy synthesis. In order to melt the alloy, heat is produced by generating an electric arc between a tungsten electrode and a copper crucible. Initially, all the raw elements are placed on the water chilled copper crucible, then the chamber is evacuated and refilled by the argon. This process is repeated three times to remove all air from the melting chamber.



Fig 2.1 Arc-melting machine

After the final evacuation, a partial pressure of 0.7 bar of argon is established in the melting chamber. To generate the arc, the tungsten electrode is kept very close to the sample. Once the arc is generated, tungsten electrodes moved up and down to melt all parts of the sample. This gives high enough temperature to melt the metals and form an alloy. For the Ti-V-Cr alloys, a current of 45 amperes was used. After melting, when the melted alloy is solidified, it is turned over and remelted. This process is repeated three times to make a homogeneous alloy. Figure 2.1 shows the picture of the arc-melting apparatus.

2.2 X-ray Diffraction

X-ray diffraction is used to study the crystal structure of the alloys. For the present study, we used a Bruker D8 Focus X-ray diffractometer having a Bragg-Brentano configuration and with CuK_α ($\lambda_\alpha = 1.54 \text{ \AA}$) radiation. The crystal structure parameters were evaluated from Rietveld refinement by using Topas software [35]. A schematic diagram of the X-ray goniometer is shown in figure 2.2.

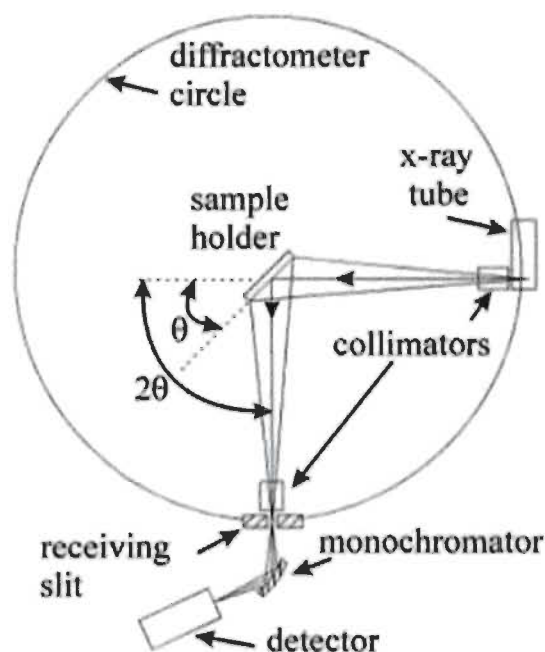


Fig 2.2 Schematic diagram of the X-ray diffractometer

Figure 2.2 shows the main components of a X-ray diffractometer : X-ray tube for production of X-ray; slits in order to collimate the X-ray beam; monochromator; to select the wavelength; sample holder; X-ray detector [36]. In the X-ray tube, a tungsten filament and a metal target are arranged in such a way that the metal target is maintained at ground potential and the tungsten filament at negatively high potential. When the tungsten filament is heated up by the filament current a stream of electrons are emitted from the filament and accelerated towards the target [37]. These electrons hit the metal target and produce X-ray. Most of the kinetic energy of the electrons is transformed into heat. Therefore, to prevent the metal target from melting, cold water circulation is used. X-ray produced in the X-ray tube contains strong K_{α} line with weak K_{β} line. This K_{β} component is undesirable and to decrease the intensity of this component relative to the K_{α} , a filter is used. The filter material is usually in the form of foil. Choice of the filter depends on the metal target. For Cu metal target, a Ni filter is used.

For the diffraction phenomenon, X-ray beam incident on the sample, interact with the electron cloud surrounding the atom and are scattered. These scattered X-rays have definite phase relationship due to the periodic arrangement of atoms on the lattice [37].

These phase relations will produce constructive and destructive interference. If the path difference between the two successive waves is integral multiples of the wavelength then constructive interference take place and a diffraction peak is observed. Diffraction condition or Bragg's law is:

$$2d_{hkl} \sin \theta = n\lambda,$$

where d is the interplanar spacing of hkl planes, λ is the wavelength and n is an integer number.

Powder diffractometers using the Bragg-Brentano parafocusing geometry gives well-defined diffraction angles. The Bragg-Brentano parafocusing geometry is shown in figure 2.3. In this geometry, sample and a point detector move in such a way that the sample is always at θ and detector is always at 2θ to the incident X-ray. Incident and the diffracted beam move on a circle that is centred on the sample. In figure 2.3, X-ray source is denoted by **S**, detector is denoted by **D** and the centre of the goniometer circle is denoted by **O**. All these three points lie on a circle known as parafocusing circle and is denoted by green dashed lines in the figure. The goniometer circle is indicated by the black dotted lines on which the detector moves. The goniometer circle has a fixed radius R but the radius of parafocusing circle varies from $R/2$ to ∞ .

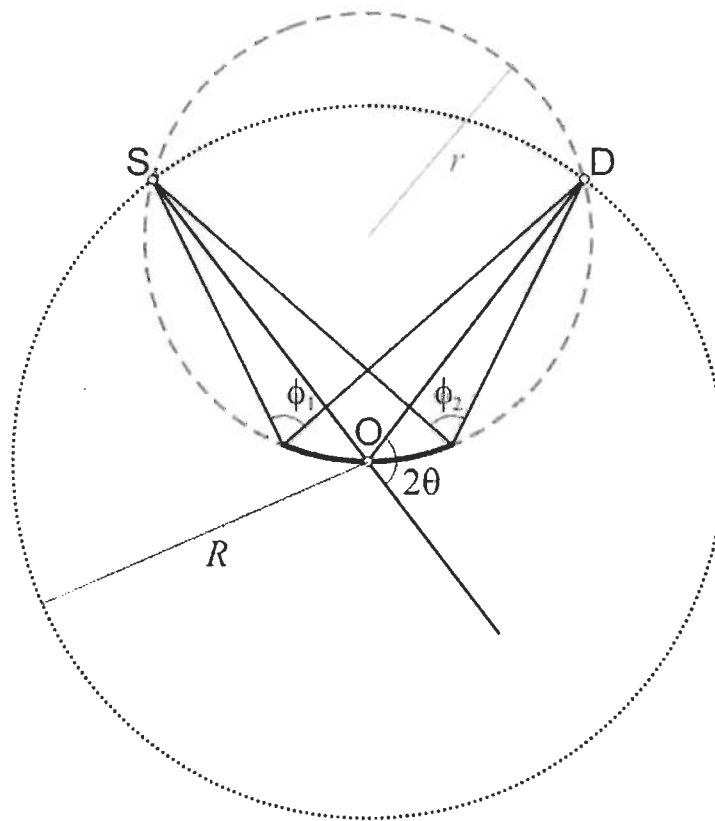


Fig 2.3 The Bragg-Brentano Parafocusing Circles of a X-ray goniometer

Owing to this geometrical arrangement, incident and diffracted X-rays (diffracted from any point of the sample surface by 2θ) will refocus exactly at the same point **D**.

$$\phi_1 = \phi_2 = 180 - 2\theta$$

In this figure a curved sample holder is shown but in practice flat sample holder is used. That's why diffracted beams do not focus perfectly and create asymmetric broadening towards the low 2θ angles in the diffraction pattern.

2.3 Scanning Electron Microscopy

In a Scanning electron microscope (SEM) a highly focused electron beam is used to scan the sample surface. When the high-energy electron beam is incident on the sample, then different interactions take place, which gives different information about the sample such as morphology and chemical composition. These various electron-sample interactions are schematically shown in figure 2.4.

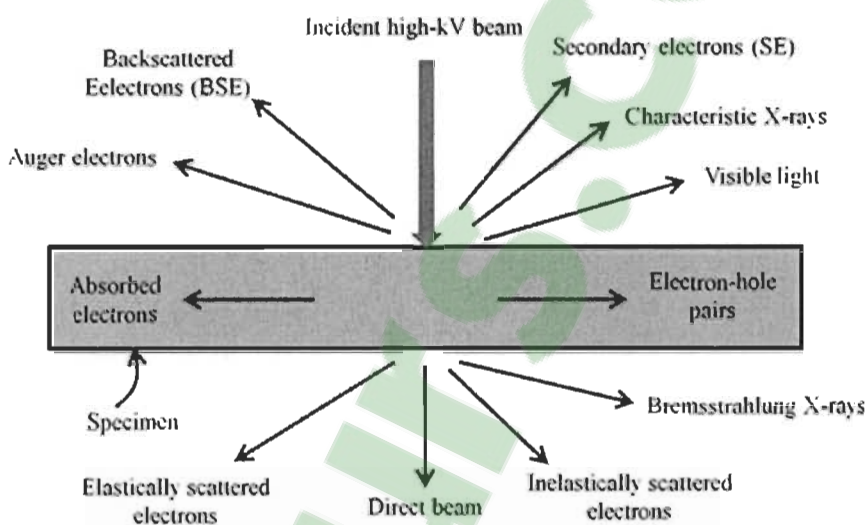


Fig 2.4 Types of the interaction of the electron beam with the specimen

In SEM, an electron beam of energy 5 to 30 keV is bombarded on the target sample [38]. This incidental electron beam participates in various types of scatterings with bound electrons and lattice. These scatterings are known as elastic and inelastic scattering of electrons which are shown in figure 2.4. In the inelastic scattering, incident electrons lose their energy after interacting with the atoms of material's surface. This energy loss is a function of the distance travelled by the electron and dependent on the property of the target material [38]. Inelastic scattering causes the production of secondary electrons. On the other hand, in the case of elastic scattering, electrons are deflected by the atomic nuclei and a very small amount of energy transfer takes place. The energy transfer is minimal because the mass of the nucleus is larger than the mass of the electron.

Therefore elastic scattering is a scattering in which incident electron is deflected by the attractive force (without significant energy loss) by passing close to the positively charged nucleus [38]. Due to the elastic scattering, backscattered electrons are produced. In the present study, JEOL JSM-5500 scanning microscopy has been used in which EDS (Energy Dispersive Spectroscopy from Oxford Instruments) apparatus was attached for the chemical analysis.

2.3.1 Secondary electron emission mode

Secondary electron mode is most commonly used in SEM. Secondary electrons have very low energy compared to back scattered electrons (few electron volts). The number of the secondary electrons produced per incident electron is defined by the secondary electron coefficient δ [38]. These secondary electrons are detected and gives the high-resolution image of the sample surface.

2.3.2 Backscattered electrons mode

The number of the backscattered electrons reaching to the detector is directly proportional to the atomic number of the atom. This mode is helpful for obtaining high resolution compositional maps.

2.3.3 Energy Dispersive X-ray analysis

Energy dispersive X-ray analysis (EDS) is used for chemical characterization. This technique identifies the elements present in the sample and also gives information about their relative abundance. For this analysis, high energy electrons are bombarded on the target sample. These incident electrons interact with the electron shell bound to the nucleus and eject them from the shell. Ejection of the electron create a hole in the inner shell and to fill this vacancy an electron from the higher energy shell jump into the lower energy shell by emitting the energy equal to the energy difference between these two energy levels. This energy is emitted in the form of X-ray which is known as the characteristic X-ray. Energies of these X-rays are detected by the energy dispersive X-ray spectrometer. Each element has a unique set of energy levels, which means that

energy of the X-ray produced by the transition from higher to lower level will be different for different elements.

2.4 Extended X-ray absorption fine structure Spectroscopy

For the present study, EXAFS measurements have been done on HXMA (Hard X-ray Micro-Analysis) 061D-1 beam line at Canadian Light Source (Saskatoon, Canada). All the experiments have been run on transmission mode. For the EXAFS data analysis winxas software has been used [39]. Extended X-ray absorption fine structure spectroscopy (EXAFS) is used to determine the bond length, coordination number and local atomic structure of a material. A schematic diagram of EXAFS is shown in figure 2.5 [40].

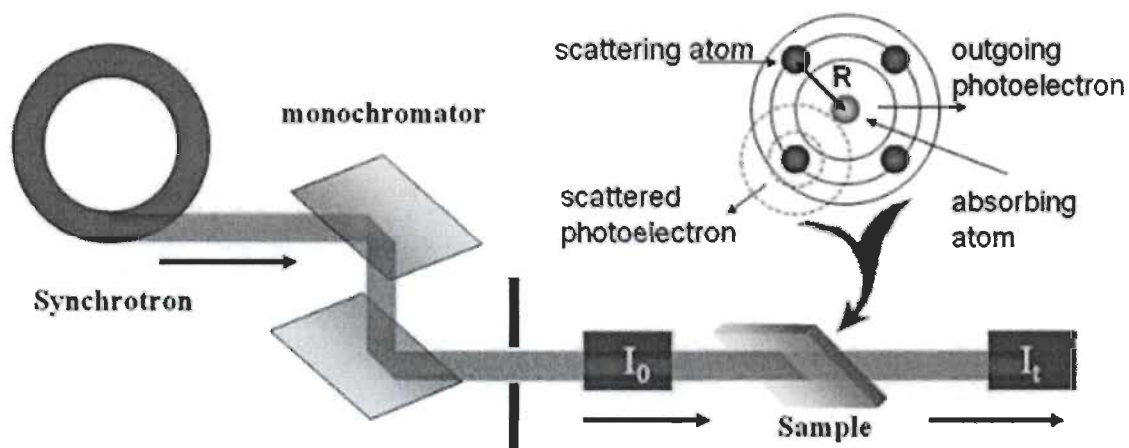


Fig.2.5 Schematic diagram of EXAFS

As seen from the figure, in EXAFS set up, synchrotron light source produces a broad X-ray spectrum, a monochromator is used to select X-ray of a particular energy. X-ray beam of definite energy is then incident on the target sample. Some of the incidental X-rays are absorbed by the atom of the target material in which excitation or ejection of the core electron takes place [41]. This X-ray absorption is determined by comparing the intensity of the incident (I_0) and transmitted (I_t) beam. This process is repeated with X-ray of slightly different energy. A schematic of the X-ray absorption spectrum is shown in figure 2.6 [42].

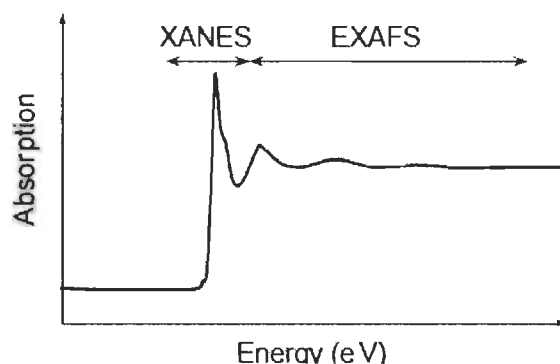


Fig.2.6 Schematic presentation of X-ray absorption spectrum

In this figure, x-axis is the energy of the incident X-ray photon and y-axis is the absorption of the X-ray by the sample. The sharp rise in the spectra is known as edge, the peaks and shoulders near the edge are known as X-ray absorption near edge structure (XANES) and gradual oscillation above the edge is known as EXAFS.

2.4.1 EXAFS Principle

EXAFS is an interference phenomenon between the emitted and the backscattered photo electron wave. Its schematic illustration is shown in figure 2.7. The X-ray photon of energy E is incident on the sample and if this energy is greater than the binding energy of core electron (E_0) then the absorption of this photon generates a photo-electron of energy $E-E_0$ [41]. This emitted photo-electron is backscattered by the neighbouring scattering atoms and interference phenomenon takes place between emitted and backscattered photoelectron waves. If this interference is constructive then the wave function increases and if destructive then the wave function decreases.

According to the de Broglie relation;

$$\lambda = h / p \dots\dots(2.1)$$

Where h is the plank constant, λ is the wavelength and p is the momentum of the photo-electron.

Energy of the photoelectron is related to the momentum by the kinetic energy equation:

$$E = p^2 / 2m \dots\dots(2.2)$$

Combining equations (2.1) and (2.2), the wavelength of the photoelectron is:

$$\lambda = h / (2mE)^{1/2} \dots\dots(2.3)$$

The energy of the ejected photoelectron is $E-E_0$. Therefore, the wavelength of the ejected photoelectron will be;

$$\lambda = h / [2m (E - E_0)]^{1/2} \dots\dots\dots(2.4)$$

When the photoelectron is backscattered from many scattering atoms then it is called multiple scattering and when it is scattered from only one atom then it is called single scattering.

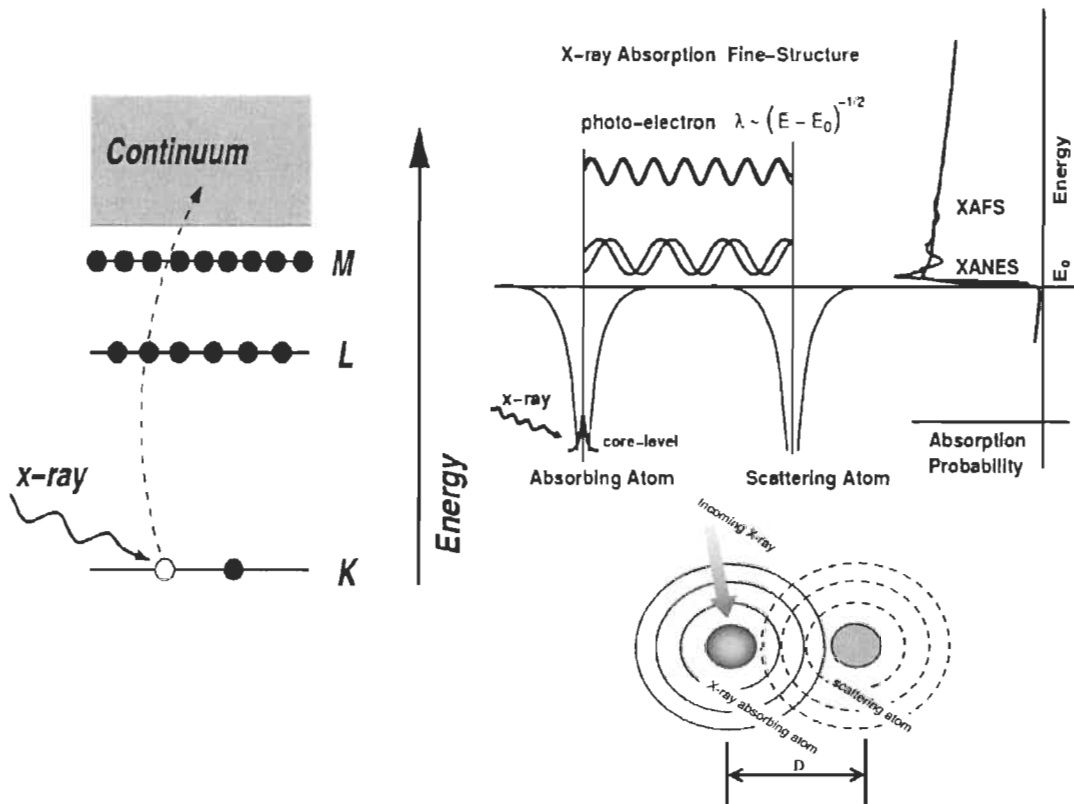


Fig 2.7 Schematic illustration of EXAFS phenomena

In the case of a single scattering, D is defined as the distance between absorbing and scattering atom but in multiple scattering, the photoelectron goes back and forth from the

absorber to the scatter atoms so in that case D is defined as half of the total distance travelled by the photoelectron [41].

As seen from the fig.2.7, constructive and destructive interference phenomenon causes the oscillation in EXAFS. Amplitude of these oscillations is proportional to the number of scattering atoms which gives information of coordination number.

EXAFS region is related to only oscillatory part of the X-ray absorption spectrum therefore, background is subtracted from the spectrum and this yield is symbolized by the oscillatory factor $\chi(E)$ [41]. It is generally convenient to understand EXAFS in terms of photo-electron wavenumber (k) ($1/\text{\AA}$ unit), rather than X-ray energy. Therefore, $\chi(E)$ is converted into the $\chi(k)$, then Fourier's transformation gives us R-space fitting. R-space fitting helps us to know the radial distance or the bond length between two atoms.

2.5 Sievert's type apparatus for hydrogen measurements

Sievert's is a common technique which is used to measure the hydrogen uptake from the gas phase to the solid host [43]. For the present study of hydrogen storage, a home-made volumetric Sievert's type apparatus has been used. This apparatus is designed with several operational modes like absorption-desorption kinetics, pressure composition isotherms and kinetic ramp desorption. A picture of the machine is shown in figure 2.8.

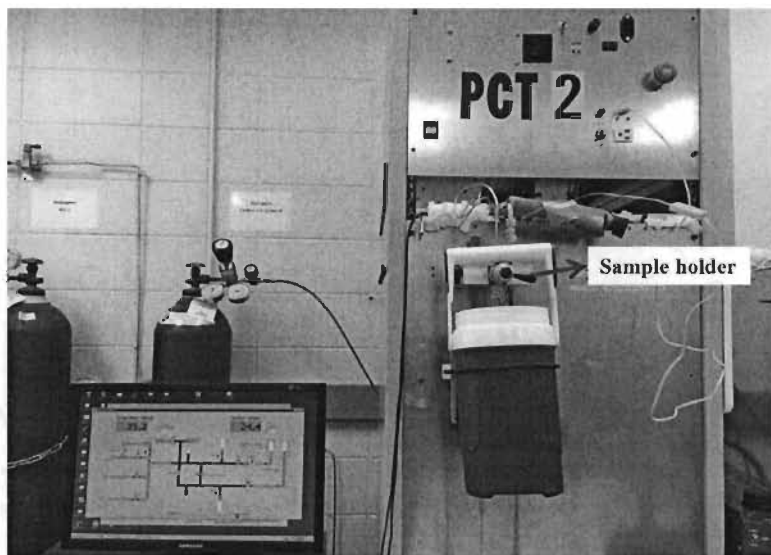


Fig.2.8 Homemade Sievert's type apparatus

In this apparatus there is a calibrated reference chamber and a sample holder where the sample is kept. The whole apparatus is designed with pressure gauges, connecting tubes and pipe lines. The absorbed amount of the gas is calculated by the pressure changes during absorption or desorption. The amount of the gas molecule in given volume can be calculated by using the virial expansion of the real gas law:

$$PV/RT = 1 + B(T) \frac{1}{V} + C(T) \frac{1}{V^2} + D(T) \frac{1}{V^3} + \dots(2.5)$$

Where P is the gas pressure, V is molar volume and R is the gas constant.

B(T), C(T) and D(T) are the temperature dependent second, third and fourth virial coefficients. Equation (2.5) can be simplified by considering only second order coefficient,

$$PV = R.T + B.P \dots\dots\dots (2.6)$$

$$\text{Since, } V = V/n$$

Therefore,

$$V = n (R.T + B.P)/P \dots\dots(2.7)$$

The number of moles of hydrogen absorbed or desorbed by the alloy is then,

$$n = 2.\Delta P. V / RT \dots\dots(2.8)$$

The factor 2 is because of the dihydrogen. Here, V is the total volume of the tube and sample holder which is constant.

2.6 Neutron Diffraction

In the present study, neutron diffraction has been performed at Delft University of Technology, Netherlands. For the neutron data refinement, the GSAS II software was used [44].

X-ray diffraction is commonly used to study the crystal structure of alloys, but this technique has some limitation. Specifically, for metal hydrides, X-ray cannot locate the

hydrogen atom in metal lattice. This is because X-ray interacts with the electron clouds of the atom and as hydrogen is a one electron atom its diffracting power is negligible compared to the other atoms in the alloy or hydride. Neutron powder diffraction is essentially the only technique that could locate the hydrogen atom in the lattice [45]. Therefore, for the better understanding of our alloys, neutron powder diffraction has been used.

Fundamentally, XRD and neutron diffraction both follows the Bragg's law which is:

$$2d_{hkl} \sin\theta = n\lambda$$

(where λ is the wave length of the radiation, d is the interplanar spacing of hkl planes and θ is the Bragg's angle.)

Neutron scattering is a quantum mechanics phenomenon which takes place due to the interaction between the incident neutron and the nucleus of the atom.

Neutrons interact with the nucleus via the short-range nuclear forces. This interaction is characterized by a scattering length (b). It can be seen from the figure 2.9 that most of the elements and their isotopes have positive b but some of them have negative b . If the scattering length is positive, it means neutrons are subjected to repulsive potential and if negative it means neutrons are subjected to an attractive potential.

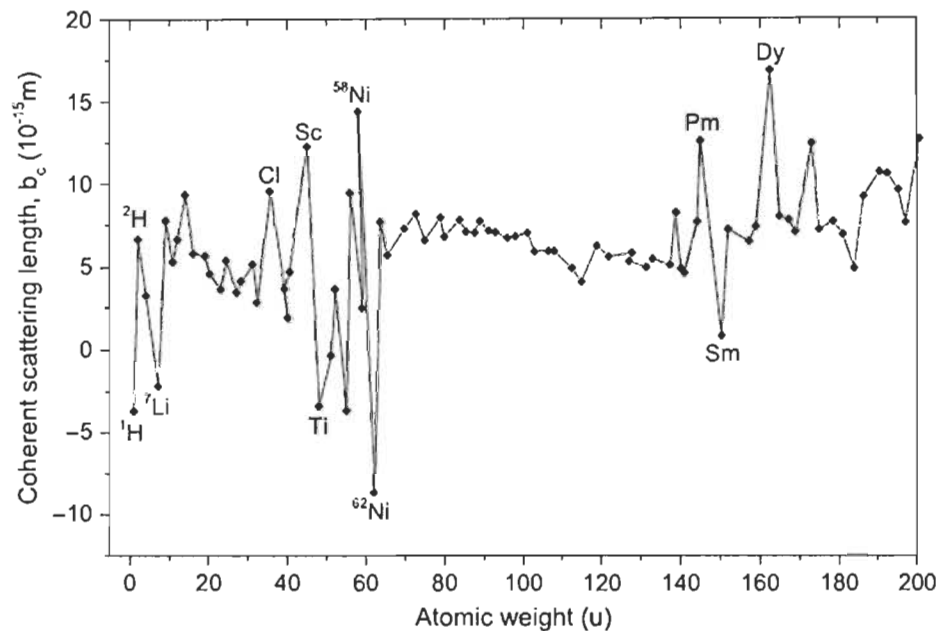


Fig.2.9 Different scattering length as a function of atomic weight

A schematic diagram of a constant wavelength diffractometer is shown in figure 2.10 [45]. For the neutron diffraction experiment, a constant wavelength diffractometer is attached to a neutron source. In the neutron source, due to the thermal fission, U^{235} split into the two dissimilar mass and produces neutrons. Produced neutrons are thermalized by the moderators. These thermal neutrons of energy 0.04 eV enter into the flight tube where they are collimated and then strike a single crystal monochromator. After diffraction from the monochromator, all of these neutrons enter into another flight tube and other collimators. Collimated neutrons are then diffracted by the sample. A neutron detector and beam stop are other parts of the diffractometer. Beam stop ensure that no direct neutron beam is entering into the detector. Signal appears in the detector only when the Bragg's condition is satisfied.

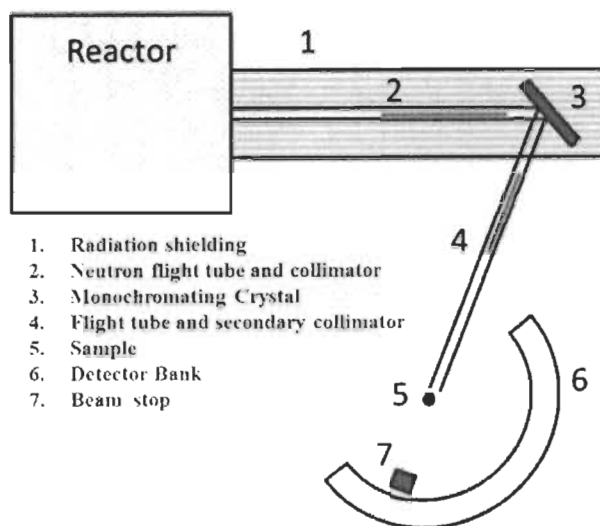


Fig.2.10 A schematic diagram of the constant wave length diffractometer

A schematic presentation of neutron diffraction pattern is shown in figure 2.11. The recorded neutron diffraction pattern is analyzed by the Rietveld refinement which is based on least-square algorithm [45]. By the Rietveld refinement of neutron pattern, crystal parameters (crystallite size, lattice parameter, microstrain), thermal parameters and atomic parameters (position and site occupancy of atoms) can be determined.

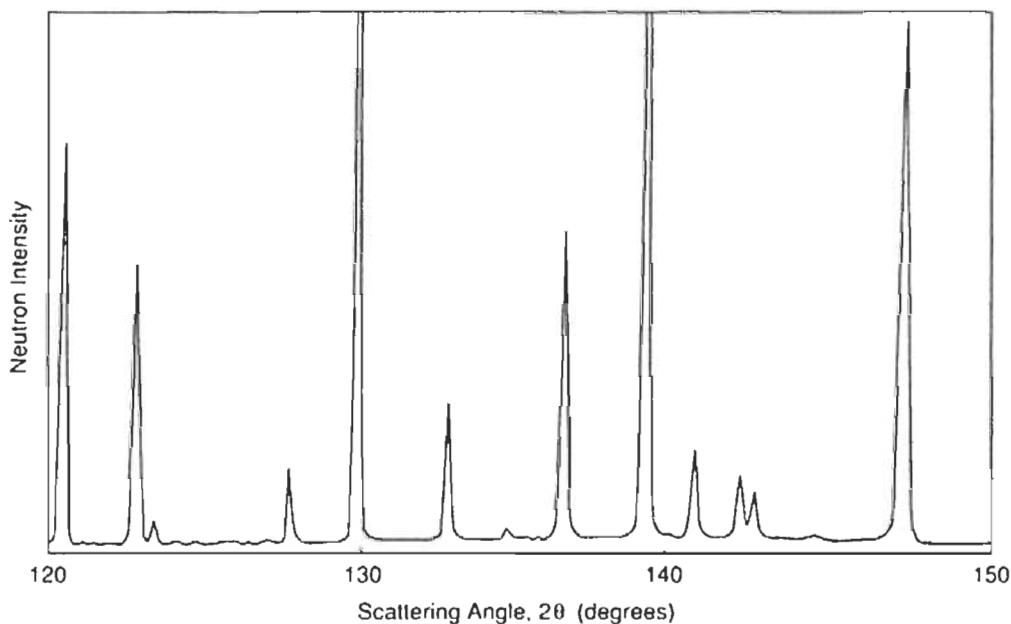


Fig.2.11. A schematic presentation of neutron diffraction pattern

Chapter 3

Structural, microstructural and hydrogenation characteristics of Ti-V-Cr alloy added with Zr-Ni

3.1 Introduction

Similarly to most metal hydrides, the first hydrogenation of bcc alloys is difficult. The main reason is the presence of oxide at the surface. Usually the way to improve the first hydrogenation and break the surface oxide is to expose the alloy to high temperature and hydrogen pressure. But this solution is time consuming and impractical for many applications. In order to improve the first hydrogenation kinetics of bcc alloys, Miraglia et al. added Zr_7Ni_{10} to Ti-V-Cr alloy [23]. They found that addition of Zr_7Ni_{10} resulted in a microstructure with a Zr and Ni-rich secondary phase that made the activation possible without prior heat treatment [23]. In this chapter, we report the effect of the addition of 7Zr+10Ni on crystal structure, microstructure and hydrogenation kinetics of $Ti_xV_{70-x}Cr_{30}$ ($x = 10$ to 50) alloy. Besides this, effect of Ti/V proportion was also investigated, and the results are shown in this chapter.

In this work, a different alloy synthesis method than the one used by Miraglia et al. [23] is used. Miraglia et al. synthesized the bcc and Zr_7Ni_{10} alloy separately and afterward, the desired proportion of these alloys was mixed and remelted [23]. Therefore, they performed three different melting for each alloy. In the present work, all the raw elements were mixed in the desired proportions and melted together. Thus, only one melt was done for each alloy. To distinguish our method to the one used by Miraglia et al. the additive name is written as 7Zr+10Ni.

3.2 Results and discussion

In this section, detailed analysis of SEM, XRD and crystal structure of $Ti_xV_{70-x}Cr_{30}$ ($x = 10, 20, 30, 40, 50$) alloy added with 4 wt.% of 7Zr+10Ni are reported. Scanning electron microscopy showed that all alloys were multiphase. X-ray powder diffraction confirmed

the body-centred cubic (bcc) phase as the main phase for the as-cast alloys. Upon hydrogenation, the bcc phase transformed into a face-centred cubic (fcc) phase. For $x = 20, 30$ and 40 a body-centred tetragonal (bct) phase was found along with fcc phase. Hydrogenation kinetics revealed that absorption kinetics improves with increasing Ti proportion. A detailed presentation of these results is shown below.

3.2.1 Morphology

Microstructure of alloys $x = 10$ and 20 are shown in fig.3.1. It can be seen that four phases are present in these alloys: a matrix and three phases with different shades of grey thereafter called, bright, grayish and black.

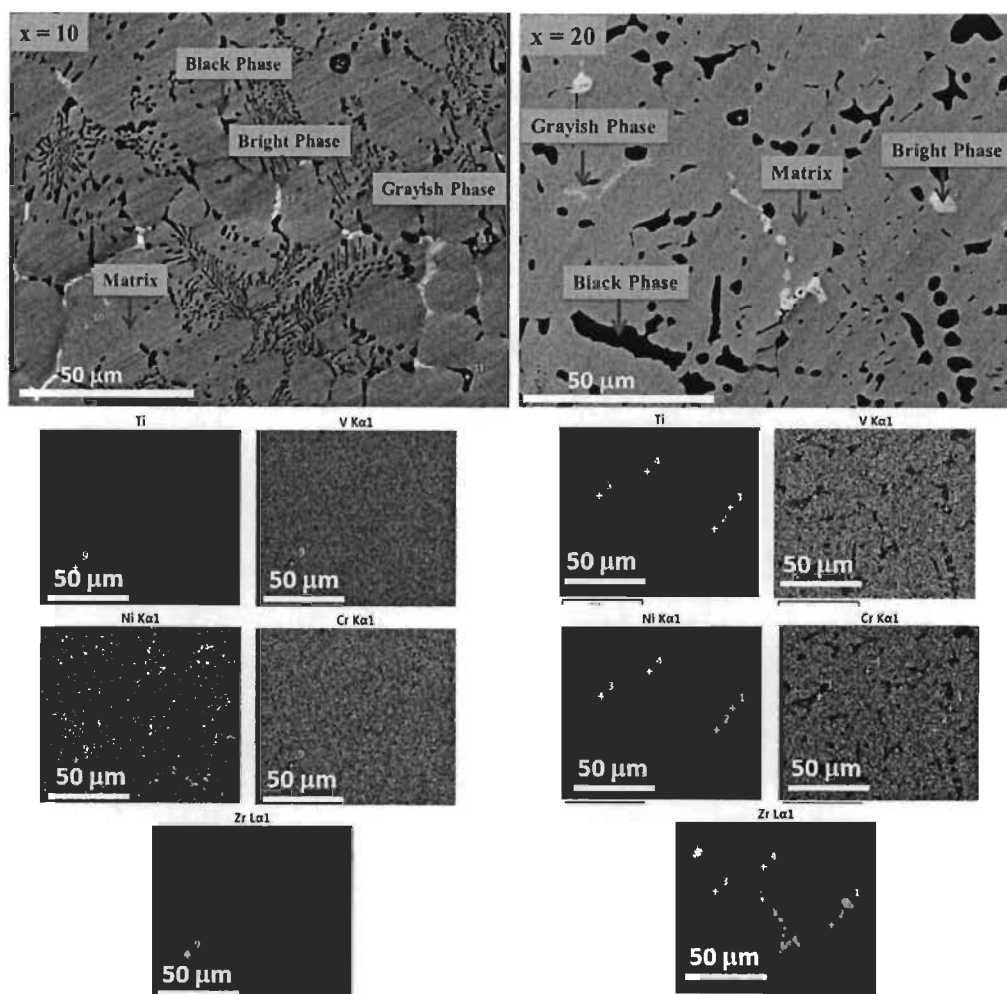


Fig 3.1 Backscattered electron micrograph and elemental probe analysis of Ti_xV_{70-x}Cr₃₀ ($x = 10, 20$)

Elemental composition of observed phases has been studied by EDS. Table 3.1 shows the elemental analysis of alloy $x = 10$. It is clear from the table that matrix phase composition is similar to the bulk nominal value. The bright phase has 60 % of Zr. Nickel concentration is higher in the grayish phase and the black phase is essentially titanium.

| Elements | Bulk nominal value | Matrix | Bright phase | Grayish phase | Black phase |
|----------|--------------------|--------|--------------|---------------|-------------|
| Ti | 9.7 | 7.9 | 7.6 | 32.2 | 92.8 |
| V | 58.2 | 60.1 | 19.2 | 9.3 | 5.4 |
| Cr | 29.3 | 29.1 | 8.1 | 2.9 | 0.9 |
| Zr | 1.1 | 1.1 | 62.9 | 15.4 | 0.8 |
| Ni | 1.6 | 1.6 | 2.2 | 40.2 | -- |

Table 3.1 Nominal and measured atomic percentage of the as-cast sample $Ti_{10}V_{60}Cr_{30}$. Error on the measured values is ± 0.5 at.%.

Table 3.2 is showing the elemental analysis of alloy $x = 20$. The general features of the different phases are similar to the previous case, but the chemical composition slightly differs for the same phase in the two alloys. Clearly both the alloys, $x = 10$ and 20 have a discrepancy in the chemical composition of bright and grayish phases.

| Elements | Bulk nominal value | Matrix | Bright phase | Grayish phase | Black phase |
|----------|--------------------|--------|--------------|---------------|-------------|
| Ti | 19.4 | 18.7 | 8.8 | 29.6 | 93.1 |
| V | 48.6 | 48.3 | 3.9 | 13.4 | 5.2 |
| Cr | 29.2 | 30.1 | 2.1 | 7.8 | 0.8 |
| Zr | 1.1 | 1.1 | 85.2 | 36.4 | 0.9 |
| Ni | 1.6 | 1.8 | -- | 12.8 | -- |

Table 3.2 Nominal and measured atomic percentage of the as-cast sample $Ti_{20}V_{50}Cr_{30}$. Error on the measured values is ± 0.5 at.%.

Figure 3.2 is showing the backscattered electron micrographs of alloys $x = 30, 40$ and 50 . Each of these alloys has three phases: matrix phase, bright and black phase. The grayish phase observed in the alloys $x = 10$ and 20 is not present in these compositions.

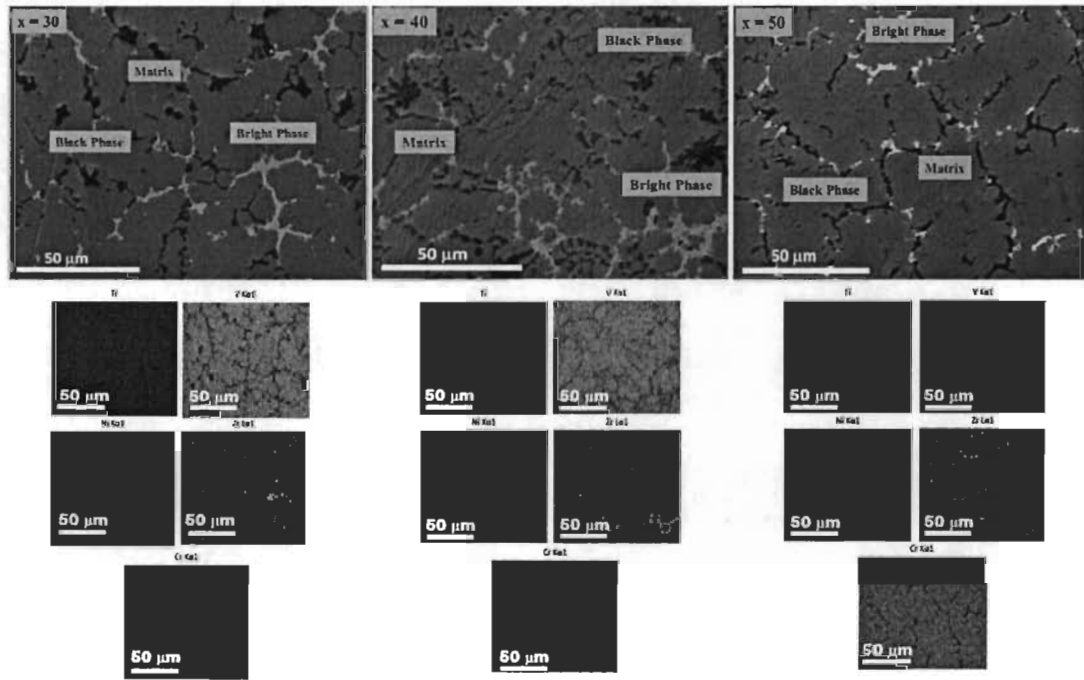


Fig 3.2 Backscattered electron micrograph and elemental probe analysis of $Ti_xV_{70-x}Cr_{30}$ ($x = 30, 40$ and 50)

In order to see the elemental composition of the phases, EDS analysis was done. The results for the alloys $x = 30, 40$ and 50 are shown in tables 3.3, 3.4 and 3.5 respectively.

Table 3.3 is showing the EDS analysis for $x = 30$ alloy. The matrix phase has a composition similar to the bulk nominal value and the black phase is essentially titanium precipitates. In the bright phase, titanium has the highest concentration and all other elements have similar concentrations.

| Elements | Bulk nominal value | Matrix | Bright phase | Black phase |
|----------|--------------------|--------|--------------|-------------|
| Ti | 29.2 | 28.2 | 37.1 | 92.1 |
| V | 38.8 | 38.3 | 14.8 | 5.1 |
| Cr | 29.2 | 31.1 | 15.8 | 0.6 |
| Zr | 1.1 | 1.3 | 15.2 | 2.2 |
| Ni | 1.6 | 1.1 | 17.1 | -- |

Table 3.3 Nominal and measured atomic percentage of the as-cast sample $Ti_{30}V_{40}Cr_{30}$. Error on the measured values is ± 0.5 at.%.

Table 3.4 is presenting the chemical analysis of $x = 40$ alloy. The situation is similar to the previous case except that in the bright phase chromium has a slightly higher concentration and vanadium a lower concentration compared to $x = 30$ alloy.

| Elements | Bulk nominal value | Matrix | Bright phase | Black phase |
|----------|--------------------|--------|--------------|-------------|
| Ti | 38.8 | 40.1 | 39.4 | 91.6 |
| V | 29.2 | 29.5 | 11.8 | 4.8 |
| Cr | 29.2 | 27.3 | 20.4 | 1.4 |
| Zr | 1.1 | 1.3 | 13.1 | 2.2 |
| Ni | 1.6 | 1.7 | 15.3 | -- |

Table 3.4 Nominal and measured atomic percentage of the as-cast sample $Ti_{40}V_{30}Cr_{30}$. Error on the measured values is ± 0.5 at.%.

EDS analysis of alloy $x = 50$ is reported in table 3.5. Like the above cases, the matrix phase has a composition close to the nominal one and the black phase is titanium precipitate. The composition of the bright phase is found different than in the previous cases. Here, titanium is found as the most abundant element, but the concentration of vanadium is found lower. The other three elements have shown similar concentrations.

| Elements | Bulk nominal value | Matrix | Bright phase | Black phase |
|----------|--------------------|--------|--------------|-------------|
| Ti | 48.6 | 49.3 | 46.1 | 78.2 |
| V | 19.4 | 19.2 | 7.2 | 8.1 |
| Cr | 29.2 | 28.5 | 17.4 | 10.3 |
| Zr | 1.1 | 1.3 | 14.4 | 3.4 |
| Ni | 1.6 | 1.7 | 14.6 | -- |

Table 3.5 Nominal and measured atomic percentage of the as-cast sample $Ti_{50}V_{20}Cr_{30}$. Error on the measured values is ± 0.5 at.%.

On the basis of SEM figure and EDS analysis it is clear that varying elemental concentration affects the microstructure and phase chemical composition of the alloy. Phase abundance of each phase of each alloy is reported in table 3.6. It shows that, for all alloys, the matrix phase is by far the most abundant and constitutes the bulk of the alloys. The next most abundant phase is the black precipitates with abundances from 6 to 15 %. The bright and grayish phases are only marginally present.

| Alloy | Matrix (%) | Bright phase (%) | Grayish Phase (%) | Black Phase (%) |
|------------------------|------------|------------------|-------------------|-----------------|
| $Ti_{10}V_{60}Cr_{30}$ | 83(2) | 0.4(2) | 0.8(5) | 15(1) |
| $Ti_{20}V_{50}Cr_{30}$ | 85(2) | 0.2(2) | 2.4(5) | 13(1) |
| $T_{30}V_{40}Cr_{30}$ | 84(2) | 6(1) | | 9(1) |
| $Ti_{40}V_{30}Cr_{30}$ | 81(2) | 7(1) | | 12(1) |
| $Ti_{50}V_{20}Cr_{30}$ | 88(2) | 4(1) | | 6(1) |

Table.3.6 Percentage of the observed phases for the alloy $Ti_xV_{70-x}Cr_{30}$ ($x = 10$ to 50), added with $7Zr+10Ni$, as calculated by Image j. Number in parentheses is the uncertainty on the last significant digit.

A better representation of matrix and bright phases for each alloy can be seen in figure 3.3 (a) and (b) respectively.

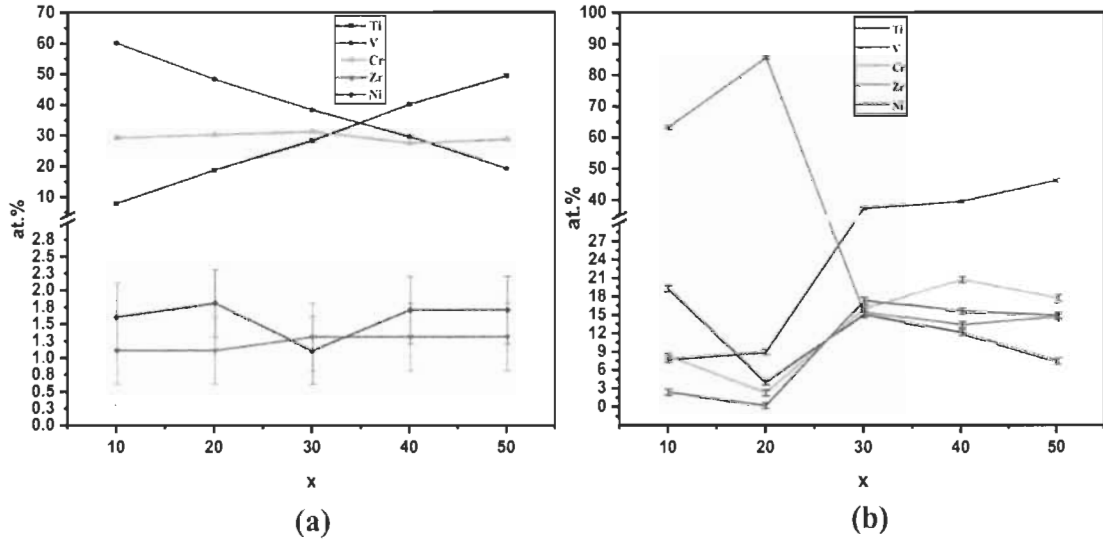


Fig 3.3 Chemical analysis of the elements in Matrix (a) and Bright phase (b) with varying Ti concentration x.

Fig.3.3 (a) shows that in the matrix phase proportion of Ti and V changes towards the higher x value while Cr, Zr and Ni are almost constant for all the x values (x= 10 to 50). This follows the nominal compositions.

From fig 3.3 (b), it is clearly visible that in the bright phase there is a drastic variation in the elemental composition from x = 10 to 30 but after that it seems to stabilize for x = 40 and 50.

3.2.2 Crystal Structure

SEM and EDS determined the morphology and phase composition of $Ti_xV_{70-x}Cr_{30}$ (x = 10 to 50) alloy. In order to study the crystal structure of as cast and hydrided alloys, X-ray diffraction was performed. Fig. 3.4(a) and (b) shows the powder diffraction patterns of as cast and hydrided alloys respectively. It is clear from the fig 3.4(a) that all the as cast alloys have body centred cubic (bcc) structure. In the diffraction pattern of x = 30 and 40, small peaks belonging to another phase are seen. They most likely belong to the

black phase (Ti-rich phase) which was the second most abundant phase seen in the microstructure of these alloys. Table 3.6 shows that alloys 10 and 20, have higher abundance of black phase compared to the alloy $x=30$ and 40. In spite of that, Ti phase was not observed in the X-ray pattern of these alloys. This could be due to the small crystallite size of Ti-phase in alloy $x = 10$ and 20.

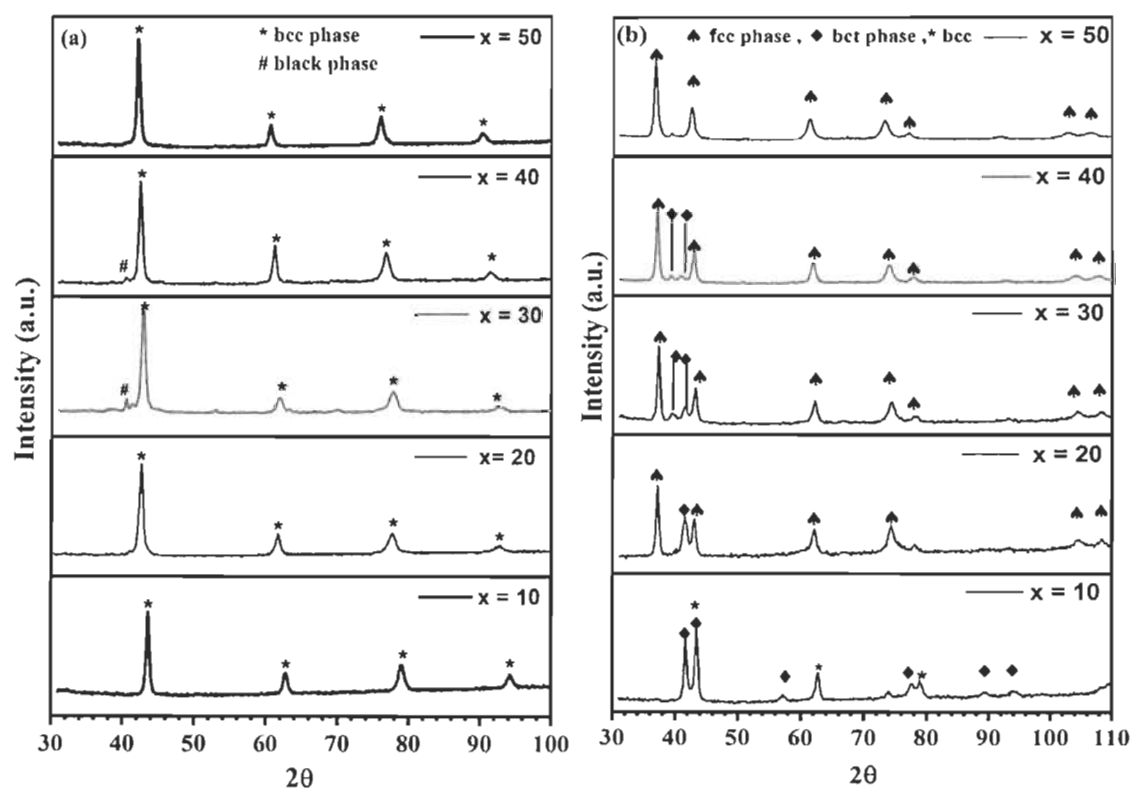


Fig.3.4 XRD pattern of the $Ti_xV_{70-x}Cr_{30}$ ($x = 10, 20, 30, 40, 50$) alloys with additive in (a) as cast and (b) hydrided state.

This minor phase has limited number of peaks, but their positions match the positions of pure titanium (S.G $P6_3/mmc$) which is consistent with the fact that the black phase is essentially titanium precipitates. This phase is not further discussed in this chapter.

To calculate the lattice parameter and crystallite size of the alloys, Rietveld refinement was performed. For as-cast alloys, lattice parameter and crystallite size are reported in table 3.7

| Alloy | Lattice parameter (Å) | Crystallite Size (nm) | Microstrain (%) |
|---|-----------------------|-----------------------|-----------------|
| Ti ₁₀ V ₆₀ Cr ₃₀ | 3.000(2) | 18(1) | 0.43(9) |
| Ti ₂₀ V ₅₀ Cr ₃₀ | 3.023(1) | 15.5(3) | 0.62(4) |
| Ti ₃₀ V ₄₀ Cr ₃₀ | 3.0376(7) | 13.0(5) | 0.19(1) |
| Ti ₄₀ V ₃₀ Cr ₃₀ | 3.069(1) | 14.4(8) | 0.47(9) |
| Ti ₅₀ V ₂₀ Cr ₃₀ | 3.102(1) | 15.6(6) | 0.43(6) |

Table.3.7 Crystal parameters of the Ti_xV_{70-x}Cr₃₀ (x= 10 to 50) alloys in as-cast state. The number in parentheses is the uncertainty on the last significant digit.

This table shows that lattice parameter is increasing for higher x values, but crystallite size is roughly constant. Metallic radius of Ti is bigger than V and Cr, thereby lattice parameters are increasing towards higher x values. In order to see the relationship between lattice parameter, atomic radius and the x values, figure 3.5 present the average atomic radius and lattice parameters as a function of x.

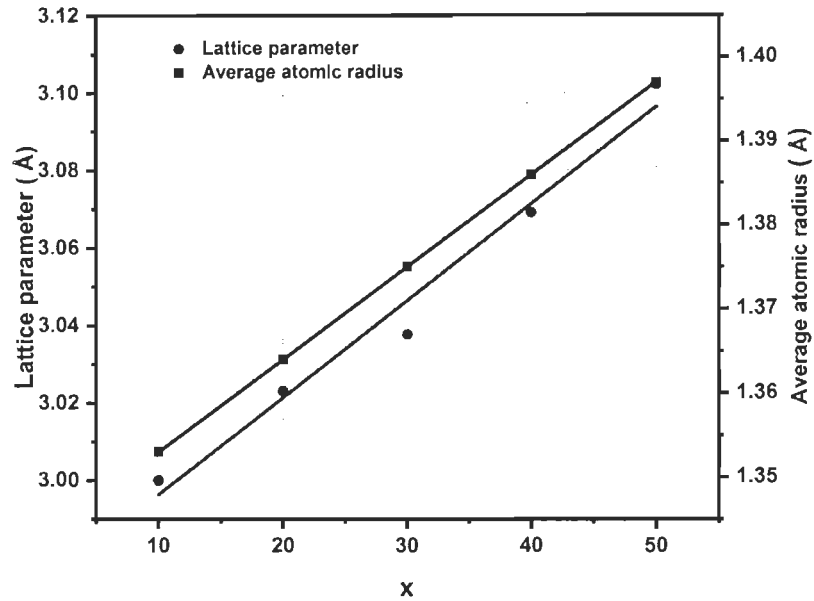


Fig.3.5 Plot of lattice parameters and average atomic radius as a function of Ti concentration (x).

The straight line is a linear fit of the experimental points.

Figure 3.5 clearly shows that the lattice parameters are proportional to the average atomic radius which is expected for a bcc solid solution structure.

3.2.3 First Hydrogenation

First hydrogenation kinetics of as-cast alloys are shown in figure 3.6. It is clear from this figure that absorption capacity of the alloys is increasing and absorption kinetics getting faster with increasing x values. Among all the samples, x = 50, has shown the maximum absorption capacity of 3.6 wt.%. However, a small incubation time is observed for this alloy.

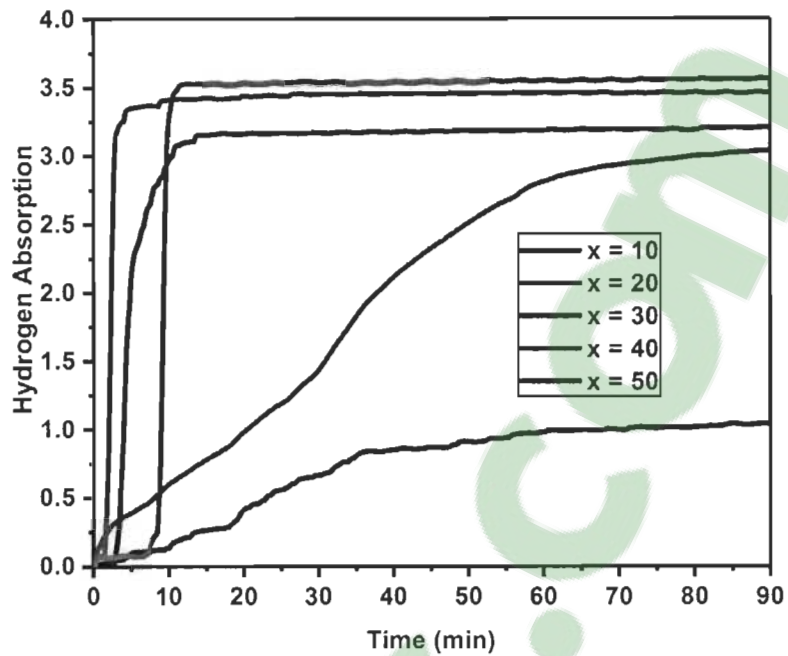


Fig.3.6 Activation curve of the $Ti_xV_{70-x}Cr_{30}$ ($x = 10, 20, 30, 40, 50$) alloys with additive, under 2 MPa of hydrogen at 22 °C.

Effect of the Ti/V ratio (x value) on lattice parameter and absorption capacity of the alloys can be seen from figure 3.7. This figure indicates that lattice parameter and absorption capacity both increases with rising Ti content.

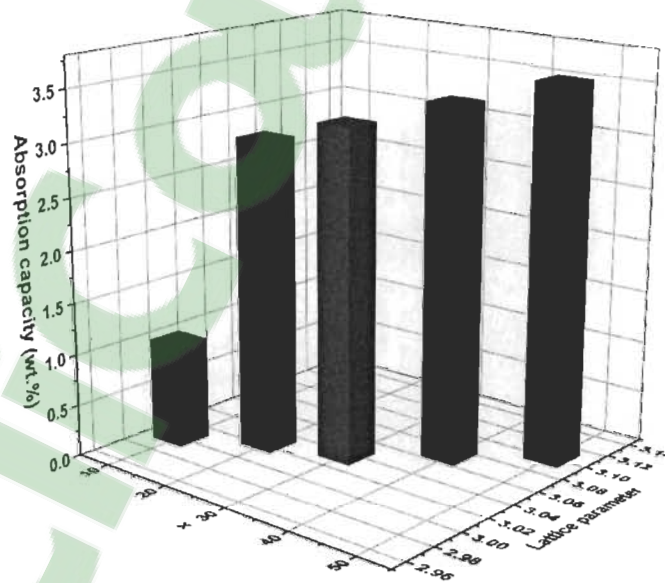


Fig.3.7 Ti-content versus lattice parameter and absorption capacity of $Ti_xV_{70-x}Cr_{30}$ ($x = 10$ to 50)

The crystal structure of all of these hydrided samples were investigated by X-ray powder diffraction. The XRD patterns can be seen in figure 3.4(b). Phase abundance and crystal structure parameters of all the hydrided alloys were evaluated from Rietveld's refinement and are reported in Table 3.8.

| Alloy | Phase | Phase fraction (%) | Lattice parameter (Å) | Crystallite size (nm) | Microstrain (%) |
|---|-------|--------------------|-----------------------|-----------------------|-----------------|
| Ti ₁₀ V ₆₀ Cr ₃₀ | bcc | 28(3) | 2.9978(8) | 12.9(5) | |
| | bct | 72(3) | 3.0016(8) 3.258(1) | 11.8(3) | |
| Ti ₂₀ V ₅₀ Cr ₃₀ | fcc | 61(2) | 4.3346(8) | 18.0(1) | 0.15(1) |
| | bct | 39(2) | 3.149(1) 3.092(2) | 7.2(3) | |
| Ti ₃₀ V ₄₀ Cr ₃₀ | fcc | 79(2) | 4.281(1) | 24(2) | 0.19(1) |
| | bct | 21(2) | 3.2701(1) 3.040(2) | 12.7(1) | |
| Ti ₄₀ V ₃₀ Cr ₃₀ | fcc | 91(2) | 4.3008(8) | 17.0(8) | 0.222(7) |
| | bct | 9.0(8) | 3.316(1) 3.071(2) | 19(2) | |
| Ti ₅₀ V ₂₀ Cr ₃₀ | fcc | 100.0 | 4.3346(8) | 12.0(5) | 0.312(8) |

Table.3.8 Crystal parameters of the Ti_xV_{70-x}Cr₃₀ (x= 10 to 50) alloys in hydrided state. The number in parentheses is the uncertainty on the last significant digit.

It is clear from the table that, with increasing x, bct phase of the hydride alloys is decreasing and fcc phase is increasing. For x = 10, there is only bct and bcc phase. This agrees with the incomplete activation curve seen in the figure 3.6. Presence of bct and bcc phase means that part of the alloy formed monohydride phase after interacting with hydrogen but part of the sample was still unhydrided. It was reported by Nakamura & Akiba that monohydride of bcc alloy has bct structure [46]. Alloy x = 20, 30 and 40, all

showed the presence of a dihydride (fcc) phase along with bct phase. This indicates that these alloys were not fully hydrided. The alloy $x= 50$ was single fcc phase which indicates that this alloy was fully hydrided. It can be seen from figure 3.6, that this alloy had the maximum absorption capacity.

Using the XRD patterns of hydrided samples, expected absorption capacity of each sample could be calculated and compared with the measured one. This calculation has been made on the basis of phase abundance which was determined by Rietveld's refinement. Using the theoretically hydrogen capacity of each phase (bcc = 0 wt.%, bct = 2 wt.%, fcc = 4 wt.%), absorption capacity of each alloy was calculated. These results are reported in table. 3.9. It is to be noticed that secondary phase of the alloys that were seen in micrographs was not noticeable in the X-ray patterns. This could be due to the relatively small proportion of these phases and also to the small crystallite size. Small crystallite size makes the peaks very broad and almost undistinguishable from the background. To identify the crystal structure of secondary phase, neutron diffraction patterns have been taken. This will be discussed in chapter 5. Because the secondary phases were not apparent in the diffraction patterns, it means that only the hydride coming from the bcc phase seen in the as-cast patterns contribute to the diffraction patterns. Thus, the calculated capacity must be adjusted to the fact that the secondary phase did not contribute to the X-ray patterns. It was demonstrated that the bcc phase corresponds to the matrix phase seen in the micrographs. Therefore, the total calculated capacity was multiplied by the abundance of the matrix (bcc) phase as reported in Table 3.6 to give the normalized hydrogen capacity.

Thus the normalized absorption capacities are compared with the measured absorption capacity and reported in table 3.9.

| Alloy (x) | Phase | Phase abundance (wt%) | Phase capacity (wt.%) | Total calculated capacity from X-ray pattern | Normalized capacity (wt.%) | Measured capacity (wt.%) |
|-----------|-------|-----------------------|-----------------------|--|----------------------------|--------------------------|
| 10 | bcc | 28(3) | 0.0 | 1.4(1) | 1.2(1) | 1.0 |
| | bct | 72(3) | 1.4 | | | |
| 20 | fcc | 61(2) | 2.4 | 3.2(1) | 2.7(1) | 3.0 |
| | bct | 39(2) | 0.8 | | | |
| 30 | fcc | 79(2) | 3.2 | 3.6(1) | 3.0(1) | 3.2 |
| | bct | 21(2) | 0.4 | | | |
| 40 | fcc | 91(2) | 3.6 | 3.8(1) | 3.1(2) | 3.4 |
| | bct | 9.0(8) | 0.2 | | | |
| 50 | fcc | 100.0 | 4.0 | 4.0 | 3.5(1) | 3.6 |

Table.3.9 Calculated and experimentally obtained storage capacity of each alloy. The number in parentheses is the uncertainty on the last significant digit.

It can be seen from the table that only for $x = 10$, the measured capacity is lower than the calculated one. However, the difference between these numbers is very small or negligible considering the uncertainties. For all other alloys, the measured capacity is slightly higher than the calculated one. This missing capacity could be due to the secondary phase, because in our theoretical calculation we did not consider secondary phase as a hydrogen absorbing phase.

3.2.4 Pressure composition temperature (PCT)

To see the effect of Ti-proportion on thermodynamics of Ti-V-Cr alloy, PCT measurements have been done on $x = 40$ and 50 alloy at $150\text{ }^{\circ}\text{C}$. The results are reported in figure 3.8. Before the PCT measurement samples were hydrogenated at room temperature under 20 bars of hydrogen pressure and then heated to $150\text{ }^{\circ}\text{C}$. To prevent the alloys from the dehydrogenation during heating, a hydrogen pressure of 20 bar was maintained.

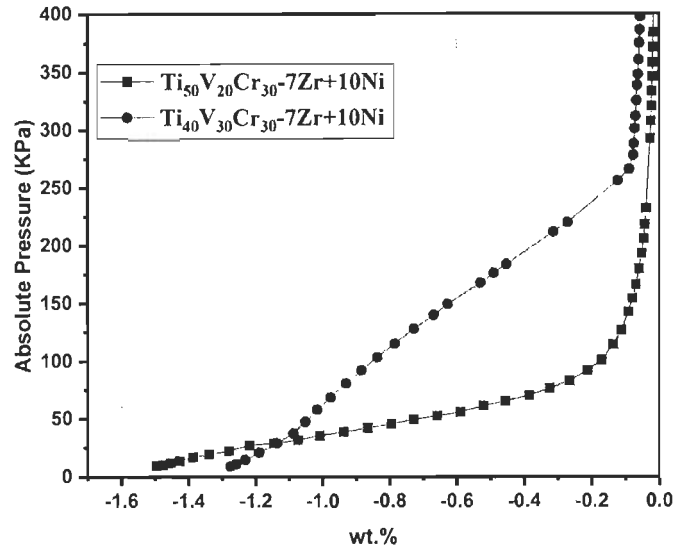


Fig.3.8 Desorption PCT curves of $Ti_xV_{70-x}Cr_{30}$ ($x = 40, 50$) alloy added with 4 wt.% of 7Zr+10Ni at $150^\circ C$.

It can be seen from the figure that, when x increases from 40 to 50, desorption capacity increases from 1.3 wt.% to 1.5 wt.%. We also see a drastic change in the shape of the isotherms. For $x = 50$ the isotherm is almost flat while for $x = 40$, it is highly sloped.

3.3 Conclusions

The microstructure, crystal structure and first hydrogenation kinetics of $Ti_xV_{70-x}Cr_{30}$ ($x = 10$ to 50) to which 4 wt.% of 7Zr+10Ni was added have been reported in this chapter. The main findings of this work are as follows:

The microstructure of $Ti_xV_{70-x}Cr_{30}$ ($x = 10$ to 50) alloys revealed the presence of a main bcc phase (matrix) along with the secondary phases. Ti-precipitate (black phase) was seen in all alloys. A bright phase with changing composition was found in all alloys. X-ray patterns identified the main phase in as-cast alloys as being bcc. For alloys $x = 30$ and 40, a minor Ti-phase was also seen along with bcc phase. After hydrogenation, alloy $x = 10$, has shown a bct phase along with residual bcc phase. For alloys $x = 20$ to 40, two hydride phases were present: a bct monohydride phase and a dihydride fcc phase. Presence of monohydride phase confirmed that these alloys were not fully hydrided. On

the other hand, for alloy $x = 50$, a single fcc phase was found which confirmed that this alloy was fully hydrided. Hydrogenation curves revealed the slow absorption kinetics of alloys $x = 10$ and 20 , compared to alloys $x = 30, 40$ and 50 . Absorption capacity of the alloys was found increasing with rising Ti- proportion.

This study highlights that varying elemental composition affects the microstructure, hydrogenation kinetics and thermodynamic of the alloy. Increasing Ti-content improve the absorption capacity for Ti-V-Cr alloy.

Chapter 4

Investigation of the microstructure, crystal structure and hydrogenation kinetics of Ti-V-Cr alloy with Zr addition

4.1 Introduction

In the previous chapter, it was seen that addition of 4 wt.% of 7Zr+10Ni to $Ti_xV_{70-x}Cr_{30}$ ($x = 10$ to 50) alloys improved the activation kinetics[47]. The microstructure of these alloys revealed Zr and Ni-rich secondary phases. This motivated us to use Zr, as an additive for the same compositions and compare it with (7Zr+10Ni). This study helps to understand the role of additive in $Ti_xV_{70-x}Cr_{30}$ ($x = 10$ to 50) alloy. In this chapter, microstructure, crystal structure and hydrogenation kinetics of $Ti_xV_{70-x}Cr_{30}$ ($x = 10$ to 50) alloy added with 4 wt.% of Zr is reported.

4.2 Results and Discussion

Scanning electron microscopy revealed that, all of these alloy were multiphase but with different microstructure and phase composition. From X-ray diffraction, bcc structure of all as-cast alloys was confirmed. For alloy $x= 30$ and 40, Ti and Ti-Zr high pressure-high temperature phases were observed along with the bcc phase. Upon hydrogenation, bcc phase transformed to a body centred tetragonal and a face centred cubic phase. Only alloy $x=40$, has shown a complete hydrogenation. A linear relationship between the volume of hydrogen in fcc phase and bcc lattice parameters has been observed. This study also emphasis that 7Zr + 10Ni is better additive than Zr for $Ti_xV_{70-x}Cr_{30}$ ($x = 10, 20, 30, 40, 50$) alloy. All of these results are reported in detail below.

4.2.1 Morphology

Figure 4.1 shows the backscattered electron micrographs of the as-cast alloy $Ti_xV_{70-x}Cr_{30}$ ($x = 10, 20, 30, 40, 50$), added with 4 wt.% of Zr. It is clear from the figure that these alloys have different microstructures.

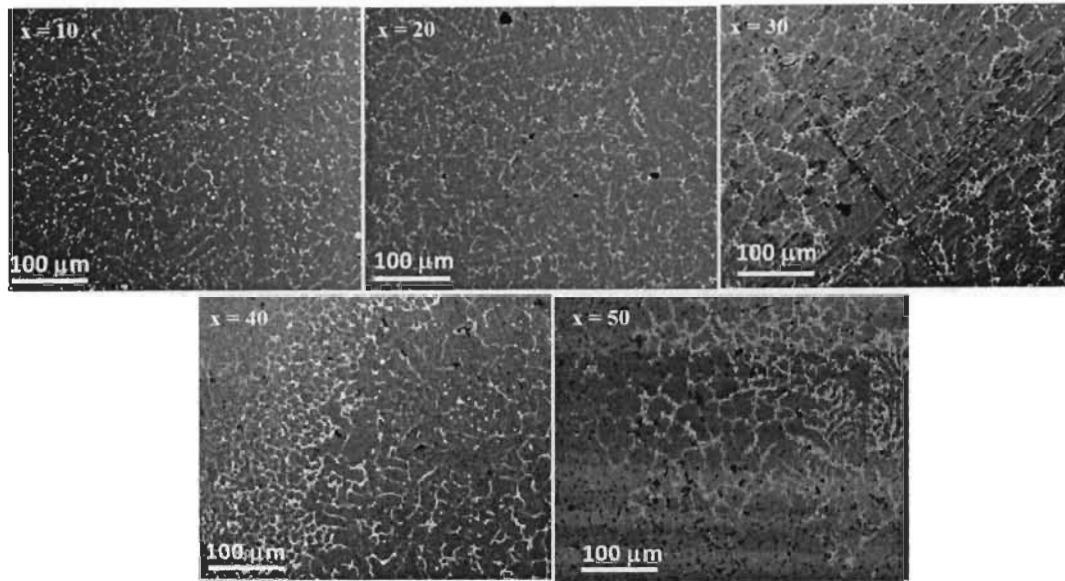


Fig.4.1: Backscattered electrons micrograph of the alloys $Ti_xV_{70-x}Cr_{30}$ ($x = 10, 20, 30, 40, 50$), added with 4 wt.% of Zr.

These alloys are made up of three phases: a matrix, a bright phase and a black phase. Relative abundance of these phases was found to be different for each composition. For alloys $x = 10$ and 20 the microstructure is homogeneous but for the other alloys, it is clearly inhomogeneous with regions having more secondary phase than others. The reason for this behaviour is most probably cooling rate. This inhomogeneity makes the estimation of relative amount of each phase more difficult. Using ImageJ, the relative amount of each phase was estimated and is reported in Table 4.1

| Alloy | Matrix (%) | Bright phase (%) | Black phase (%) |
|---|------------|------------------|-----------------|
| Ti ₁₀ V ₆₀ Cr ₃₀ | 91.4 | 8.3 | -- |
| Ti ₂₀ V ₅₀ Cr ₃₀ | 92.1 | 7.8 | -- |
| T ₃₀ V ₄₀ Cr ₃₀ | 86.2/77.5 | 9.05/7.5 | 15.2/5.4 |
| Ti ₄₀ V ₃₀ Cr ₃₀ | 89.7/85.4 | 13.2/7.1 | 2.8/1.1 |
| Ti ₅₀ V ₂₀ Cr ₃₀ | 86.9/84.7 | 11.7/6.6 | 5.9/3.3 |

Table 4.1: Percentage of the observed phases for the alloy Ti_xV_{70-x}Cr₃₀ (x= 10 to 50) added with 4 wt.% of Zr, as determined by imagej. Error on the measured values is ±0.5 at.%. For inhomogeneous phases, the higher/lower values are indicated.

It can be seen from table 1 that the matrix phase is the most abundant phase for all alloys. Relative amount of black phase is found higher for x =30 than alloy x = 40 and 50. In order to see each phase clearly, high magnification micrographs are presented in figure 4.2.

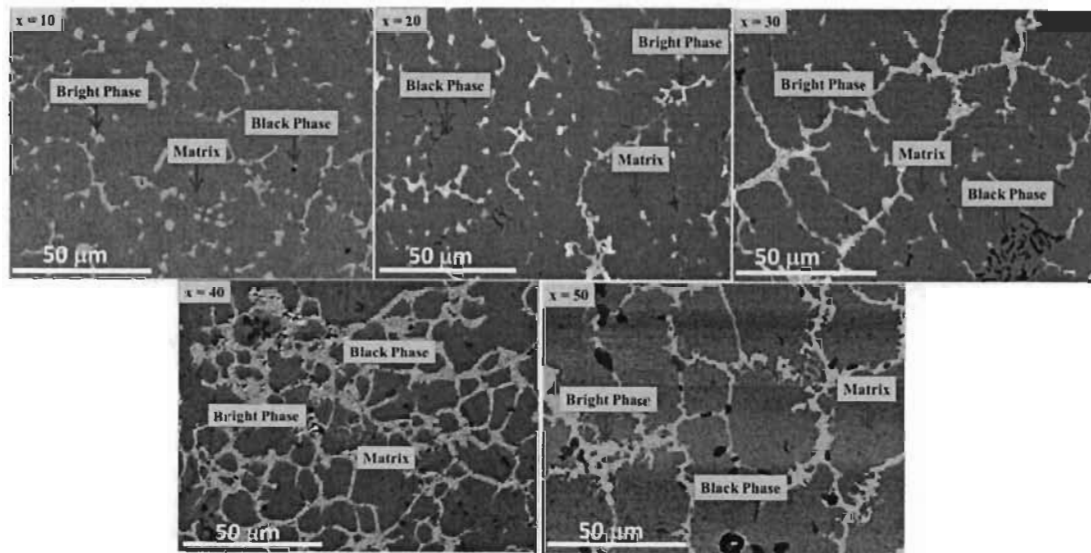


Fig.4.2: Higher magnification backscattered electrons micrograph of the alloys Ti_xV_{70-x}Cr₃₀ (x = 10, 20, 30, 40, 50), added with 4 wt.% of Zr.

To measure the elemental composition of these phases, EDS analysis has been performed. The results for the alloy Ti₁₀V₆₀Cr₃₀ added with 4 wt.% of Zr are reported in Table 4.2. It can be seen clearly from the table that the matrix composition is similar to

the bulk nominal value and the bright phase is rich in zirconium. The black phase is mainly titanium with some zirconium.

| Elements | Bulk nominal value | Matrix | Bright phase | Black phase |
|----------|--------------------|--------|--------------|-------------|
| Ti | 9.9 | 8.9 | 27.2 | 79.1 |
| V | 58.5 | 60.1 | 11.1 | 4.1 |
| Cr | 29.2 | 29.6 | 5.2 | 2.5 |
| Zr | 2.2 | 1.4 | 56.4 | 14.2 |

Table 4.2: Nominal and measured atomic percentage of the as-cast samples $Ti_{10}V_{60}Cr_{30}$ added with 4 wt.% of Zr. Error on measured value is ± 0.5 at.%.

Table 4.3 is showing the chemical analysis of alloy $x = 20$, where again it is seen that matrix composition of the alloy is similar to the bulk nominal value and black phase has a very similar composition to the black phase of the previous alloy. Bright phase of this alloy is Ti-Zr rich but the composition is very different than the bright phase for $x = 10$.

| Elements | Bulk nominal value | Matrix | Bright phase | Black phase |
|----------|--------------------|--------|--------------|-------------|
| Ti | 19.6 | 19.1 | 44.3 | 78.3 |
| V | 48.9 | 50.1 | 8.2 | 5.3 |
| Cr | 29.3 | 29.4 | 6.1 | 1.4 |
| Zr | 2.1 | 1.5 | 41.4 | 14.9 |

Table 4.3: Nominal and measured atomic percentage of the as-cast samples $Ti_{20}V_{50}Cr_{30}$ added with 4 wt.% of Zr. Error on measured value is ± 0.5 at.%.

The chemical composition of the different phases of the alloy $x = 30$ as measured by EDS is reported in Table 4.4. Here again, matrix composition and bulk nominal value of

the alloy are similar. Black phase is seen as Ti- precipitate and the bright phase shows high abundance of Ti and Zr with a small percentage of V and Cr.

| Elements | Bulk nominal value | Matrix | Bright phase | Black phase |
|-----------|--------------------|--------|--------------|-------------|
| Ti | 29.3 | 28.2 | 49.7 | 84.9 |
| V | 39.1 | 40.3 | 11.9 | 5.7 |
| Cr | 29.3 | 29.9 | 8.9 | 2.1 |
| Zr | 2.2 | 1.6 | 29.5 | 17.3 |

Table 4.4: Nominal and measured atomic percentage of the as-cast samples $Ti_{30}V_{40}Cr_{30}$ added with 4 wt.% of Zr. Error on measured value is ± 0.5 at.%.

Table 4.5, shows the EDS measurements for alloy $x = 40$. It indicates that matrix is similar to the bulk nominal value with a small percentage of Zr. Black phase is Ti-rich. Bright phase is 62% Ti and 23 % Zr, other elements like V and Cr are less than 10% each.

| Elements | Bulk nominal value | Matrix | Bright phase | Black phase |
|-----------|--------------------|--------|--------------|-------------|
| Ti | 38.5 | 38.7 | 62.2 | 84.4 |
| V | 29.6 | 30.2 | 8.1 | 2.8 |
| Cr | 29.6 | 29.8 | 6.2 | 0.9 |
| Zr | 2.1 | 1.3 | 23.5 | 11.9 |

Table 4.5: Nominal and measured atomic percentage of the as-cast samples $Ti_{40}V_{30}Cr_{30}$ added with 4 wt.% of Zr. Error on measured value is ± 0.5 at.%.

Elemental analysis for $x = 50$ is reported in Table 4.6. Matrix composition is seen to be similar to the nominal value, black phase is Ti-rich and the bright phase is enriched with Ti and Zr.

| Elements | Bulk nominal value | Matrix | Bright phase | Black phase |
|----------|--------------------|--------|--------------|-------------|
| Ti | 48.9 | 48.4 | 64.4 | 88.1 |
| V | 19.6 | 19.2 | 4.1 | 2.4 |
| Cr | 29.4 | 30.1 | 5.6 | 2.1 |
| Zr | 2.1 | 2.3 | 24.4 | 7.5 |

Table 4.6: Nominal and measured atomic percentage of the as-cast samples $Ti_{50}V_{20}Cr_{30}$ added with 4 wt.% of Zr. Error on measured value is ± 0.5 at.%.

It is clear from the EDS analysis that all of these alloys have different matrix and bright phase composition which is illustrated more clearly in Figure 4.3(a) and 4.3(b) respectively.

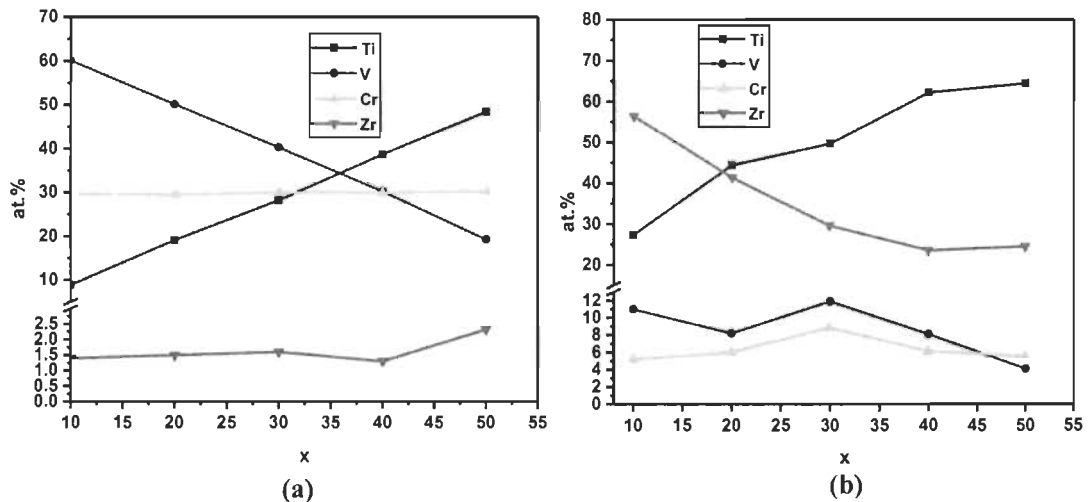


Fig.4.3. Chemical analysis of the elements in Matrix (a) and Bright phase (b) with varying Ti concentration x.

As seen from fig.4.3(a), for the matrix, Ti and V are varying with x, while Cr and Zr are constant for all x values. On the other hand, for the bright phase (fig. 4.3(b)), Ti and Zr proportions change with x while V and Cr proportions show very small variation.

4.2.2 Crystal Structure

X-ray diffraction patterns of $Ti_xV_{70-x}Cr_{30}$ alloy in as-cast state are shown in figure 4.4(a). As seen from the figure, all as-cast alloys have body centred cubic (bcc) phase. However, alloy $x = 30$ and 40 have shown two additional minor phases along with the bcc phase which are titanium and high-temperature-high-pressure (HT HP) Ti-Zr phase. Comparing these results with the SEM and EDS analysis, it is found that Ti (S.G. $P6_3/mmc$) and HT HP Ti-Zr phase (S.G. $P6/mmm$) corresponds to the black and bright phase seen in the backscattered images.

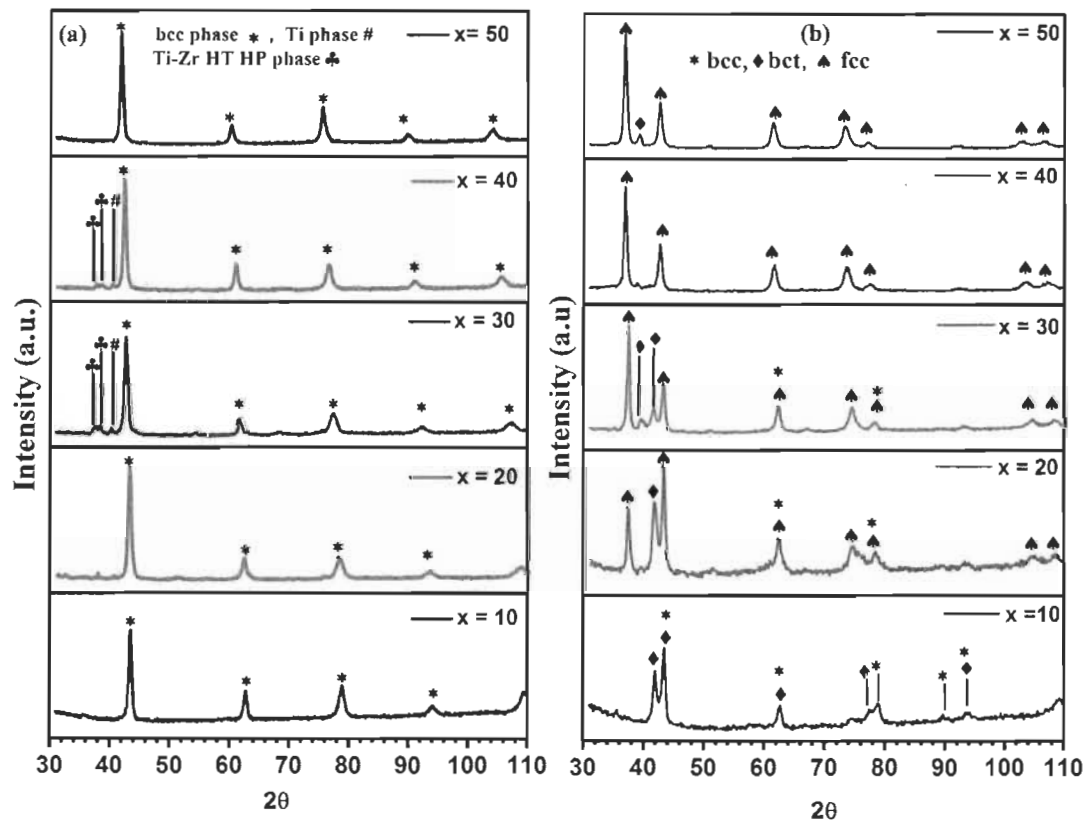


Fig.4.4 XRD pattern of $Ti_xV_{70-x}Cr_{30}$ ($x = 10$ to 50) alloys added with 4 wt.% of Zr in (a) as-cast and (b) hydride state.

Lattice parameters, phase abundances and crystallite sizes for each alloy were determined by Rietveld's refinement and are reported in table 4.7. For all patterns, the microstrain parameter was found to be zero within experimental error. This table shows clearly that bcc crystallite size is constant from $x = 10$ to 50 while lattice parameters are

increasing from 3.0032(4) Å to 3.1142(4) Å. In order to understand the relation between lattice parameter of bcc phase and Ti-content, average atomic radius of each alloy is calculated and a graph is presented where lattice parameter and average atomic radius are plotted as a function of x.

| Alloy | Phase | Phase Abundance (%) | Lattice Parameter (Å) | Crystallite size (nm) |
|--------|----------------|---------------------|-----------------------|-----------------------|
| x = 10 | bcc | 100 | 3.0032(4) | 17.1(7) |
| x = 20 | bcc | 100 | 3.0170(6) | 18.0(8) |
| x=30 | bcc | 88.7(6) | 3.0460(5) | 15.3(5) |
| | Ti | 1.6(2) | 2.981(1) 4.800(4) | 32.1(6) |
| | Ti-Zr HP HT | 9.7(5) | 4.783(3) 3.034(3) | 8.2(7) |
| x = 40 | bcc | 92.4(5) | 3.0795(4) | 17.7(5) |
| | Ti | 2.4(3) | 2.986(3) 4.83(1) | 7.6(1) |
| | Ti-Zr HP HT | 5.1(4) | 4.769(3) 3.030(4) | 9.5(1) |
| x = 50 | bcc | 100 | 3.1142(4) | 15.0(4) |

Table 4.7: Crystal parameters of $Ti_xV_{70-x}Cr_{30}$ (x = 10 to 50) alloy added with 4 wt.% of Zr. Number in the parenthesis is the error on the last significant digit.

Figure 4.5 shows a linear relationship between the lattice parameter of the bcc phase and Ti content. Direct relationship between the average atomic radius and the lattice parameter is also clear from this figure.

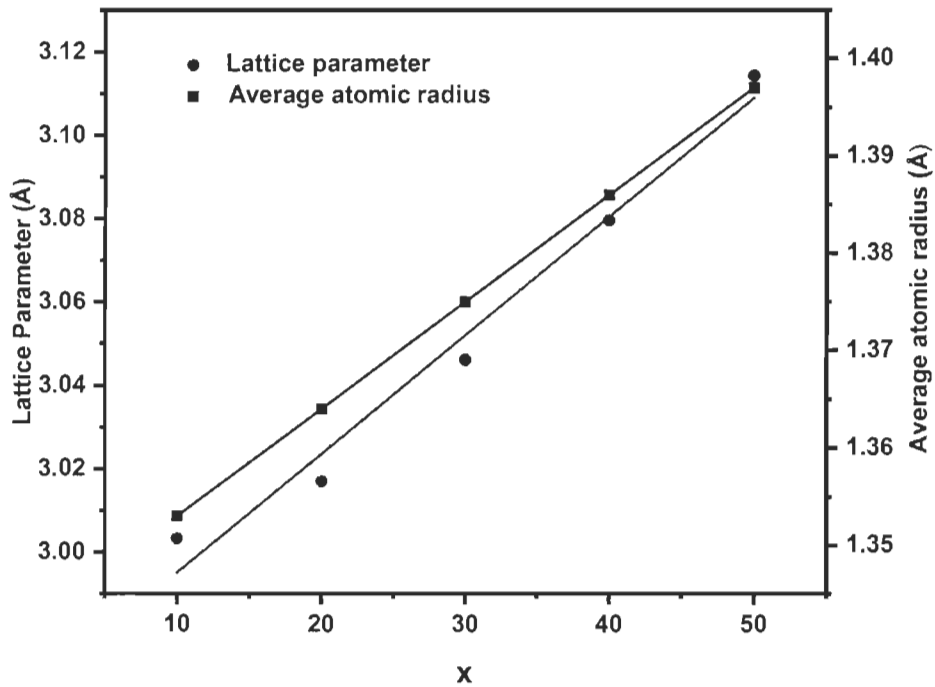


Fig.4.5: Lattice parameters and average atomic radius of bcc phase as a function of Ti-content (x).

4.2.3 First Hydrogenation

After studying the microstructure and crystal structure of $Ti_xV_{70-x}Cr_{30}$ ($x= 10, 20, 30, 40, 50$) alloys, hydrogen measurements were performed. Figure 4.6, shows the first hydrogenation (activation) curves of the $Ti_xV_{70-x}Cr_{30}$ ($x= 10, 20, 30, 40, 50$) alloys. These measurements were done at room temperature under 20 bar pressure. It has to be mentioned that these measurements were done without any prior heat treatment of these alloys. As seen from the curves, absorption capacity increases with increasing x values. Alloy $x = 50$, has shown the maximum absorption capacity of 3.7 wt.%. Initially, this alloy has shown a long incubation time. Afterward, it took 350 min to absorb 3.7 wt.%.

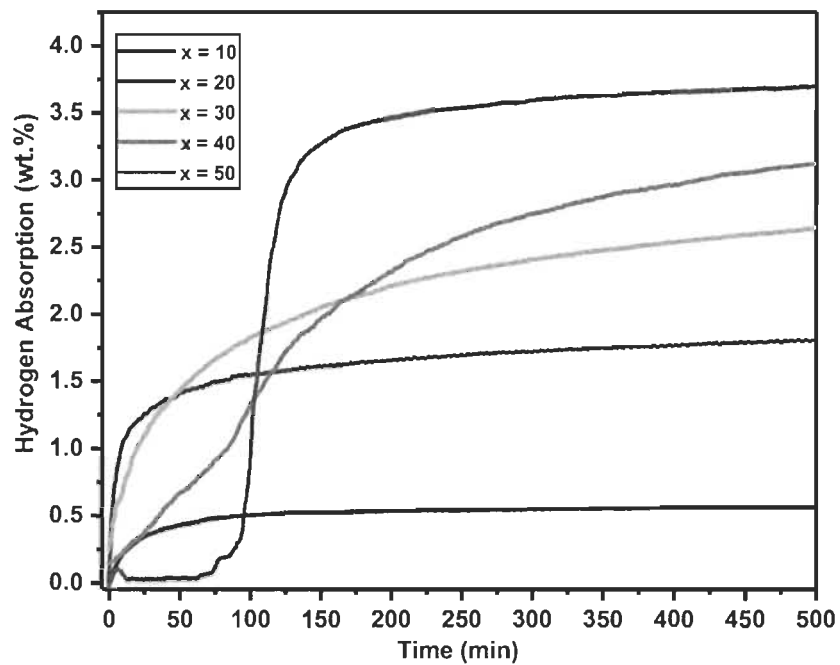


Fig.4.6. Activation curve of the $Ti_xV_{70-x}Cr_{30}$ ($x = 10, 20, 30, 40, 50$) alloys added with 4 wt.% of Zr, under 20 bars of hydrogen at 22 °C

Crystal structure of these hydrided alloys has been studied by X-ray diffraction. Diffraction patterns are shown in figure 4.4(b). It can be seen that except for the alloy $x = 40$, all the hydrided alloys have more than one phases. These phases correspond to bcc (S.G. Im-3m), body centred tetragonal (bct, S.G. I4/mmm), and face centred cubic (fcc, S.G. Fm-3m). Lattice parameters and phase analysis of all hydrided alloys were evaluated by Rietveld's refinement and are presented in table 4.8. As for the as-cast case, for all patterns the microstrain parameter was found to be zero within the experimental error.

| Alloy | Phase | Phase Abundance (%) | Lattice Parameter (Å) | Unit cell volume (Å ³) | Crystallite size (nm) |
|-------|-------|---------------------|------------------------|------------------------------------|-----------------------|
| 10 | bcc | 37(3) | 3.0031(8) | 27.08(2) | 12.0(5) |
| | bct | 63(3) | 3.0140(1) 3.2126(2) | 29.18(3) | 7.5(3) |
| 20 | bcc | 26 (2) | 3.0233(8) | 27.63 | 10.6(5) |
| | bct | 36 (2) | 3.0971(1) 3.175(2) | 30.46(4) | 18(3) |
| | fcc | 37 (1) | 4.2712(1) | 77.90(8) | 19(3) |
| 30 | bcc | 18 (1) | 3.1379(1) | 30.90(4) | 7.6 (5) |
| | bct | 15(1) | 3.155(5) 3.455(8) | 34.40(14) | 5.9(6) |
| | fcc | 67 (2) | 4.2821(9) | 78.52(5) | 19 (1) |
| 40 | fcc | 100 | 4.3067(8) | 79.88(5) | 13.3 (5) |
| 50 | bct | 6.8(5) | 3.301(2) 3.361(4) | 36.62(7) | 12(1) |
| | fcc | 93.2 (5) | 4.3287(7) | 81.11(4) | 15.2 (5) |

Table 4.8: Crystal parameter of $Ti_xV_{70-x}Cr_{30}$ ($x = 10$ to 50) alloy added with 4 wt.% of Zr in hydride state. Numbers in parentheses is the error on the last significant digit.

As seen from table 4.8, hydride phase of alloy $x = 10$, consists of a bcc and a bct phase. Lattice parameters of hydride bcc phase is similar to the lattice parameter of as cast bcc phase (table 4.7) for this alloy. On the other hand, lattice expansion of bct phase, compared to the as-cast bcc, is quite small: only 1.05 \AA^3 per unit cell. It is well known that the monohydrate of a bcc phase is a bct phase [46]. Usually, the volume occupied by a hydrogen atom in the lattice is between 2 \AA^3 and 3 \AA^3 . This means that only between 0.5 and 0.33 hydrogen atom is absorbed by the formula unit which is not the characteristic of a monohydrate. This indicates that bct phase of alloy $x = 10$ is not a true

monohydrate. This is also confirmed from the activation curve of this alloy. Measured capacity of $x = 10$ is only 0.5 wt.%. Considering that 63% of the alloy is bct this means that the true capacity of this bct phase is about 0.8 wt.%. As the nominal capacity of the monohydrate is 2 wt.% this means that only 0.4 hydrogen atom instead of 1 was absorbed by the bct phase. This number agrees well with the ones derived from the diffraction patterns. Therefore, we could conclude that, for this alloy, because of the small lattice parameter of the bcc phase, it is very difficult for hydrogen to go into the bcc solid solution phase and when it does it forms a bct phase but with a stoichiometry much smaller than a monohydrate.

For alloy $x = 20$, bcc and bct phase are seen along with face centred cubic phase (fcc). In this case, after hydrogenation lattice expansion of bcc and bct phase compared to the as-cast bcc was found to be very small: 0.19 \AA^3 and 1.5 \AA^3 respectively. This indicates that for bcc and bct phase hydrogen atom absorbed by the formula unit is 0.06 and 0.5 respectively. Here again it means that bct phase is not a true monohydrate phase. On the other hand, lattice expansion for fcc phase is 5.74 \AA^3 which means hydrogen atom absorbed by formula units are 2. This is the characteristics of a dihydride phase. Considering the phase abundance (bcc = 26 wt.%, bct = 36 wt.%, fcc = 37 wt.%) and nominal hydrogen capacity of each phase (bct = 2 wt.%, fcc = 4 wt.%), the total absorption capacity calculated from the X-ray diffraction pattern of the alloy is 1.87 wt.% which is very close to the measured one. However, from a thermodynamics point of view having a bcc, bct, and fcc phases simultaneously is not possible. The presence of these three phases simultaneously is most probably due to slow diffusion of hydrogen through the fcc and bct phases. This means that, upon hydrogenation, a 'shell' of fcc phase forms and, as diffusion is slow through this phase, the hydrogen could not reach the bct and bcc phase in the "core". This is a classic explanation for the incomplete hydrogenation in many metal hydrides.

For alloy $x = 30$ and 50 , from the lattice expansions we determined that one hydrogen atom was absorbed in bct phase and two were absorbed in the fcc phase. This indicates that for these alloys bct phase was a true monohydrate and fcc phase was a dihydride. Alloy $x = 40$ was a complete dihydride without any bcc or bct phases.

Figure 7 shows the volume of the hydrogen atom in the fcc phase as a function of x . The volume of hydrogen atoms was calculated from the difference in unit cell volume of the bcc phase before hydrogenation and the fcc phase after hydrogenation. It is clear from the figure that the volume of the hydrogen atom in the fcc phase decreases with x . This result is somewhat counterintuitive. As shown in figure 4.5, the lattice parameter of the bcc phase increases with x . Therefore, the interstitial sites available for hydrogen will be bigger as x increases. This means that the volume increase due to the absorption of hydrogen is smaller for a bigger bcc lattice parameter which is exactly what we see. To our knowledge this is the first time such behaviour is seen. Similar investigation on other bcc alloys should be performed in order to validate this result.

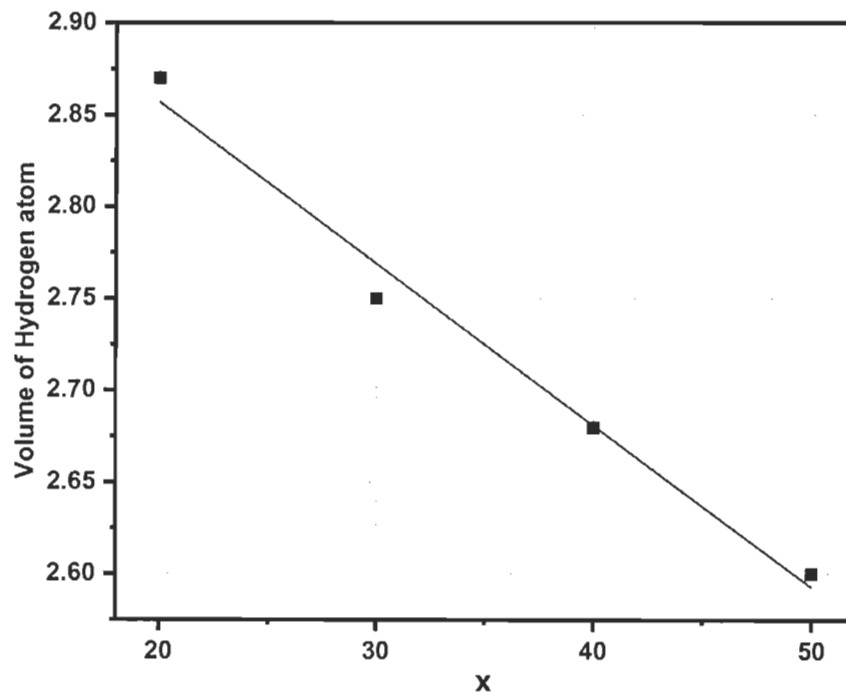


Fig 4.7: For $Ti_xV_{70-x}Cr_{30}$ ($x = 20$ to 50) alloy, volume of hydrogen atoms in fcc phase

4.2.4 Comparison between Zr and 7Zr+10Ni additive

In this section, a comparison between 7Zr+10Ni additive with Zr additive is shown. For this comparison, $Ti_{40}V_{30}Cr_{30}$ alloy has been selected. Activation kinetics of $Ti_{40}V_{30}Cr_{30}$ alloy with Zr and with 7Zr+10Ni additives are compared in figure 4.8. In this figure, as a reference, hydrogenation kinetics of the same composition without any additive is also shown. It can be seen that the alloy without any additive does not absorb hydrogen. However, the same composition to which was added Zr and 7Zr+10Ni could absorb hydrogen. These results emphasize that an additive is essential to make the activation possible at room temperature. The alloy with 7Zr+10Ni presents a very fast kinetics compared to the alloy with Zr. This could be understood on the basis of different microstructure of Zr and 7Zr+10Ni added alloys. With 7Zr+10Ni additive, the alloy has a Zr-Ni rich secondary phase. When Zr is the additive, the secondary phase is Zr-rich. The relative abundance of the secondary phase for both 7Zr+10Ni and Zr added alloys is also different. For 7Zr+10Ni added alloys, the secondary phase proportion was found to be between 0.2 % and 7 %. For Zr added alloys, the proportion was between 6.6 % and 13.2%. Even though Zr added alloy has a high percentage of secondary phase compared to 7Zr+10Ni alloy, still it has slow kinetics. This indicates that the combined effect of Zr-Ni is more beneficial for fast absorption than Zr alone.

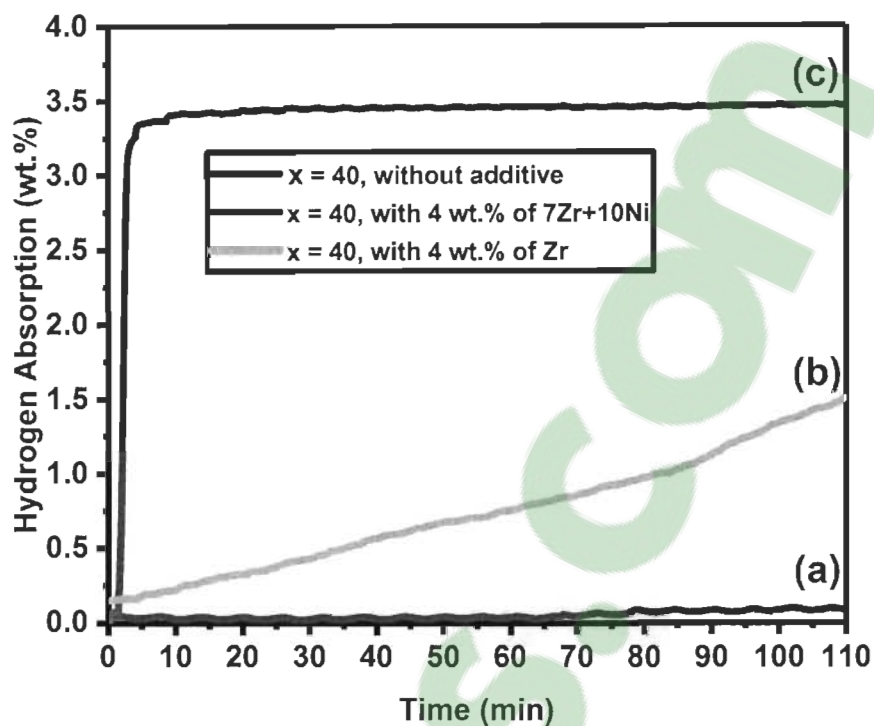


Fig.4.8: First hydrogenation kinetics of $Ti_{40}V_{30}Cr_{30}$ alloy (a) without additive (b) with 4 wt.% of Zr (c) with 4 wt.% of 7Zr+10Ni, under 20 bars of hydrogen at 22 °C

4.3 Conclusions

Five different composition of $Ti_xV_{70-x}Cr_{30}$ ($x=10$ to 50) alloys added with 4 wt.% of Zr has been studied. All alloys presented a multiphase microstructure. X-ray patterns confirmed that all the as cast alloys were bcc but for alloy $x=30$ and 40 Ti and HT-HP Ti-Zr phases were also observed along with bcc phase.

Hydrogenation curves have shown that increasing Ti-content is beneficial for higher absorption capacity which is also confirmed by the XRD patterns of these hydride alloys. Alloys $x=10$ and 20 have shown the presence of bct phase which was not a true monohydrate phase. For this reason, these alloys have shown small absorption capacity. For $x=30$ and 50, a complete monohydrate phase was seen. Upon hydrogenation, only alloy $x=40$ has shown a single fcc phase.

This study also demonstrated that volume occupied by the hydrogen in fcc phase linearly decreased with increasing bcc lattice parameters.

Comparison of Zr additive with 7Zr+10Ni additive emphasized that the 7Zr+10Ni is more effective for the enhancement of first hydrogenation. The reason for this discrepancy is probably the different microstructure and the synergetic effect of Zr and Ni. Therefore, it is concluded here that for $Ti_xV_{70-x}Cr_{30}$ ($x= 10$ to 50) alloys, 7Zr+10Ni is better additive than Zr.

Chapter 5

Neutron, and EXAFS studies of $\text{Ti}_{50}\text{V}_{20}\text{Cr}_{30}$ added with 4wt. % of 7Zr+10Ni

5.1 Introduction

In the previous chapters, it was shown that adding 7Zr+10Ni to $\text{Ti}_x\text{V}_{70-x}\text{Cr}_{30}$ ($x = 10$ to 50) alloys resulted in better first hydrogenation kinetics than by adding Zr. It was also shown that $x = 50$ alloys gave the highest capacity amongst these alloys. Therefore, further investigations were targeted to this particular alloy. The microstructure of this alloy consisted of a matrix, along with a black and bright phases. In order to study the characteristics of the individual phases, we synthesized each of them using the chemical composition found from EDS measurements. As the black phase is essentially titanium, this phase was not investigated further. Scanning electron microscopy and hydrogenation measurements were performed to understand the morphology and absorption capacity of these alloys.

As the main phase is a solid solution bcc alloy, the local environment of hydrogen do not constant but change from one site to another due to the statistical nature of the bcc solid solution. It is interesting to know the effect of local environment on hydrogenation properties and if this environment change upon hydrogenation. One effective way to probe local environment is to use Extended X-Ray Absorption Fine structure (EXAFS) which probe the local environment of a selected type of atoms. For the EXAFs study, we synthesized two alloys with compositions identical to the matrix and bright phase of $\text{Ti}_{50}\text{V}_{20}\text{Cr}_{30}$ alloy. They are respectively designated 50TiM and 50TiBP alloys. By performing EXAFS of the Ti-edge of these two alloys in the as-cast, hydrided and desorbed states, we hope to understand the dynamic of hydrogenation and its effect on local environment of atoms.

EXAFS probe the local environment of atoms but could not locate the hydrogen atom in the crystal structure. The practically only way to do this is by neutron diffraction. For

this type of experiment we again selected the $\text{Ti}_{50}\text{V}_{20}\text{Cr}_{30}$ alloy because it is the most interesting one from a practical point of view and also, because of its high capacity and single phase, it will give a stronger neutron diffraction signal.

5.2. Neutron study on $\text{Ti}_{50}\text{V}_{20}\text{Cr}_{30}$

In order to locate the hydrogen in the crystal structure of $\text{Ti}_{50}\text{V}_{20}\text{Cr}_{30}$ alloy, in-situ desorption neutron diffraction on the fully deuterated alloy was done. But first, the neutron diffraction behaviour of $\text{Ti}_{50}\text{V}_{20}\text{Cr}_{30}$ alloy should be discussed. Taking into account the scattering length of Ti, V, Cr, Zr and Ni, average scattering length of each phase of $\text{Ti}_{50}\text{V}_{20}\text{Cr}_{30}$ alloy was calculated and are reported in table 5.1.

| Alloy | Phase | Average scattering length (fm) |
|---|--------------|--------------------------------|
| $\text{Ti}_{50}\text{V}_{20}\text{Cr}_{30}$ | Matrix phase | -0.4204 |
| | Bright phase | 1.61528 |
| | Black phase | -2.03764 |

Table 5.1: Average scattering length of the different phases of $\text{Ti}_{50}\text{V}_{20}\text{Cr}_{30}$

It can be seen from the table that the scattering length of the matrix phase is very close to the scattering length of vanadium (-0.3824 fm). It is well known that the scattering length of vanadium is so small that it is essentially transparent to neutron. Therefore, the matrix phase of this alloy is a null matrix and no Bragg peaks could be seen on the diffraction pattern and this phase could not be observed. On the other hand, the bright and black phases have much higher absolute scattering lengths and they could be seen on the diffraction patterns.

The fact that the bcc phase could not be seen in neutron diffraction is not necessarily a bad situation. When a bcc alloy absorbs hydrogen, it forms first a bct structure (monohydride) and thereafter a fcc structure (dihydride). As deuterium has a high scattering length, the bct and fcc structures will be easily seen. Thus, change in the state of hydrogenation could be tracked by in-situ neutron diffraction.

We decided to study the dehydrogenation of the fully hydrided $\text{Ti}_{50}\text{V}_{20}\text{Cr}_{30}$ alloy which, as shown by the X-ray diffraction pattern, is a pure fcc phase. The sample was first deuterided and thereafter installed on the neutron diffraction sample holder where the temperature was increased under a dynamic vacuum. During the experiment temperature was raised from 122 °C to 266°C. The diffraction patterns at various temperatures are shown in figure 5.1. Rietveld refinement was performed on all patterns. The metal atoms position and occupancy were kept fixed while the hydrogen (deuterium) site occupancy was refined. From the Rietveld refinement of neutron pattern, it was found that main phase of the alloy was fcc. The sharp residual peaks are due to the Al body of the heater which was physically attached to the sample during the experiment. It can be seen from the figure that peak intensity of fcc phase decreases as the temperature increases. Effect of temperature on deuterium (D) occupancy and on fcc cell parameter can be seen from fig 5.2(a). It is clear that D occupancy of the alloy start to decrease at about 200° C. The next data point is actually at a lower temperature which may seem strange. However, this is a proof that the alloy started to desorb. Desorption is an endothermic process thus, the sample will cool down which is what we saw. Further temperature increase resulted in a lowering of occupancy factor for deuterium, reaching the low value of about 0.3 at 266 °C.

The interpretation of this lowering of deuterium occupancy factor should be discussed. Two different models could be used. The first one is to interpret the lowering of occupancy factor in a true crystallographic matter. It means that the occupancy factor is the fraction of deuterium sites that are occupied. An occupancy factor of 0.4 meaning that 40% of the deuterium sites are occupied. This interpretation has a serious limitation because, if the occupancy factor is less than 1 then it also means that the structure is no longer a true fcc.

The other way to interpret the reduction of occupancy factor is to treat it as a scale factor. It was demonstrated that the scattering factor of the bcc phase is zero and no Bragg's peaks will be seen on the diffraction pattern. This means that, when the fcc desorbs to the bcc phase, the bcc phase does not appear on the diffraction pattern and the pattern will look the same except for the scale factor which decreases. To prevent this, we used the aluminum phase as a benchmark. Obviously, this phase should be constant because the scattering due to the aluminum heater is constant. Therefore, the ratio of the scale factor of the fcc phase over the scale factor of aluminum phase was kept constant. This means that any relative diminution of the amount of fcc phase will be given by a decrease of the deuterium occupancy factor. Therefore, in the present case, the occupancy factor reflects the amount of fcc phase in the sample. Thus, an occupancy factor of 0.4 means that 40% of the original fcc phase remains and 60% desorbed to a bcc phase.

Figure 5.2 (a) also shows the evolution of lattice parameter of the fcc phase with temperature. A slight increase of fcc lattice parameter is seen up to 160 °C. The next few data points are more erratic. This is most likely due to the reduction of temperature at the start of desorption. The lattice parameter seems to slightly drop between 200 °C and 220 °C but raises again at higher temperature. The overall increases of lattice parameter between 122 °C and 266 °C correspond to a linear thermal expansion of $21 \cdot 10^{-6}$ (m/m.K).

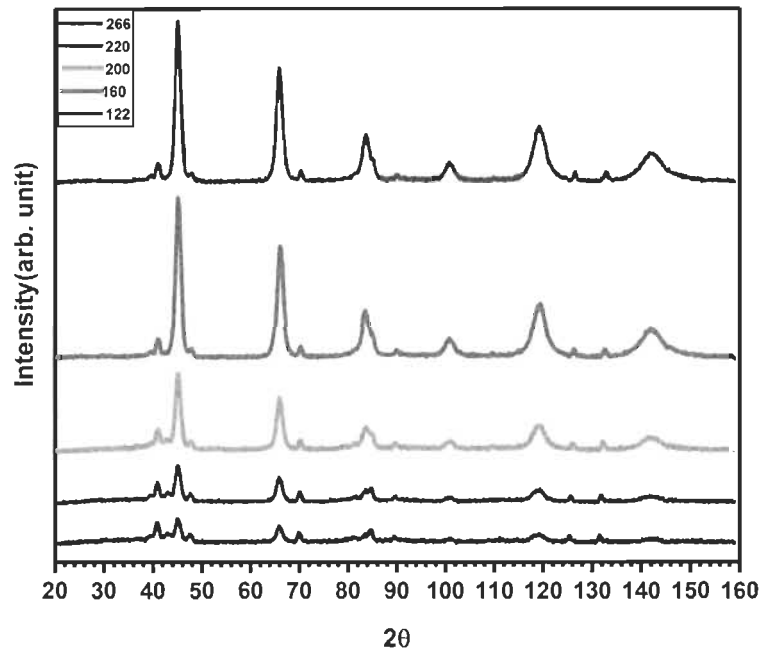


Fig.5.1: Desorption neutron diffraction pattern of fully deuterated $Ti_{50}V_{20}Cr_{30}$ alloy

The validity of linear thermal expansion calculation could be checked with the aluminum phase. Figure 5.2 (b) shows the aluminum lattice parameter versus temperature. From this plot, linear thermal expansion of Al is found to be $29 \cdot 10^{-6}$ (m/m.K). This number is very close to the literature values of 21 to $24 \cdot 10^{-6}$ (m/m.K) [48].

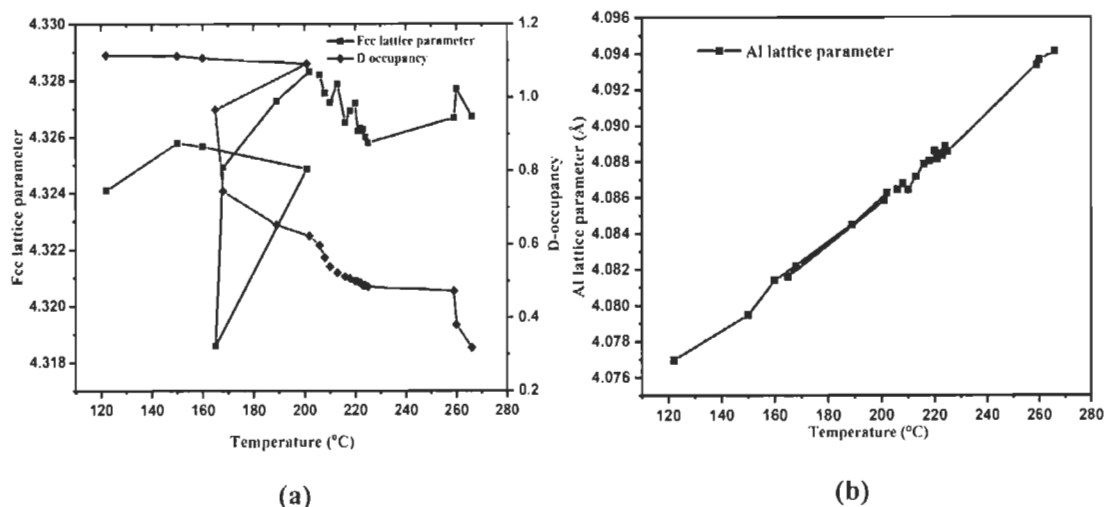


Fig.5.2 Relation between (a) fcc lattice parameter, D-occupancy versus temperature (b) Al cell parameter versus temperature.

Therefore, from in-situ neutron diffraction experiment we were able to measure the fcc phase diminution with temperature and also to estimate the linear thermal expansion of this hydride.

5.3 Results and discussion of 50TiM and 50TiBP

This section describes the morphology and hydrogenation kinetics of $Ti_{49}V_{19.5}Cr_{28.5}Zr_{1.3}Ni_{1.7}$ (50TiM) and $Ti_{46.1}V_{7.2}Cr_{17.4}Zr_{14.7}Ni_{14.6}$ (50TiBP) alloy. As indicated in the introduction of this chapter, these compositions represent respectively the matrix (50TiM) and bright (50TiBP) phases seen in the $Ti_{50}V_{20}Cr_{30}$ alloy. SEM results revealed that, when cast independently, both the alloys were multiphase. These microstructures were compared with the microstructure of $Ti_{50}V_{20}Cr_{30}$ alloy. Alloy 50TiM showed the similar microstructure to $Ti_{50}V_{20}Cr_{30}$ alloy but 50TiBP was found different. Hydrogenation kinetics showed that 50TiBP has faster kinetics than 50TiM but 50TiM showed a higher absorption capacity than 50TiBP. This was expected due to the different chemical composition and phase abundance of these alloys.

This section also gives the information of EXAFS results of 50TiBP. Normalized EXAFS spectra and R-space fitting of as cast and hydride alloy indicated that hydrogen changed the local environment of Ti-atom.

5.3.1 Morphology of 50TiM and 50TiBP

In order to see the morphology of the 50TiM and 50TiBP alloys, SEM analysis has been performed. Fig 5.3 (a-b) shows the morphology of 50TiM and 50TiBP respectively. It can be seen from fig 5.3 (a) that alloy 50TiM is made up by three phases; matrix, bright and black phase. On the other hand, for 50TiBP four phases are observed; matrix phase, bright phase, dark gray and black phase. To obtain the chemical composition of each phase of each alloy, EDS analysis has been done.

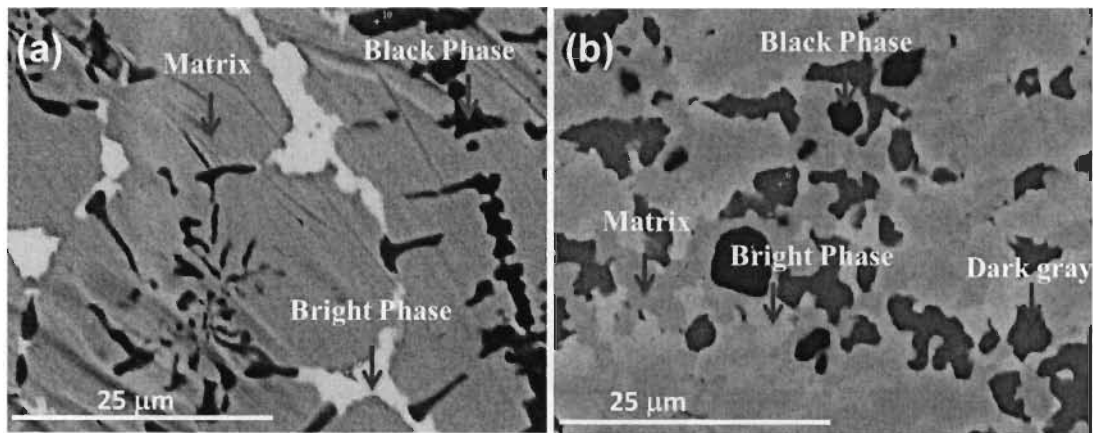


Fig.5.3: Backscattered electron micrographs of 50TiM (a) and 50TiBP (b).

Table 5.2 shows the chemical composition of 50TiM alloy. It is clear from the table that matrix phase of the alloy is very close to the bulk nominal value. Bright phase has high proportion of Zr and Ni compared to the matrix. Black phase of the alloy is Ti-precipitate. Here it can be observed clearly that microstructure and phase composition of 50TiM is very similar to the microstructure and phase composition of $Ti_{50}V_{20}Cr_{30}$, as reported in chapter 1. Both of these alloys have shown the presence of matrix, bright and black phases with similar phase composition.

| Elements | Bulk nominal value | Matrix | Bright phase | Black phase |
|-----------|--------------------|--------|--------------|-------------|
| Ti | 49.3 | 47.6 | 42.6 | 87.4 |
| V | 19.2 | 20.4 | 8.7 | 5 |
| Cr | 28.5 | 29.6 | 26.3 | 5.1 |
| Zr | 1.3 | 1.3 | 13.6 | 2.4 |
| NI | 1.7 | 1.0 | 8.7 | -- |

Table 5.2 Nominal and measured atomic percentage of the 50TiM. Error on the measured values is ± 0.5

Table 5.3 shows the chemical analysis of 50TiBP alloy. Here again, chemical composition of the matrix phase is very close to the bulk nominal value. In the bright phase, except for Ti and Zr, all the elements have similar concentration as seen in the bulk nominal value. Dark gray phase is mainly titanium, the other elements being less than 12% each. Black phase is Ti-precipitate.

Here, microstructure of 50TiBP alloy is found different from $Ti_{50}V_{20}Cr_{30}$ alloy. For 50TiBP, an additional gray phase is seen which was not observed for $Ti_{50}V_{20}Cr_{30}$ alloy. Besides, the microstructure, elemental composition of bright and matrix phases of 50TiBP are also different than the $Ti_{50}V_{20}Cr_{30}$ alloy.

| Element | Bulk nominal value | Matrix phase | Bright phase | Dark gray phase | Black phase |
|---------|--------------------|--------------|--------------|-----------------|-------------|
| Ti | 46.1 | 45.5 | 35.9 | 67.9 | 80.9 |
| V | 7.2 | 5.1 | 7.6 | 8.4 | 1.0 |
| Cr | 17.4 | 12.7 | 19.5 | 12 | -- |
| Zr | 14.4 | 18 | 21.7 | 7.4 | 17.6 |
| Ni | 14.6 | 18.8 | 15.2 | 4.4 | 0.5 |

Table 5.3 Nominal and measured atomic percentage of the 50TiBP. Error on the measured values is ± 0.5

Using imageJ, relative amount of observed phase for 50TiM and 50TiBP was determined and reported in table 5.4. It shows that the matrix phase is by far the most abundant phase for both of these alloys.

| Alloy | Matrix (%) | Bright phase (%) | Dark gray phase(%) | Black phase (%) |
|-------|------------|------------------|--------------------|-----------------|
| 50M | 83(3) | 7(1) | | 9.2(4) |
| 50BP | 70(3) | 12(1) | 12(1) | 5.2(4) |

Table.5.4 Percentage of the observed phases for the alloy 50TiM and 50TiBP, as calculated by Image j. Number in parentheses is the uncertainty on the last significant digit.

5.3.2 First Hydrogenation

First hydrogenation curves of 50TiBP and 50TiM are shown in figure 5.4. It is to be mentioned that both alloys were activated at room temperature without any prior heat treatment. Absorption kinetics of 50TiBP was found to be faster than the 50TiM. A small bump can also be seen in the absorption curve of 50TiBP. Absorption is an exothermic reaction; fast kinetics of the alloy increased the temperature of the sample holder which in turn slightly increased the pressure. When the temperature went back to the nominal value, the pressure decreased and made the capacity decrease. Alloy 50TiM absorbed 3.0 wt.% of hydrogen while 50TiBP could absorb 2.25 wt.%. It can be seen from the table 5.4, that alloy 50TiM have 83% of matrix phase which means that maximum absorption capacity of this alloy is 3.6 wt.% assuming that only matrix phase absorbs hydrogen. For alloy 50TiBP, the matrix phase is 70%, which means that maximum absorption capacity of this alloy is 3.2wt.%. It can be seen here that maximum absorption capacity of both alloys are very close to the value expected if only matrix phase absorbs hydrogen.

The alloy 50TiBP is showing faster kinetics that the alloy 50TiM. This is somewhat expected as we saw in the previous chapters that kinetics is helped by the amount of bright phase. As the alloy 50TiBP was specifically cast to reproduce the bright phase and as the amount of bright phase in this alloy is higher, it is normal that the activation kinetic is faster for this alloy.

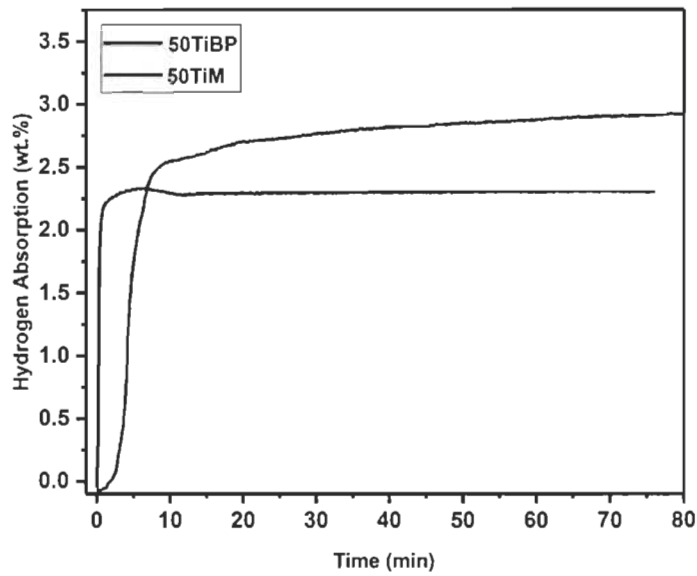


Fig.5.4: Activation curves of the 50TiBP and 50TiM, under 20 bars of hydrogen at 22 °C.

5.3.3 EXAFS

In order to study the local environment of 50TiBP, EXAFS measurements have been performed. Fig.5.5 (a) shows the normalized EXAFS spectra of 50TiBP in the as-cast, hydrided and desorbed state. These measurements have been done at Ti-K edge. Therefore, it is the atomic surroundings of Ti atoms that have been probed.

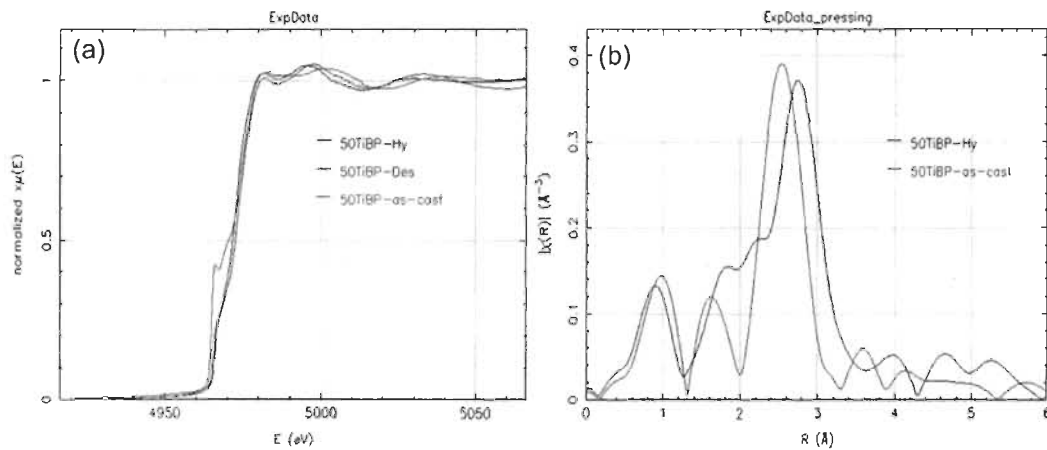


Fig. 5.5: EXAFS spectra at Ti K edge for the 50TiBP in as-cast hydrogenated and desorbed state. (a) Normalized EXAFS spectra (b) R space oscillations.

It can be seen from the figure that the signal obtained for these three samples are different. This indicates that hydrogenation and dehydrogenation affect the electronic structure of Ti-atom. Fig.5.5 (b) shows the R-space fitting of as-cast and hydrogenated samples. Peaks which were observed in as cast sample could not be seen clearly in hydrogenated sample. For the as cast sample first, second, third and fourth peak can be seen clearly but after hydrogenation only first and second peak were found. Second peak which was present in as cast sample disappeared or merged into the third peak after hydrogenation. Besides this, variation in the peak intensities can also be seen. The third peak of the as cast sample is 5 % more intense than the second peak of hydrided sample. The difference in R-space fitting of as-cast and hydrided samples could be due to the difference in coordination shells. After the hydrogenation bond length increases and coordination number decreases. This is the reason why R-space fitting of as-cast and hydrogenated samples are different. Data analysis to calculate the bond length and coordination number before and after hydrogenation is in process.

5.4 Conclusions

In this chapter, neutron study of $\text{Ti}_{50}\text{V}_{20}\text{Cr}_{30}$ alloy has been reported. This study showed that, for this alloy, D occupancy is actually a measure of the fcc abundance in the alloy. From in-situ experiment, it was seen that the alloy started to desorb at 200 °C and at 266

°C only 30% of the fcc phase remained. Linear thermal expansion of hydride phase has been also calculated.

Two compositions representing the matrix and bright phases were prepared by using the elementary composition measured in the microstructure of $\text{Ti}_{50}\text{V}_{20}\text{Cr}_{30}$ alloy. Their compositions were respectively $\text{Ti}_{49}\text{V}_{19.5}\text{Cr}_{28.5}\text{Zr}_{1.3}\text{Ni}_{1.7}$ (50TiM) and $\text{Ti}_{46.1}\text{V}_{7.2}\text{Cr}_{17.4}\text{Zr}_{14.7}\text{Ni}_{14.6}$ (50TiBP). The microstructure of these alloys revealed that these new samples were multiphase instead of single phase as was hoped for.

First hydrogenation curve demonstrated a faster absorption kinetics for the 50TiBP alloy compared to the 50TiM alloy but its total capacity was lower. Higher abundance of bright phase in the 50TiBP explained the faster kinetics. Higher abundance of matrix phase in the 50TiM alloy was the reason for the higher capacity of this alloy.

Effect of hydrogen on atomic structure of 50TiBP alloys has been studied by EXAFS measurements. Normalized EXAFS spectra of 50TiBP at Ti-K-edge showed that hydrogen affects the local structure of Ti-atom. R-space fitting of as cast and hydrogenated samples were found different which could be due to the different coordination number and bond length of these alloys. Detailed neutron and EXAFS data analysis are in process.

Chapter 6

Conclusion and future work

6.1 Conclusion

In this study, the effects of additives on Ti-V-Cr alloys has been studied. The impact of Ti/V ratio has also been investigated. Two types of additives were tested: 7Zr+10Ni and Zr. For both types of additives, the faster first hydrogenation kinetics was attributed to the presence of a secondary phase that was enriched in Zr (and Ni). The additive 7Zr+10Ni gave a much faster first hydrogenation kinetics than the Zr only additive. The reason is a combination of different microstructure and different chemical composition of the secondary phase. It was found that increasing Ti/V ratio enhance the hydrogen capacity. Thus, alloy $Ti_{50}V_{20}Cr_{30}$ was selected for further investigation. In-situ neutron diffraction was used to investigate the change in crystal structure of $Ti_{50}V_{20}Cr_{30}$ alloy during desorption. Despite the fact that the bcc phase of this alloy is essentially transparent to neutron, the decomposition of the fully hydride fcc phase was monitored. Change in lattice parameters and linear thermal expansion of fcc phase was measured for the first time.

To understand the behavior of each individual phase in the multiphase bcc alloys, the matrix and secondary phase of the $Ti_{50}V_{20}Cr_{30} + 7Zr+10Ni$ were cast individually. Their respective composition being $(Ti_{46.1}V_{7.2}Cr_{17.4}Zr_{14.7}Ni_{14.6})$ for the secondary phase and $(Ti_{49}V_{19.5}Cr_{28.5}Zr_{1.3}Ni_{1.7})$ for the matrix. These two alloys were synthesized and the mechanism of these phases was studied individually. It was found that the matrix phase absorbs a high amount of hydrogen and that the secondary phase has higher hydrogenation kinetics thus confirming the hypothesis that the secondary phase acts as a gateway for hydrogen to enter the matrix phase.

Change in the atomic structure of $Ti_{46.1}V_{7.2}Cr_{17.4}Zr_{14.7}Ni_{14.6}$ alloy before and after hydrogenation was studied by EXAFS. It was found that presence of hydrogen atom affect the electronic structure of Ti-atom.

6.2 Future work

The microstructure, phase composition and first hydrogenation of $\text{Ti}_x\text{V}_{70-x}\text{Cr}_{30}$ ($x = 10$ to 50) alloys with additive have been studied. However, to fully understand this system, thermodynamics parameters must be measured. In particular the impact of the additive has to be investigated. In this work, it was found that the chemical composition of the matrix phase do not change much with different additive and thus the thermodynamics parameters are probably very close but this should be confirmed by experiments. Another important practical aspect of metal hydrides is their resistance to hydrogenation/dehydrogenation cycling. A systematic study of cycling behaviour of these alloys should be done. It will be interesting to see the impact of cycling on the microstructure and chemical composition of the matrix and secondary phases.

SECTION B

Articles

1. Dixit V and J Huot, *structural, microstructural and hydrogenation characteristics of Ti-V-Cr alloy with Zr-Ni addition*. Journal of Alloys and compounds, 2018.
2. Dixit V and J Huot, *Investigation of the microstructure, crystal structure and hydrogenation kinetics of Ti-V-Cr alloy with Zr addition*, Journal of Alloys and compounds (submitted).
3. Dixit V, Eijck L and J. Huot, *Neutron study on $Ti_{50}V_{20}Cr_{30}$ alloy*. (Under process)
4. Dixit V and J Huot, *Study of the matrix and bright phase of $Ti_{50}V_{20}Cr_{30}$ alloy*. (Under process).
5. Dixit V, Chen N and J. Huot, *EXAFS study of 50TiBP and 50TiM alloy*. (Under process)

Article 1

Structural, microstructural and hydrogenation characteristics of Ti-V-Cr alloy with Zr-Ni addition

Viney Dixit and Jacques Huot*

Institut de Recherche sur l'Hydrogène, Université du Québec à Trois-Rivières, 3351 des Forges, Trois-Rivières, Québec, Canada

Abstract

In this paper we report the effect of Ti-proportion and addition of Zr-Ni on the crystal structure, morphology and hydrogen storage kinetics of Ti-V-Cr alloy. For this study, five alloys of compositions $Ti_xV_{70-x}Cr_{30}$ ($x = 10, 20, 30, 40, 50$) added with 4 wt.% of 7Zr+10Ni were synthesized. Scanning electron microscopy revealed that all alloys were multiphase. X-ray powder diffraction confirmed that all the as-cast alloys have the body-centred cubic (bcc) phase as the main phase. The same amount of (7Zr+10Ni) was added in all of the alloys, but each alloy has shown a different elemental concentration in their secondary phases. For alloys $x = 10$ and 20 , a Zr rich secondary phase was formed but for alloys $x = 30, 40$ and 50 , the secondary phase has relatively high concentration of all elements.

Upon hydrogenation, the bcc phase transformed into a face-centred cubic (fcc) phase. For $x = 20, 30$ and 40 a body-centred tetragonal (bct) phase was also observed along with fcc phase. Hydrogenation kinetics of all of these alloys was measured and it was found that absorption capacity increased with Ti-content. The maximum absorption capacity of 3.6 wt.% was achieved for $x = 50$.

Keywords: Ti-V-Cr alloy, 7Zr+10Ni, Activation, Crystal structure, Microstructure



Structural, microstructural and hydrogenation characteristics of Ti-V-Cr alloy with Zr-Ni addition

Viney Dixit, Jacques Huot*

Institut de Recherche sur l'Hydrogène, Université du Québec à Trois-Rivières, 3351 des Forges, Trois-Rivières, Québec, Canada

ARTICLE INFO

Article history:

Received 24 July 2018
Received in revised form
19 October 2018
Accepted 22 October 2018
Available online 27 October 2018

Keywords:

Ti-V-Cr alloy
7Zr+10Ni
Activation
Crystal structure
Microstructure
bcc alloys

ABSTRACT

In this paper we report the effect of Ti-proportion and addition of Zr-Ni on the crystal structure, morphology and hydrogen storage kinetics of Ti-V-Cr alloy. For this study, five alloys of compositions $Ti_xV_{70-x}Cr_{30}$ ($x = 10, 20, 30, 40, 50$) added with 4 wt% of 7Zr+10Ni were synthesized. Scanning electron microscopy revealed that all alloys were multiphase. X-ray powder diffraction confirmed that all the as-cast alloys have the body-centred cubic (bcc) phase as the main phase. The same amount of (7Zr+10Ni) was added in all of the alloys, but each alloy has shown a different elemental concentration in their secondary phases. For alloys $x = 10$ and 20, a Zr rich secondary phase was formed but for alloys $x = 30, 40$ and 50, the secondary phase has relatively high concentration of all elements.

Upon hydrogenation, the bcc phase transformed into a face-centred cubic (fcc) phase. For $x = 20, 30$ and 40 a body-centred tetragonal (bct) phase was also observed along with fcc phase. Hydrogenation kinetics of all of these alloys was measured and it was found that absorption capacity increased with Ti-content. The maximum absorption capacity of 3.6 wt% was achieved for $x = 50$.

© 2018 Elsevier B.V. All rights reserved.

1. Introduction

For the full implementation of hydrogen as an energy vector, a safe, low cost and compact hydrogen storage system are required [1]. Beside the well-known gaseous and liquid storage systems, metal hydrides are attractive solution because of their high volumetric density and low operation pressure. Metal hydrides come in a variety of chemical compositions and crystal structures. Some of the most studied are the body centred cubic (bcc) alloys [2]. Ti-V-based bcc alloys are particularly attractive due to their high volumetric storage capacity but these alloys have shown very slow kinetics [3]. Maeland et al. investigated the effect of transition metals: Fe, Mn, Co, Cr and Ni, on Ti-V-based solid solution and observed that addition of a third element improves the hydrogenation kinetics [4,5]. It is reported in literature that Ti-V-Cr alloys with bcc structure have the capacity to absorb up to 3.7 wt% of hydrogen [6]. However, because of the high stability of the monohydride, these alloys show reversible capacity of about 2.4 wt% [6–8].

The first hydrogenation, the so-called activation, of these alloys

is usually slow and heat treatment between 300 °C and 750 °C is required [9–12]. But for commercial applications, this additional step of activation is undesirable. To improve the activation process, Miraglia et al. added Zr₇Ni₁₀ to Ti-V-Cr alloys [13]. They reported that this addition gives rise to a second phase which made the activation possible without prior heat treatment [13]. Bibienne et al. studied the effect of 7Zr+10Ni on Ti-V-Cr alloy and also observed fast kinetics without prior heat treatment [14,15].

Activation kinetics and storage capacity are affected by the differences in chemical composition. The effect of elemental composition on the hydrogenation characteristics of bcc alloys has been the subject of many investigations. It was found that chemical composition has an impact on the plateau pressure and sorption kinetics [15–18].

In this paper we report the investigation on Ti-V-Cr alloys where the Cr content is fixed and only the Ti/V ratio is modified. Effect of the V-content on Ti-V-Cr-Mn alloy has been studied by Yu et al. [19]. They found that a higher concentration of vanadium increased the hydrogen capacity but this made the first hydrogenation much slower, particularly because of a longer incubation time. Since vanadium is expensive compared to Ti, optimizing the Ti/V ratio is attractive for practical applications. A second aim of this study was to investigate the effect of addition of (7Zr + 10Ni) on the activation kinetic. For that purpose, 4 wt% of 7Zr+10Ni was used as an

* Corresponding author.

E-mail address: jacques.huot@uqtr.ca (J. Huot).

additive in all compositions.

1.1. Experimental details

All the elements Ti (99.9%), V (99.7%), Cr (99%), Zr (99.2%) and Ni (99.9) were purchased from Alfa-Aesar and used without further purification. Samples of compositions $Ti_xV_{70-x}Cr_{30}$ ($x = 10, 20, 30, 40, 50$) were all added with 4 wt% of (7Zr + 10Ni). Synthesis was performed by mixing all raw elements and cast them by arc melting. To insure homogeneity, each sample was turned over and remelted 3 times. It should be noted that this method of synthesis is different from the one used by Miraglia et al. [13]. In their case, they synthesized the bcc and Zr_7Ni_{10} alloy separately. Thereafter, these two alloys were mixed in the desired proportion and melted again [13]. Therefore, three melting was necessary for the synthesis of one alloy. In the present work, only one melt was performed because all raw elements were mixed in the desired proportions and melted together. After arc-melting, samples were crushed inside an argon-filled glove box using a hardened stainless-steel mortar and pestle. Hydrogen measurements were performed using a homemade Sievert type apparatus. For the structural and microstructural studies X-ray diffraction pattern (XRD: Bruker D8 Focus: Cu $K\alpha$ radiation) and scanning electron microscope (JEOL JSM-5500) were used. Chemical analyses were performed by EDS (Energy Dispersive Spectroscopy from Oxford Instruments) apparatus attached to the SEM. For the SEM and EDS analysis, all the synthesized samples (pallets) were polished and the smooth surface of the samples was used for the analysis. Crystal structure parameters were evaluated from Rietveld refinement using Topas software [20]. Percentage of secondary phase was calculated from the backscattered micrographs, using the relative areas of each phase as calculated by ImageJ software [21].

2. Result and discussion

2.1. Morphology

Fig. 1 shows the backscattered electron micrograph of the alloys

$Ti_xV_{70-x}Cr_{30}$ where $x = 10, 20, 30, 40, 50$. It is clear from the figure that all these alloys are multiphase and they have different microstructures.

All alloys are made of a gray matrix phase along with a black phase and a bright phase. In the case of $x = 10$ and 20, there is also a small amount of grayish phase. The relative amount and morphology of each of these phases change with x . The area percentage of different phases of $Ti_xV_{70-x}Cr_{30}$ alloy is calculated and reported in Table 1.

It is clear from this table that, in these alloys, there is a predominant phase. This phase will be thereafter called matrix. Other phases, denoted grayish, bright and black are less abundant. In order to study the elemental composition of each phase in each alloy, EDS analysis has been performed on all compositions. Fig. 2 shows the evolution of the chemical composition of the matrix and the bright phase as a function of x . In the case of the matrix phase, it is clear that the abundance of Ti, V, and Cr closely follow the nominal abundance for each composition. The abundance of Zr in the matrix phase is virtually constant at 1.2 ± 0.1 at% while for Ni the abundance is 1.7 ± 0.1 at% with the exception of $x = 30$ where nickel abundance in the matrix phase is 1.1 at%.

The bright phase shows a more complex variation with x . For $x = 10$ and 20, the main element of the bright phase is zirconium. For $x = 10$ the next most abundant element is vanadium while the other three elements constitute less than 10 at.% each. For $x = 20$ zirconium is even more abundant in the bright phase, constituting more than 80% of that phase. The other elements are all less than

Table 1

Percentage of the observed phases for the alloy $Ti_xV_{70-x}Cr_{30}$ ($x = 10$ to 50) with 4 wt% of 7Zr+10Ni as determined by ImageJ. The number in parentheses is the estimated error on the last significant digit based on average over a few measurements.

| Alloy | Grayish Phase (%) | Bright phase (%) | Black Phase (%) | Matrix (%) |
|------------------------|-------------------|------------------|-----------------|------------|
| $Ti_{10}V_{60}Cr_{30}$ | 0.8 (5) | 0.4 (2) | 15 (1) | 83 (2) |
| $Ti_{20}V_{50}Cr_{30}$ | 2.4 (5) | 0.2 (2) | 13 (1) | 85 (2) |
| $Ti_{30}V_{40}Cr_{30}$ | 6 (1) | 9 (1) | 84 (2) | 81 (2) |
| $Ti_{40}V_{30}Cr_{30}$ | 7 (1) | 12 (1) | 81 (2) | 88 (2) |
| $Ti_{50}V_{20}Cr_{30}$ | 4 (1) | 6 (1) | 6 (1) | 88 (2) |

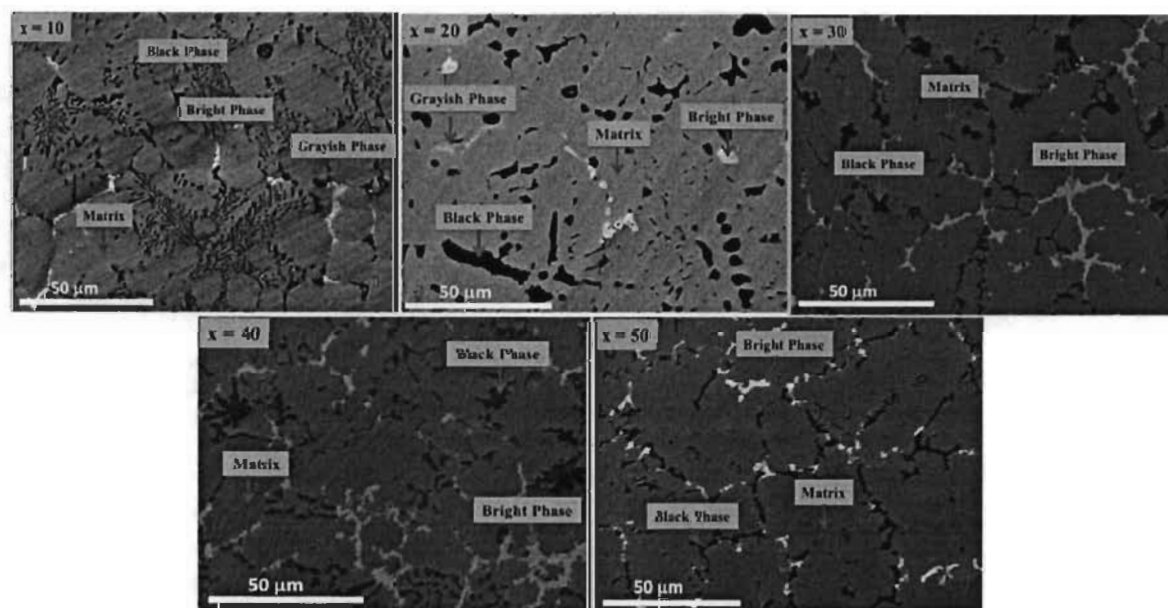


Fig. 1. Backscattered electrons micrograph of the alloys $Ti_xV_{70-x}Cr_{30}$ ($x = 10, 20, 30, 40, 50$), with 4 wt% of 7Zr+10Ni.

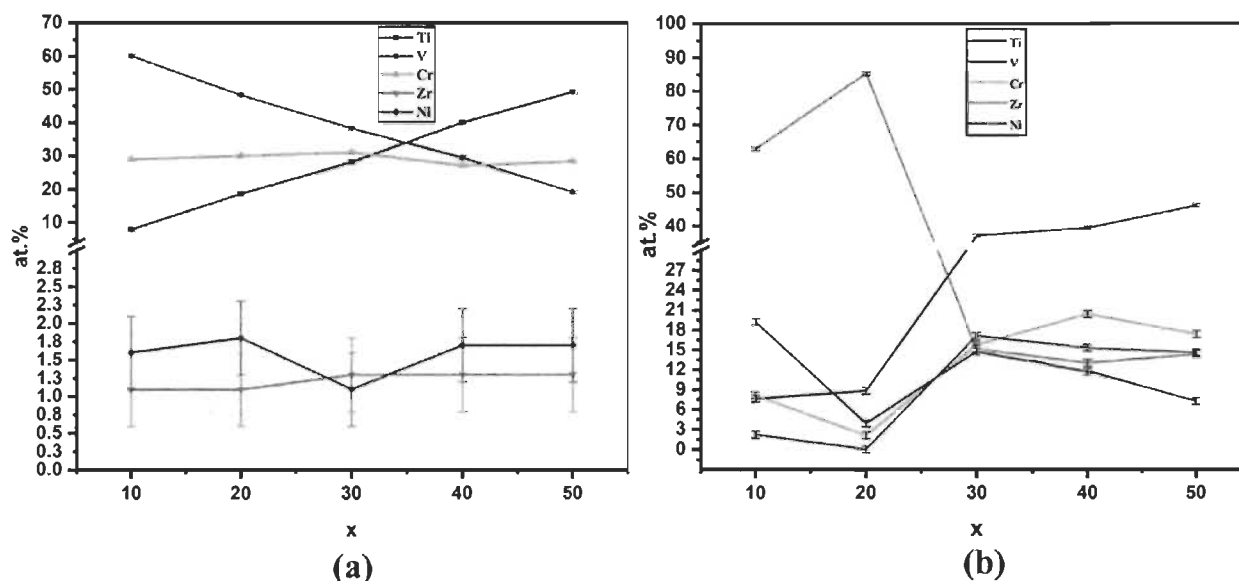


Fig. 2. Chemical analysis of the elements in Matrix (a) and Bright phase (b) with varying Ti concentration.

10% abundant with nickel being totally absent. For $x > 30$ the composition of the bright phase is somewhat more stable with x . Ti is the most abundant element and slowly increases with x , going from 37 at.% for $x = 30$ to 46 at.% for $x = 50$. The abundance of the other elements is more or less constant with the exception of the downward trend of vanadium.

Error on the measured values is ± 0.5 at.%. The other phases seen in the backscattered micrographs were the black phase and the grayish phase. From EDX measurement, it was found that in the black phase Ti was between 78 at.% and 93 at.%. We thus concluded that the black phase is in fact titanium-rich precipitates. As for the grayish phase, it was seen only for $x = 10$ and 20 and the abundance of that phase was very small, respectively 0.8% and 2.4% for $x = 10$ and 20. Table 2 shows the chemical composition of this phase for $x = 10$ and 20.

2.2. Crystal structure

X-ray powder diffraction patterns of the alloys in their as cast and hydrided states are presented in Fig. 3(a and b). Diffraction patterns presented in Fig. 3(a) shows that all the as-cast alloys are body centred cubic (bcc). The patterns of the alloys $x = 30$ and 40 present an additional minor phase. This minor phase is most likely the black phase (Ti rich). Owing to limited number of peaks, crystal structure identification is difficult and will not be further discussed in this paper.

Rietveld refinement was performed on all diffraction patterns. In the case of as-cast alloys, the weighed R-values were between

Table 2

Measured element abundance in at.% of cast Ti_xV_{70-x}Cr₃₀ ($x = 10$ & 20) alloy with 4 wt% of 7Zr+10Ni. Error on measured values is ± 0.5 at.%.

| EDS analysis of grayish phase of Ti _x V _{70-x} Cr ₃₀ ($x = 10$ & 20) alloy | | |
|--|----------|----------|
| Elements | $x = 10$ | $x = 20$ |
| Ti | 32.2 | 29.6 |
| V | 9.3 | 13.4 |
| Cr | 2.9 | 7.8 |
| Zr | 15.4 | 36.4 |
| Ni | 40.2 | 12.8 |

6.61 and 4.9 while the goodness of fit was between 2.43 and 1.57. Lattice parameters and crystallites size as determined by Rietveld refinement for the as-cast alloys are reported in Table 3. This table shows that the lattice parameter is increasing from $x = 10$ to 50 and the crystallite size is roughly constant.

The values reported in Table 3 could be compared with the corresponding ones given in previous investigation on Ti₅₂V₁₂Cr₃₆ and Ti₄₂V₂₁Cr₃₇ [14,15]. It could be seen that the crystallite sizes are practically the same respectively 13.3 (9) nm and 13 (2) nm for on Ti₅₂V₁₂Cr₃₆ and Ti₄₂V₂₁Cr₃₇ [14,15]. However, the microstrains were smaller at respectively 0.12 (3)% and 0.15 (6)%. The reason for the higher microstrain in the present investigation is unclear to us. It may depend on the arc melting power used for casting and also on the cooling rate. Considering the metallic radius of the elements (Ti = 147 pm, V = 136 pm, Cr = 130 pm) it was confirmed that the variation of the lattice parameter is directly proportional to the variation of the average metallic radius.

2.3. First hydrogenation

Fig. 4 shows the first hydrogenation curves of all alloys. It is clear that absorption capacity is increasing and absorption kinetics is getting faster with increasing Ti content. For alloy $x = 10$ and 20 absorption capacity was found to be lower than the other alloys. Alloy $x = 50$ has shown the maximum absorption capacity 3.6 wt% but with a small incubation time.

On the other hand, Ti₄₀V₃₀Cr₃₀ alloy without additive (7Zr+10Ni) could not absorb hydrogen. These results indicate that addition of 7Zr+10Ni improve the kinetics of Ti_xV_{70-x}Cr₃₀ ($x = 10$ to 50) alloys. To understand the crystal structure of hydrided Ti_xV_{70-x}Cr₃₀ ($x = 10$ to 50) alloys, XRD patterns have been taken and are displayed in Fig. 3(b). Crystal structure parameters of each phase seen in the diffraction patterns of hydrided samples were evaluated by Rietveld refinement and are reported in Table 4. The weighed R-values of these patterns were between 5.31 and 3.97 while the goodness of fit was between 1.92 and 1.27.

It is clear from this table that after hydrogenation, the bcc phase is decreasing with x while proportion of fcc phase is increasing. A clear illustration of the change in phases from $x = 10$ to 50 is reported in Fig. 5.

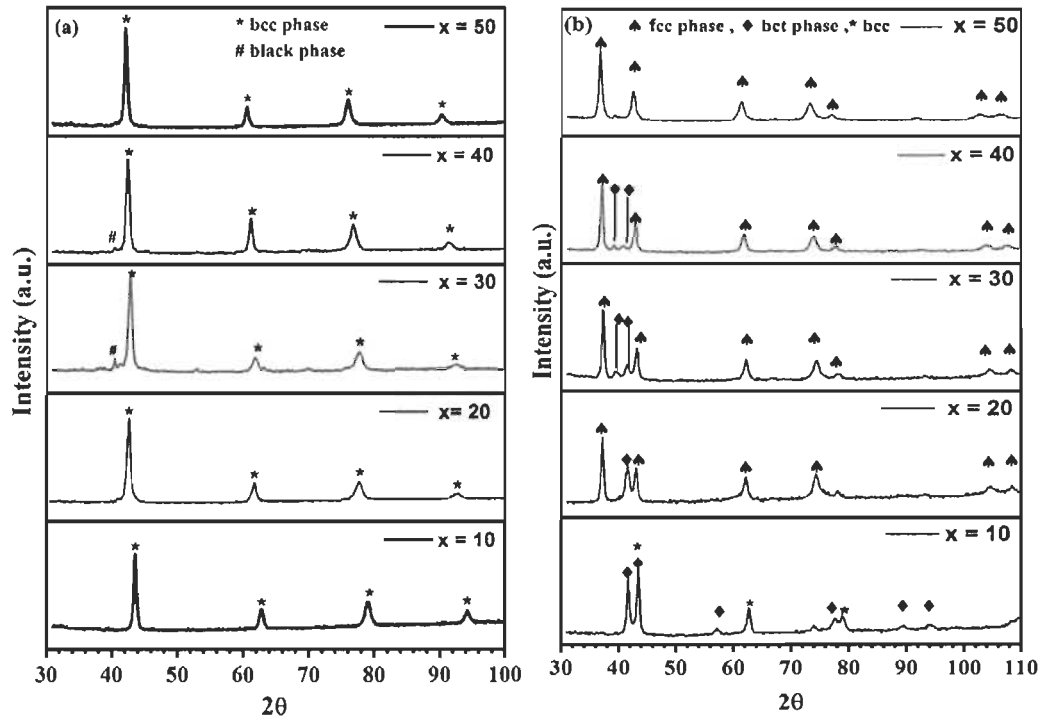


Fig. 3. XRD pattern of the $Ti_xV_{70-x}Cr_{30}$ ($x = 10, 20, 30, 40, 50$) alloys with 4 wt% of 7Zr+10Ni in (a) as cast and (b) hydrided state.

Table 3

Crystal parameters of the $Ti_xV_{70-x}Cr_{30}$ ($x = 10$ to 50 with 4 wt% of 7Zr+10Ni) alloys in as-cast state. The number in parentheses is the error on the last significant digit.

| Alloy | Lattice parameter (Å) | Crystallite Size (nm) | Microstrain (%) |
|------------------------|-----------------------|-----------------------|-----------------|
| $Ti_{10}V_{60}Cr_{30}$ | 3.000 (2) | 18 (1) | 0.43 (9) |
| $Ti_{20}V_{50}Cr_{30}$ | 3.023 (1) | 15.5 (3) | 0.62 (4) |
| $Ti_{30}V_{40}Cr_{30}$ | 3.0376 (7) | 13.0 (5) | 0.19 (1) |
| $Ti_{40}V_{30}Cr_{30}$ | 3.069 (1) | 14.4 (8) | 0.47 (9) |
| $Ti_{50}V_{20}Cr_{30}$ | 3.102 (1) | 15.6 (6) | 0.43 (6) |

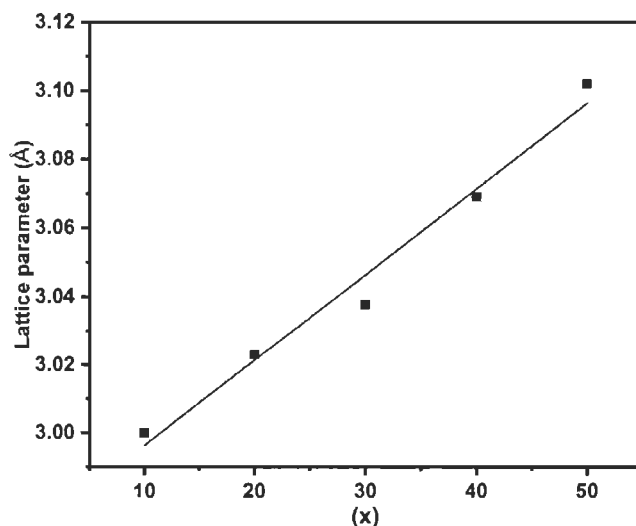


Fig. 4. Activation curve of the $Ti_xV_{70-x}Cr_{30}$ ($x = 10, 20, 30, 40, 50$) alloys with 4 wt% of 7Zr+10Ni and $Ti_{40}V_{30}Cr_{30}$ alloy without 7Zr+10Ni, under 20 bars of hydrogen at 22 °C.

It is clear from this figure that the amount of bct phase decreases with x while concurrently the amount of fcc phase increases. As shown by Nakamura and Akiba, the monohydride of a bcc alloy has a bct structure [22]. The fact that the bct and fcc phases are simultaneously present means that the hydrogenation is not complete. This is consistent with the incomplete activation seen in Fig. 5. Based on the phase abundance found by Rietveld refinement, and knowing the theoretical hydrogen capacity of each phase (bcc = 0 wt%, bct = 2.0 wt% and fcc = 4.0 wt%) we calculated the expected hydrogen capacity from X-ray powder diffraction and compared them to the measured ones. However, we have to take into account that the secondary phases are not apparent in the X-ray diffraction patterns. The reason for this is probably the relatively small proportion of these phases and also the small crystallite size, making the peaks very broad and almost undistinguishable from the background. We are now in the process of taking synchrotron and neutron diffraction patterns of these alloys in the hope of identifying the crystal structure of the secondary phases. Nevertheless, for the present investigation, we have to take into account the identification of the secondary phases the X-ray patterns. Therefore, the theoretical capacities calculated from X-ray patterns were weighed by the fraction of the matrix phase determined by SEM and listed in Table 1. This gives the normalized capacity and it is the capacity that has to be compared to the measured one. The results are given in Table 5.

From this table it can be seen that only in case of alloy $x = 10$, the measure capacity is lower than the calculated one. But the calculated number is quite close to the measured ones, considering the uncertainties.

For other alloys, the measured capacity is slightly higher than the calculated one. This missing capacity is probably due to the absorption of hydrogen by the secondary phases. In fact, the secondary phases are probably acting as a gateway for hydrogen thus making the first hydrogenation (activation) much faster than in the same alloys without addition of Zr-Ni as was shown previously

Table 4

Crystal structure parameters of the $Ti_xV_{70-x}Cr_{30}$ ($x = 10$ to 50) alloy with 4 wt% of 7Zr+10Ni in hydrided state as determined by Rietveld refinement. The number in parentheses is the error on the last significant digit.

| Alloy | Phase | Phase fraction (%) | Lattice parameter (Å) | Crystallite size (nm) | Microstrain (%) |
|------------------------|-------|--------------------|-------------------------|-----------------------|-----------------|
| $Ti_{10}V_{60}Cr_{30}$ | bcc | 28 (3) | 2.9978 (8) | 12.9 (5) | |
| | bct | 72 (3) | 3.0016 (8) 3.258 (1) | 11.8 (3) | |
| $Ti_{20}V_{50}Cr_{30}$ | fcc | 61 (2) | 4.3346 (8) | 18.0 (1) | 0.15 (1) |
| | bct | 39 (2) | 3.149 (1) 3.092 (2) | 7.2 (3) | |
| $Ti_{30}V_{40}Cr_{30}$ | fcc | 79 (2) | 4.281 (1) | 24 (2) | 0.19 (1) |
| | bct | 21 (2) | 3.2701 (1) 3.040 (2) | 12.7 (1) | |
| $Ti_{40}V_{30}Cr_{30}$ | fcc | 91 (2) | 4.3008 (8) | 17.0 (8) | 0.222 (7) |
| | bct | 9.0 (8) | 3.316 (1) 3.071 (2) | 19 (2) | |
| $Ti_{50}V_{20}Cr_{30}$ | fcc | 100.0 | 4.3346 (8) | 12.0 (5) | 0.312 (8) |

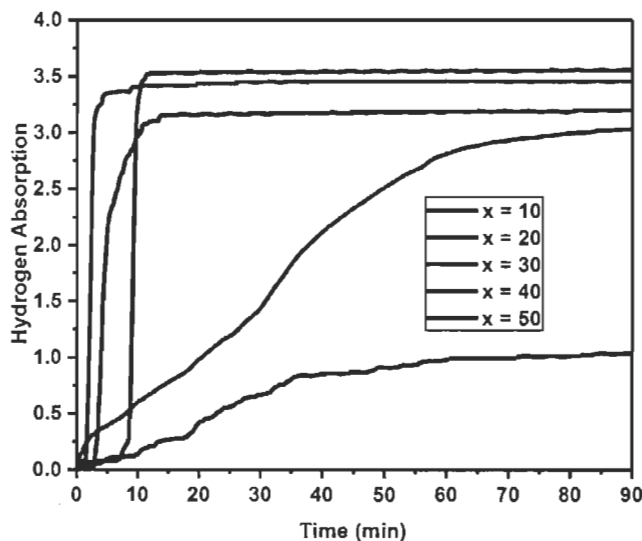


Fig. 5. Illustration of the phase change of $Ti_xV_{70-x}Cr_{30}$ alloy from $x = 10$ to 50.

Table 5

Comparison between the expected and measured absorption capacities of $Ti_xV_{70-x}Cr_{30}$ ($x = 10$ to 50) alloys. The number in parentheses is the uncertainties on the last significant digit.

| Alloy (x) | Phase | Phase abundance | Phase capacity (wt.%) | Total calculated capacity from X-ray pattern | Normalized weight capacity (wt.%) | Measured capacity (wt.%) |
|-----------|-------|-----------------|-----------------------|--|-----------------------------------|--------------------------|
| 10 | bcc | 28 (3) | 0.0 | 1.4 (1) | 1.2 (1) | 1.0 |
| | bct | 72 (3) | 1.4 | | | |
| 20 | fcc | 61 (2) | 2.4 | 3.2 (1) | 2.7 (1) | 3.0 |
| | bct | 39 (2) | 0.8 | | | |
| 30 | fcc | 79 (2) | 3.2 | 3.6 (1) | 3.0 (1) | 3.2 |
| | bct | 21 (2) | 0.4 | | | |
| 40 | fcc | 91 (2) | 3.6 | 3.8 (1) | 3.1 (2) | 3.4 |
| | bct | 9.0 (8) | 0.2 | | | |
| 50 | fcc | 100.0 | 4.0 | 4.0 | 3.5 (1) | 3.6 |

[14,15]. For confirmation of this hypothesis, the change in crystal structure upon hydrogenation should be investigated using in-situ X-ray diffraction. In the present case, we used 'post-mortem' X-ray diffraction but there is always the possibility that the alloy partially desorbed between the time it was quenched and the time it was measured by X-ray diffraction. An in-situ experiment will give us the true phase change during hydrogenation.

3. Conclusion

The microstructure and first hydrogenation behaviour of alloys of composition $Ti_xV_{70-x}Cr_{30}$ ($x = 10, 20, 30, 40, 50$) to which 4 wt% of 7Zr+10Ni was added was investigated. All alloys consisted of a main bcc phase with secondary phases. However, the microstructure was totally different from one alloy to the other.

Absorption curves show that alloys, $x = 10$ and 20 with Zr rich phase have slow kinetics and small hydrogen capacities. Alloys with $x = 30$ and 40 have faster kinetics and higher capacities. In the case of $x = 50$, an incubation time was present in the first hydrogenation curve, contrary to the other compositions where absorption starts readily. This may be because of the different microstructure and elemental composition of this alloy. Hydrided samples have shown the presence of different phases. For alloy $x = 10$, bcc phase was found with bct phase. The hydrides of alloys with $x = 20, 30$ and 40 presented bct and fcc phases but for alloy $x = 50$ only fcc phase was present.

From this study we conclude that increasing Ti concentration improve storage capacity and addition of 7Zr+10Ni improves the first hydrogenation kinetics. Investigation of the thermodynamics of these alloys is now underway and will provide essential information for a better understanding of the hydrogenation of these alloys.

Acknowledgement

We would like to acknowledge the Canadian Government and Queen Elizabeth II Diamond Jubilee Scholarship for the Ph.D. fellowship. VD would like to thank her parents, Mr. & Mrs. S. Dixit, and her sister Isha, for their moral support.

References

- [1] T. Bibienne, et al., Ti-based BCC alloy: dehydrogenation characterization using synchrotron and neutron diffraction, *Mater. Res.* 19 (2016) 8–12.
- [2] H. Iba, E. Akiba, The relation between microstructure and hydrogen absorbing property in Laves phase-solid solution multiphase alloys, *J. Alloys Compd.* 231 (1) (1995) 508–512.
- [3] S.F. Santos, J. Huot, Hydrogen storage in Ti–Mn–(FeV) BCC alloys, *J. Alloys Compd.* 480 (1) (2009) 5–8.
- [4] A.J. Maeland, G.G. Libowitz, J.P. Lynch, Hydride formation rates of titanium-based b.c.c. solid solution alloys, *J. Less Common Met.* 104 (2) (1984) 361–364.
- [5] A.J. Maeland, et al., Hydride formation rates of B.C.C. group V metals, *J. Less Common Met.* 104 (1) (1984) 133–139.
- [6] G. Mazzolai, et al., Hydrogen-storage capacities and H diffusion in bcc TiVCr alloys, *J. Alloys Compd.* 466 (1) (2008) 133–139.
- [7] S. Ono, K. Nomura, Y. Ikeda, The reaction of hydrogen with alloys of vanadium and titanium, *J. Less Common Met.* 72 (2) (1980) 159–165.
- [8] T. Tamura, et al., Effects of protide structures on hysteresis in Ti–Cr–V protium absorption alloys, *Mater. Trans.* 43 (11) (2002) 2753–2756.
- [9] J.-H. Yoo, et al., Influence of Mn or Mn plus Fe on the hydrogen storage

- properties of the Ti-Cr-V alloy. *Int. J. Hydrogen Energy* 34 (22) (2009) 9116–9121.
- [10] H.C. Lin, et al., Cyclic hydrogen absorption–desorption characteristics of TiCrV and Ti_{0.8}Cr_{1.2}V alloys. *Int. J. Hydrogen Energy* 32 (18) (2007) 4966–4972.
- [11] S.-W. Cho, et al., Hydrogen isotope effects in Ti_{1.0}Mn_{0.9}V_{1.1} and Ti_{1.0}Cr_{1.5}V_{1.7} alloys. *J. Alloys Compd.* 297 (1) (2000) 253–260.
- [12] S.-i. Towata, et al., Effect of partial niobium and iron substitution on short-term cycle durability of hydrogen storage Ti–Cr–V alloys. *Int. J. Hydrogen Energy* 38 (7) (2013) 3024–3029.
- [13] S. Miraglia, et al., Hydrogen sorption properties of compounds based on BCC Ti_{1-x}V_{1-y}Cr_{1+x+y} alloys. *J. Alloys Compd.* 536 (2012) 1–6.
- [14] T. Bibienne, J.-L. Bobet, J. Huot, Crystal structure and hydrogen storage properties of body centred cubic 52Ti–12V–36Cr alloy doped with Zr₇Ni₁₀. *J. Alloys Compd.* 607 (2014) 251–257.
- [15] T. Bibienne, et al., Synthesis, characterization and hydrogen sorption properties of a Body Centered Cubic 42Ti–21V–37Cr alloy doped with Zr₇Ni₁₀. *J. Alloys Compd.* 620 (2015) 101–108.
- [16] E. Akiba, H. Iba, Hydrogen absorption by laves phase related BCC solid solution. *Intermetallics* 6 (6) (1998) 461–470.
- [17] T. Tamura, et al., Protium absorption properties of Ti–Cr–V alloys in low hydrogen pressure regions. *Mater. Trans.* 42 (9) (2001) 1862–1865.
- [18] K. Young, D. Wong, L. Wang, Effect of Ti/Cr content on the microstructures and hydrogen storage properties of Laves phase-related body-centred-cubic solid solution alloys. *J. Alloys Compd.* 622 (2015) 885–893.
- [19] X.B. Yu, et al., Enhancement of hydrogen storage capacity of Ti–V–Cr–Mn BCC phase alloys. *J. Alloys Compd.* 372 (1) (2004) 272–277.
- [20] A. Coelho, Topas-academic: a Computer Programme for Rietveld Analysis, 2004.
- [21] T. Collins. Image J for microscopy. *Biotechniques* 43 (2007) S25–S30.
- [22] Y. Nakamura, E. Akiba, Hydriding properties and crystal structure of NaCl-type mono-hydrides formed from Ti–V–Mn BCC solid solutions. *J. Alloys Compd.* 345 (1–2) (2002) 175–182.

The image shows a blue rectangular banner with the text "Clicours.COM" in white, bold, sans-serif font. The banner is positioned at the bottom of the page.

Article 2

Investigation of the microstructure, crystal structure and hydrogenation kinetics of Ti-V-Cr alloy with Zr addition

Viney Dixit, Jacques Huot

Institut de Recherche sur l'Hydrogène, Université du Québec à Trois-Rivières, 3351 des Forges, Trois-Rivières, Québec, Canada

Abstract

The effect of 4 wt.% Zr as additive in $\text{Ti}_x\text{V}_{70-x}\text{Cr}_{30}$ ($x = 10$ to 50) alloy has been investigated. After casting, all of these alloy were multiphase but with different microstructure and phase composition. From X-ray diffraction, bcc structure of all as-cast alloys was confirmed along with zirconium-rich secondary phases. For alloy $x= 30$ and 40 , a Ti and a Ti-Zr high pressure-high temperature phase were observed along with the bcc phase. Upon hydrogenation, bcc phase transformed to a body centered tetragonal and a face centered cubic phase. Only alloy $x=40$, has shown a complete hydrogenation. For $x= 20$ and 30 , a bct phase was seen along with the bcc and fcc phase. The first hydrogenation kinetics of Zr added alloys were found to be faster than without additive but not as fast as with $7\text{Zr} + 10\text{Ni}$ additive. It was also found that the volume taken by the hydrogen atom in the fcc phase decreases with increasing value of the bcc lattice parameter.

Keywords: Bcc alloy, Activation, Zr, Microstructure, Crystal structure

Investigation of the microstructure, crystal structure and hydrogenation kinetics of Ti-V-Cr alloy with Zr addition

Viney Dixit, Jacques Huot

*Institut de Recherche sur l'Hydrogène, Université du Québec à Trois-Rivières, 3351 des Forges,
Trois-Rivières, Québec, Canada*

Abstract

The effect of 4 wt.% Zr as additive in $Ti_xV_{70-x}Cr_{30}$ ($x = 10$ to 50) alloy has been investigated. After casting, all of these alloys were multiphase but with different microstructure and phase composition. From X-ray diffraction, bcc structure of all as-cast alloys was confirmed. For alloys $x=30$ and 40, a Ti and a Ti-Zr high pressure-high temperature phase were observed along with the bcc phase. Upon hydrogenation, bcc phase transformed to a body centred tetragonal and a face centred cubic phase. Only alloy $x=40$, has shown a complete hydrogenation. For $x=20$ and 30, a bct phase was seen along with the bcc and fcc phase. The first hydrogenation kinetics of Zr added alloys were found to be faster than without additive but not as fast as with 7Zr + 10 Ni additive. It was also found that the volume taken by the hydrogen atom in the fcc phase decreases with increasing value of the bcc lattice parameter.

Keywords: Bcc alloy, Activation, Zr, Microstructure, Crystal structure

1 Introduction

Hydrogen is considered as a sustainable and reliable energy carrier but, to use it commercially, hydrogen production and storage methods must be optimized [1-3]. There are several ways to store hydrogen, the main ones being liquefaction, compression and solid state [1, 4-6]. For solid state hydrogen storage, metal hydrides have attracted considerable attention of researchers because of their high volumetric storage capacity and relatively low operating hydrogen pressure [4, 7]. Amongst the variety of metal hydrides, Ti-V-Cr alloys with body centred cubic structure (bcc) have been extensively studied [8-14]. Their maximum storage capacity at room temperature is 3.7 wt.% which is relatively high [4]. However, the reversible capacity is much lower due to the low plateau pressure of the monohydride. Although these alloys have relatively high absorption capacity at room temperature, they usually show long incubation time during the

first hydrogenation [15-18]. Tsukahara et al. studied the V-based multiphase alloys for Ni-metal hydride batteries and observed the combined effect of the presence of two phases: bcc solid solution phase and C14 Laves phase [19-22]. They found the presence of two phases to be very helpful to improve the battery's reaction rate. Iba and Akiba also reported that bcc solid solution phase with Laves phase is quite promising for hydrogen absorption [23]. Recently, Miraglia et al. showed that by adding Zr_7Ni_{10} to Ti-V-Cr alloy, a Zr and Ni rich secondary phase was found in the as-cast alloy. This secondary phase was responsible for the fast activation kinetics [12].

In a previous work, we have added 4 wt.% of 7Zr+10Ni to $Ti_xV_{70-x}Cr_{30}$ ($x = 10$ to 50) alloys and found fast activation kinetics for all of these alloys [24]. Investigation of the microstructure indicated that the secondary phase was Zr and Ni-rich [24]. This motivated us to use Zr, as an additive for the same compositions and compare it with the previously used additive (7Zr+10Ni).

2 Experimental

All the raw elements Ti (99.9%), V (99.7%), Cr (99%) and Zr (99.2%) were purchased from Alfa-Aesar. Five alloys of composition $Ti_xV_{70-x}Cr_{30}$ ($x = 10$ to 50), to which 4 wt.% of Zr was added, were synthesized by arc melting. In each synthesis, the raw elements were all mixed together in the desired proportion and melted. The sample was remelted and turned over three times in order to get a homogeneous alloy.

Crystal structure of each alloy in as cast and hydrided state were studied by X-ray powder diffraction on a Bruker D8 Focus using Cu $K\alpha$ radiation. Scanning electron microscope (SEM) (JEOL JSM-5500) was used to study the microstructure of the as-cast alloys. For chemical analyses, EDS (Energy Dispersive Spectroscopy) apparatus from Oxford Instruments was utilized. Percentage of relative area of secondary phases were calculated by using the Imagej software [25]. Topas software was used for Rietveld's refinement of the crystal structure parameters [26]. The hydrogenation kinetics was measured at room temperature under 20 bars of hydrogen using a homemade Sieverts type apparatus.

3 Results and Discussion

3.1 Morphology

Backscattered electron micrographs of the as-cast alloys $Ti_xV_{70-x}Cr_{30}$ ($x = 10, 20, 30, 40, 50$), added with 4 wt.% of Zr, are presented in figure 1.

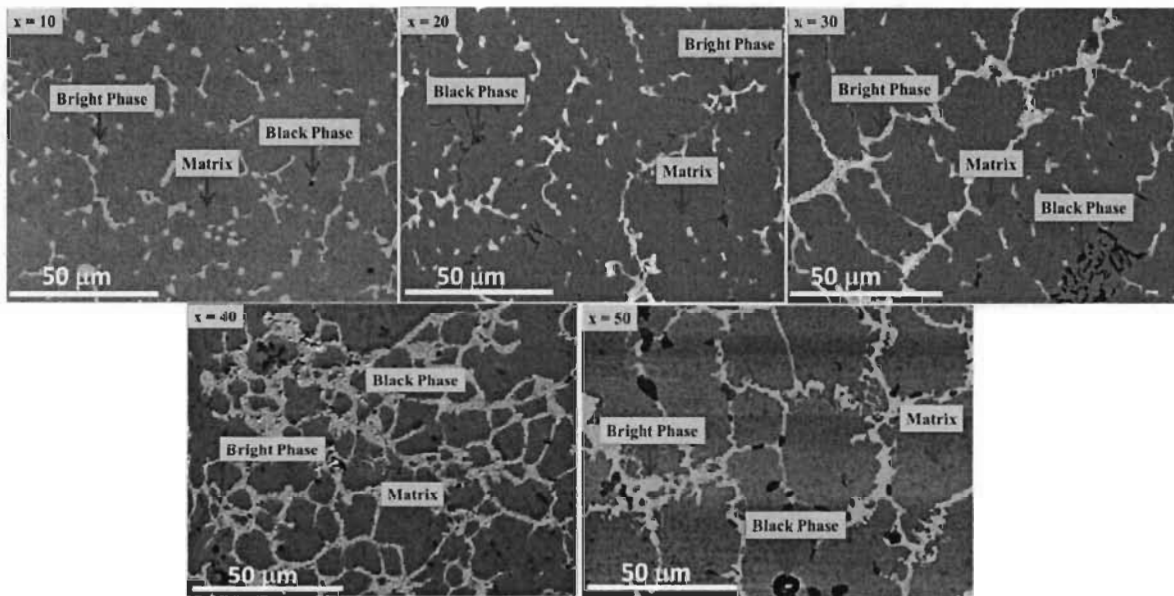


Fig.1: Higher magnification backscattered electrons micrograph of the alloys $Ti_xV_{70-x}Cr_{30}$ ($x = 10, 20, 30, 40, 50$), added with 4 wt.% of Zr.

It is seen from figure 1 that all of these alloys are made up of a matrix, a bright phase and a black phase. The abundance of these phases seems to vary with composition. At the lower magnification, for $x = 10$ and 20 the microstructure was found homogeneous but for the other alloys it was inhomogeneous with regions having more secondary phase than others. The reason for this behaviour is most probably variation of cooling rates within the ingot. For the clear vision of multiphase, only higher magnification microstructure has been shown. This inhomogeneity makes the estimation of relative amount of each phase more difficult. Using ImageJ, the relative amount of each phase was estimated and is reported in Table 1.

| Alloy | Matrix (%) | Bright phase (%) | Black phase (%) |
|---|------------|------------------|-----------------|
| Ti ₁₀ V ₆₀ Cr ₃₀ | 91.4 | 8.3 | -- |
| Ti ₂₀ V ₅₀ Cr ₃₀ | 92.1 | 7.8 | -- |
| Ti ₃₀ V ₄₀ Cr ₃₀ | 86.2/77.5 | 9.05/7.5 | 15.2/5.4 |
| Ti ₄₀ V ₃₀ Cr ₃₀ | 89.7/85.4 | 13.2/7.1 | 2.8/1.1 |
| Ti ₅₀ V ₂₀ Cr ₃₀ | 86.9/84.7 | 11.7/6.6 | 5.9/3.3 |

Table 1: Percentage of the observed phases for the alloy Ti_xV_{70-x}Cr₃₀ (x= 10 to 50) added with 4 wt.% of Zr, as determined by imagej. Error on the measured values is ±0.5 at.%. For inhomogeneous distribution of phases, the higher/lower values are indicated.

As seen from the table 1, the matrix phase dominates for all alloys. Black phase distribution is quite inhomogeneous this is the reason the range proportion is so high.

To measure the elemental composition of these phases, EDS analysis have been performed. The results for the matrix and bright phases are represented in figure 2(a) and 2(b) respectively. It is seen that in the matrix phase, the elements concentrations are very close to the nominal values for Ti, V, and Cr. In the case of zirconium, the abundance is practically constant with x, varying between 1.3 and 2.3 at.%.

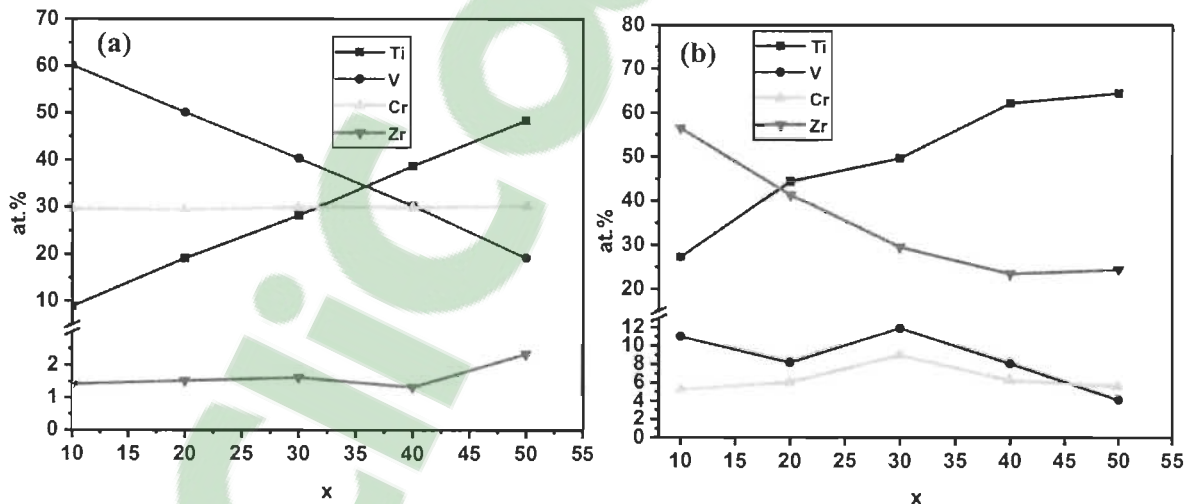


Fig.2. Proportion of elements, in at.%, as a function of x in the matrix (a) and bright phase (b).

Regarding the bright phase, Ti and Zr are the main elements of that phase but their abundance greatly change with x. Vanadium and chromium are in much smaller proportion and varies much less with x than Ti and Zr.

The black phase is essentially a titanium precipitation for all composition. The abundance of titanium in that phase varies between 78.3 at% and 84.9 at%. The second most abundant element in the black phase is zirconium and its abundance fluctuate between 7.5 at.% to 17.3 at.%. The other two elements are present in proportions less than 5 at.%.

3.2 Crystal Structure

X-ray diffraction patterns of $Ti_xV_{70-x}Cr_{30}$ alloy in as-cast state are shown in figure 3(a). It is clear from the figure that all the as-cast alloys have body centred cubic (bcc) phase. Apart from the bcc phase, two additional minor phases were also observed for alloy $x = 30$ and 40 . Analysis of the patterns showed that one phase is titanium and the other phase is a high-temperature-high-pressure Ti-Zr phase. Comparing with the SEM results and the chemical compositions measured by EDS, it is clear that the Ti phase (S.G. $P6_3/mmc$) corresponds to the black phase seen in the backscattered images while the high-temperature-high-pressure Ti-Zr phase (S.G. $P6/mmm$) is the bright phase.

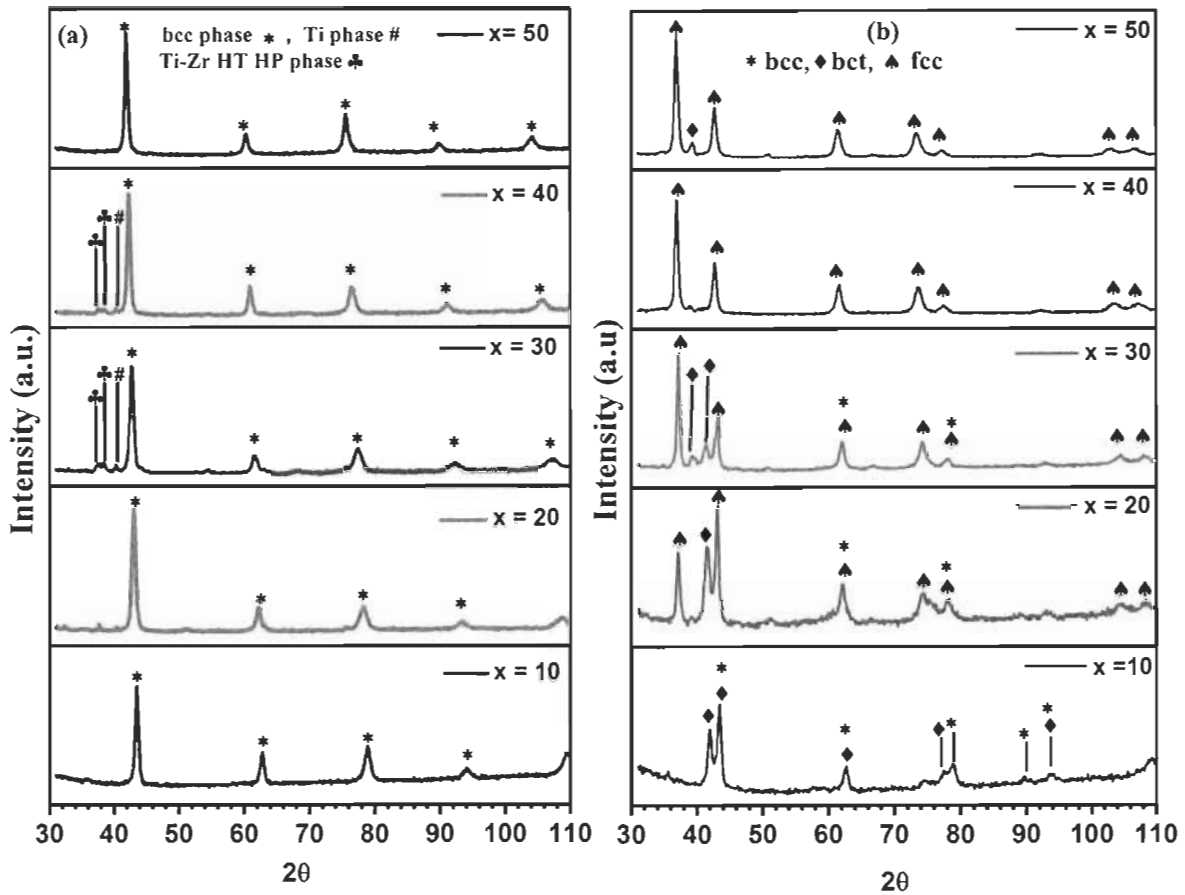


Fig.3 XRD pattern of $Ti_xV_{70-x}Cr_{30}$ ($x = 10$ to 50) alloys added with 4 wt.% of Zr in (a) as cast and (b) hydride state.

Lattice parameters, phase abundances and crystallite sizes for each alloy were evaluated by Rietveld's refinement and are reported in table 2. This table indicates that bcc crystallite size is constant for $x = 10$ to 50 while lattice parameter is increasing from $3.0032(4) \text{ \AA}$ to $3.1142(4) \text{ \AA}$. For all patterns, the microstrain parameter was found to be zero within experimental error.

| Alloy | Phase | Phase Abundance (%) | Lattice Parameter (Å) | Crystallite size (nm) |
|--------|----------------|---------------------|-----------------------|-----------------------|
| x = 10 | bcc | 100 | 3.0032(4) | 17.1(7) |
| x = 20 | bcc | 100 | 3.0170(6) | 18.0(8) |
| x=30 | bcc | 88.7(6) | 3.0460(5) | 15.3(5) |
| | Ti | 1.6(2) | 2.981(1) | 32.1(6) |
| | | | 4.800(4) | |
| | Ti-Zr HP HT | 9.7(5) | 4.783(3) 3.034(3) | 8.2(7) |
| x = 40 | bcc | 92.4(5) | 3.0795(4) | 17.7(5) |
| | Ti | 2.4(3) | 2.986(3) | 7.6(1) |
| | | | 4.83(1) | |
| | Ti-Zr HP HT | 5.1(4) | 4.769(3) 3.030(4) | 9.5(1) |
| x = 50 | bcc | 100 | 3.1142(4) | 15.0(4) |

Table 2: Crystal parameters of $Ti_xV_{70-x}Cr_{30}$ ($x = 10$ to 50) alloy added with 4 wt.% of Zr. Number in the parenthesis is the error on the last significant digit.

A linear relationship between the lattice parameter of the bcc phase and Ti content is evident from figure 4, where lattice parameter and average atomic radii are plotted as a function of x . The direct relationship between the average atomic radius and the lattice parameter is clear.

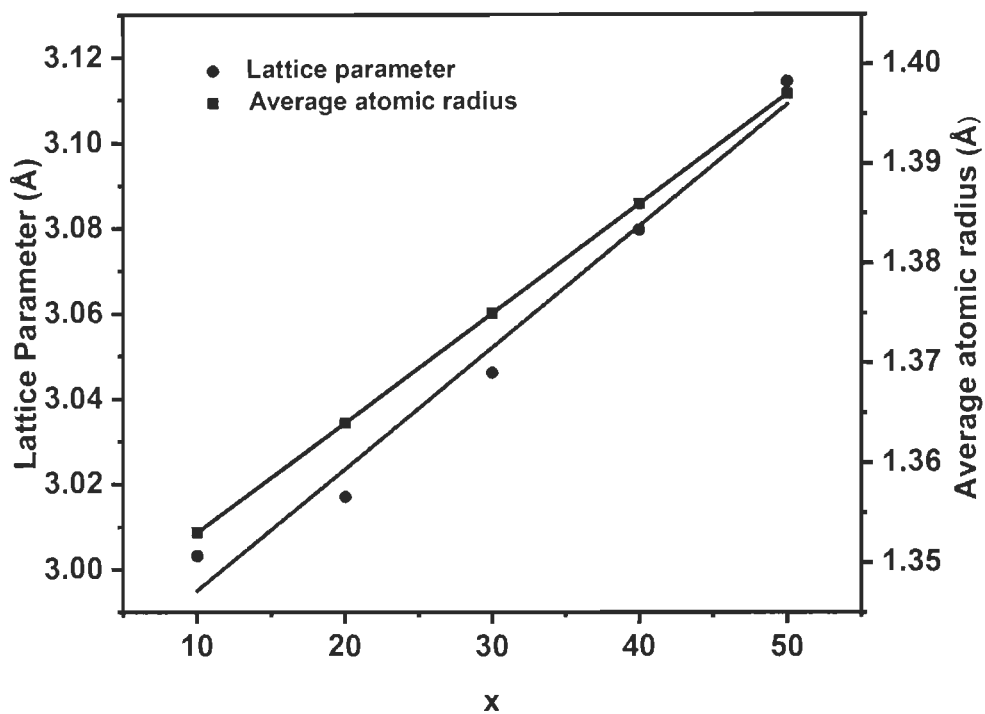


Fig.4: Lattice parameter and average atomic radius of bcc phase as a function of Ti-content (x).

3.3 First Hydrogenation

First hydrogenation (activation) curves of the $Ti_xV_{70-x}Cr_{30}$ ($x= 10, 20, 30, 40, 50$) alloys are presented in figure 5. These measurements were done at room temperature under 20 bar pressure without any prior heat treatment of the alloys. As seen from the curves, absorption capacity increases with higher x values. For alloy $x = 50$, maximum absorption capacity of 3.7 wt.% is achieved. However, for $x = 50$ a long incubation time was also observed.

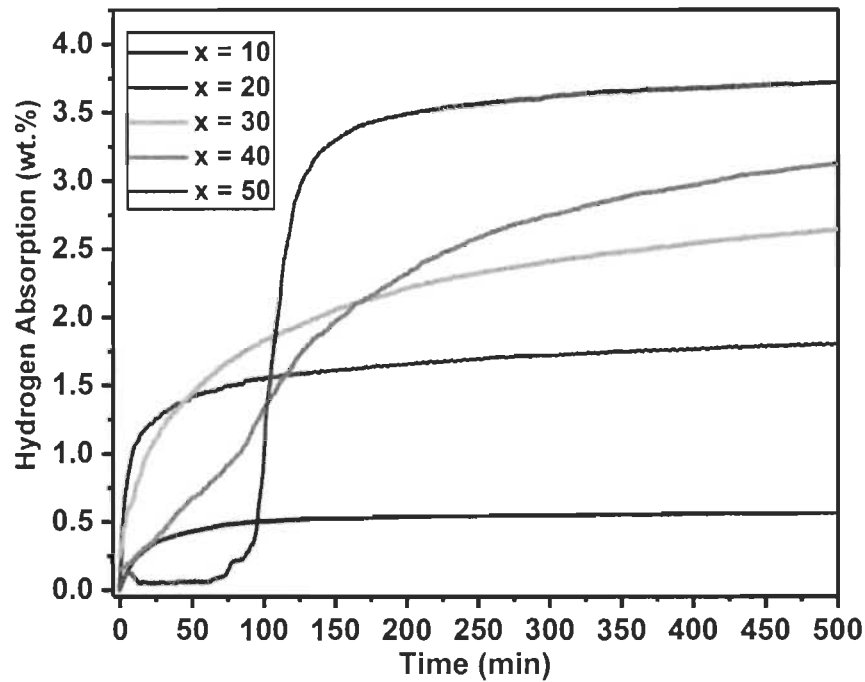


Fig.5. Activation curve of the $Ti_xV_{70-x}Cr_{30}$ ($x = 10, 20, 30, 40, 50$) alloys added with 4 wt.% of Zr, under 20 bars of hydrogen at 22 °C

In order to study the crystal structure of these hydrided alloys, X-ray diffraction have been performed on the fully hydrided samples and are displayed in figure 3(b). XRD pattern shows that except for $x = 40$, all the hydrided alloys have more than one phase. The phases present were bcc (S.G. Im-3m), body centred tetragonal (bct, S.G. I4/mmm), and face centred cubic (fcc, S.G. Fm-3m). Lattice parameters and phase analysis of all hydrided alloys were evaluated by Rietveld's refinement and are presented in table 3. As for the as-cast case, for all patterns the microstrain parameter was found to be zero within the experimental error.

| Alloy | Phase | Phase Abundance (%) | Lattice Parameter (Å) | Unit cell volume (Å ³) | Crystallite size (nm) |
|-------|-------|---------------------|------------------------|------------------------------------|-----------------------|
| 10 | bcc | 37(3) | 3.0031(8) | 27.08(2) | 12.0(5) |
| | bct | 63(3) | 3.0140(1) 3.2126(2) | 29.18(3) | 7.5(3) |
| 20 | bcc | 26 (2) | 3.0233(8) | 27.63 | 10.6(5) |
| | bct | 36 (2) | 3.0971(1) 3.175(2) | 30.46(4) | 18(3) |
| | fcc | 37 (1) | 4.2712(1) | 77.90(8) | 19(3) |
| 30 | bcc | 18 (1) | 3.1379(1) | 30.90(4) | 7.6 (5) |
| | bct | 15(1) | 3.155(5) 3.455(8) | 34.40(14) | 5.9(6) |
| | fcc | 67 (2) | 4.2821(9) | 78.52(5) | 19 (1) |
| 40 | fcc | 100 | 4.3067(8) | 79.88(5) | 13.3 (5) |
| 50 | bct | 6.8(5) | 3.301(2) 3.361(4) | 36.62(7) | 12(1) |
| | fcc | 93.2 (5) | 4.3287(7) | 81.11(4) | 15.2 (5) |

Table 3: Crystal parameter of $Ti_xV_{70-x}Cr_{30}$ ($x = 10$ to 50) alloy added with 4 wt.% of Zr in hydride state. Numbers in parentheses is the error on the last significant digit.

For alloy $x = 10$, we see that the hydride consists of a bcc phase (with the same lattice parameter as in the as-cast state (see table 2)) and a bct phase. It is well known that the monohydride of a bcc phase is a bct phase [27]. However, in the present case, the expansion of the lattice, compared to the as-cast bcc, is quite small: only 1.05 \AA^3 per unit cell. Usually, the volume occupied by a hydrogen atom in the lattice is between 2 \AA^3 and 3 \AA^3 . This means that only between 0.5 and 0.35 hydrogen atom is absorbed by formula unit which is not the characteristic of a monohydride. Moreover, from the activation measurement, the measured capacity was only 0.5 wt.%. Considering that 63% of the alloy is bct this means that the true capacity of this bct phase is about 0.8 wt.%. As the nominal capacity of the monohydride is 2 wt.% this means that only 0.4 hydrogen atom instead of 1 was absorbed by the bct phase. This number agrees well with the ones derived from the diffraction patterns. Therefore, we could conclude that, for this alloy, because of the small lattice parameter of the bcc phase, it is very difficult for hydrogen to go into the bcc solid solution phase and when it does it forms a bct phase but with a stoichiometry much smaller than a monohydride.

For alloy $x = 20$, bcc and bct phase are seen along with face centred cubic phase (fcc). In this case after hydrogenation lattice expansion of bcc and bct phase, compared to the as-cast bcc was found to be very small: 0.19 \AA^3 and 1.5 \AA^3 respectively. This indicates that for bcc and bct phase hydrogen atom absorbed by formula unit is 0.06 and 0.5 respectively. Here again it is seen that bct phase is not a true monohydride phase. On the other hand, lattice expansion for fcc phase is 5.74 \AA^3 which means hydrogen atom absorbed by formula unit are 2. This is the characteristics of a dihydride phase. Considering the phase abundance (bcc = 26 wt.%, bct = 36 wt.%, fcc = 37 wt.%) and nominal hydrogen capacity of each phase (bct = 2 wt.%, fcc = 4 wt.%), the total absorption capacity calculated from the X-ray diffraction pattern of the alloy is 1.87 wt.% which is very close to the measured one. However, from a thermodynamics point of view, having a bcc, bct, and fcc simultaneously is not possible. This is most probably due to slow diffusion of hydrogen through the fcc and bct phases. This means that, upon hydrogenation, a 'shell' of fcc phase forms and, as diffusion is slow through this phase, the hydrogen could not reach the bct and bcc phase in the 'core'. This is a classic explanation for the incomplete hydrogenation in many metal hydrides.

For alloy $x = 30$ and 50 , from the lattice expansions, we determined that one hydrogen atom was absorbed in bct phase and two were absorbed in the fcc phase. This indicates that for these alloys

bcc phase was a true monohydride and fcc phase was a dihydride. Alloy $x = 40$ was a complete dihydride without any bcc or bct phases.

Figure 6 shows the increase of unit cell volume per hydrogen atom ($\Delta H/V$) in fcc phase as a function of x . The volume change was deduced from the difference in unit cell volume of the bcc phase before hydrogenation and the fcc phase after hydrogenation. It is clear from the figure that the unit cell volume per hydrogen atom in the fcc phase decreases with x . This result is somewhat counterintuitive. As shown in figure 4, the lattice parameter of the bcc phase increases with x . Therefore, the interstitial sites available for hydrogen will be bigger as x increases. For a bigger interstitial site, the volume increases to accommodate a hydrogen in the fcc structure will be less. Therefore, in the fully hydride state (fcc phase) the change of volume due to the inclusion of hydrogen is smaller as x increases. To our knowledge this is the first time such behaviour is seen. Similar investigation on other bcc alloys should be performed in order to validate this result.

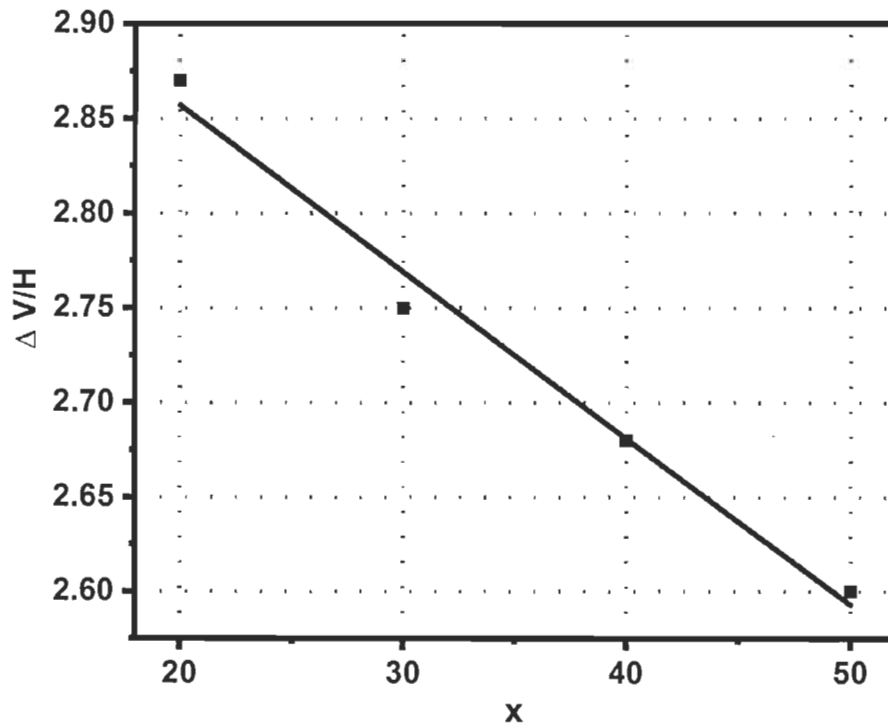


Fig 6: Increase of unit cell volume per hydrogen atom for $Ti_xV_{70-x}Cr_{30}$ ($x = 20$ to 50) alloys.

3.4 Comparison between Zr and 7Zr+10Ni additive

In a previous investigation, the effect of adding 7Zr+10Ni to $Ti_xV_{70-x}Cr_{30}$ ($x = 10$ to 50) alloy has been studied [24]. A comparison of activation kinetics of alloys added with Zr and with 7Zr+10Ni additives is presented in figure 7. As a reference, $x = 40$ composition was synthesized without any additive. It is seen from the figure that the alloy without additive did not absorb hydrogen. On the other hand, the same composition with additives (Zr and 7Zr+10Ni) could absorb hydrogen. This means that additive make activation possible at room temperature. Besides this, it is clearly seen that the alloys with 7Zr+10Ni present a very fast kinetics compared to the alloys with Zr. For both additive, the hydrogen capacity increases with the Ti-content but, for a given Ti-content, the capacity is higher with 7Zr+10Ni additive than with Zr additive. Incubation time is longer with Zr additive and the kinetics are also slower compared to 7Zr+10Ni additive. Therefore, it could be concluded that the 7Zr+10Ni additive is much better than Zr additive for the $Ti_xV_{70-x}Cr_{30}$ alloys. Difference in absorption kinetics and capacities of Zr and 7Zr+10Ni added alloys could be due to their different microstructure and difference in chemical composition of the secondary phases [24]. Alloys added with 7Zr+10Ni, has shown Zr-Ni rich secondary phase, and alloy added with Zr has a Zr rich secondary phase. Abundance of the secondary phase for 7Zr+10Ni alloys was found between 0.2 % and 7 %. However, for Zr added alloys it was found between 6.6 % and 13.2%. Even though Zr added alloy has a high percentage of secondary phase compared to 7Zr+10Ni alloy, still it has slow kinetics. This indicates that the combined effect of Zr-Ni is more beneficial for fast absorption than Zr alone and that the chemical composition of the secondary phase plays a crucial role in the activation kinetics.

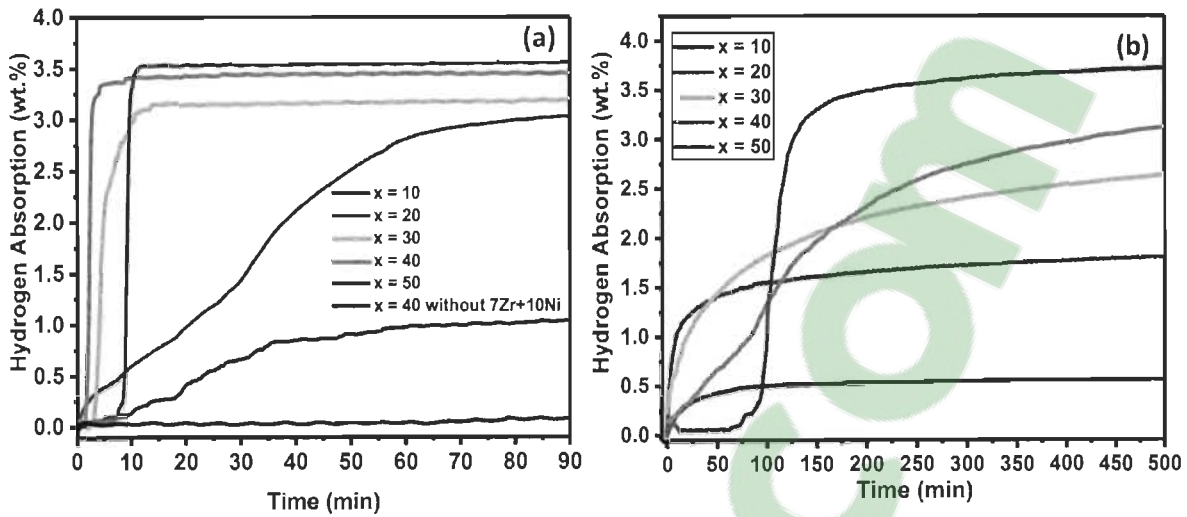


Fig.7: First hydrogenation kinetics of $Ti_xV_{70-x}Cr_{30}$ alloy (a) with 4wt.% of 7Zr+10Ni and $Ti_{40}V_{30}Cr_{30}$ alloy without additive (b) with 4 wt.% of Zr , under 20 bars of hydrogen at 22 °C

4 Conclusions

The main findings of the present investigation are as follows:

Adding 4 wt.% of Zr to five different composition of $Ti_xV_{70-x}Cr_{30}$ ($x= 10$ to 50) alloy has been realized. All alloys presented a multiphase microstructure. X-ray diffraction confirmed that all as cast alloys had a main phase which was bcc but for alloys $x = 30$ and 40, a Ti and HT-HP Ti-Zr phase was also observed along with bcc.

The hydrogenation curves shown that absorption capacity of the alloys increased with increasing x value which was also confirmed by XRD pattern of hydrided alloys. Alloys $x = 10$ and 20, showed the presence of bct phase which was not a true monohydride phase. For $x = 30$ and 50, a complete monohydride phase was seen. The alloy $x = 40$, showed a single fcc phase.

These results indicated that increasing Ti content was beneficial to achieve higher absorption capacity. This study also demonstrated a linear relationship between the bcc lattice parameter and the change of volume in the fcc phase. Volume variation of the fcc phase due to hydrogenation linearly decreased with increasing bcc lattice parameter.

Comparison of Zr additive with 7Zr+10Ni additive demonstrated that the latter is more effective for the enhancement of first hydrogenation. The reason for this discrepancy is probably the different microstructure and secondary phase chemical composition. Therefore, it is concluded that 7Zr+10Ni is better than Zr as additive for $Ti_xV_{70-x}Cr_{30}$ ($x= 10$ to 50) alloys

Acknowledgement

Authors would like to acknowledge the Canadian government and Queen Elizabeth II Diamond Jubilee Scholarship for the Ph.D. fellowship. VD would like to thank her parents and sister for their moral support.

References:

1. Momirlan, M. and T.N. Veziroglu, *The properties of hydrogen as fuel tomorrow in sustainable energy system for a cleaner planet*. International Journal of Hydrogen Energy, 2005. **30**(7): p. 795-802.
2. Zhevago, N., *Other methods for the physical storage of hydrogen*, in *Compendium of Hydrogen Energy*. 2015, Elsevier. p. 189-218.
3. Schlapbach, L. and A. Zuttel, *Hydrogen-storage materials for mobile applications*, in *Materials for sustainable energy: a collection of peer-reviewed research and review articles from nature publishing group*. 2011, World Scientific. p. 265-270.
4. Lin, H.C., et al., *Cyclic hydrogen absorption-desorption characteristics of TiCrV and Ti_{0.8}Cr_{1.2}V alloys*. International Journal of Hydrogen Energy, 2007. **32**(18): p. 4966-4972.
5. Wang, H., et al., *Tuning kinetics and thermodynamics of hydrogen storage in light metal element based systems—a review of recent progress*. Journal of Alloys and Compounds, 2016. **658**: p. 280-300.
6. Kumar, S. and N. Krishnamurthy, *Variation of activation energy of hydrogen absorption of vanadium as a function of aluminum*. International Journal of Hydrogen Energy, 2012. **37**(18): p. 13429-13436.
7. Kumar, S., et al., *Cyclic hydrogen storage properties of VTiCrAl alloy*. International Journal of Hydrogen Energy, 2018. **43**(14): p. 7096-7101.
8. Bibienne, T., J.-L. Bobet, and J. Huot, *Crystal structure and hydrogen storage properties of body centered cubic 52Ti–12V–36Cr alloy doped with Zr₇Ni₁₀*. Journal of Alloys and Compounds, 2014. **607**: p. 251-257.
9. Bibienne, T., et al., *Ti-based BCC Alloy: Dehydrogenation Characterization Using Synchrotron and Neutron Diffraction*. Materials Research, 2016. **19**: p. 8-12.
10. Bibienne, T., et al., *Synthesis, characterization and hydrogen sorption properties of a Body Centered Cubic 42Ti–21V–37Cr alloy doped with Zr₇Ni₁₀*. Journal of Alloys and Compounds, 2015. **620**: p. 101-108.

11. Mazzolai, G., et al., *Hydrogen-storage capacities and H diffusion in bcc TiVCr alloys*. Journal of Alloys and Compounds, 2008. **466**(1-2): p. 133-139.
12. Miraglia, S., et al., *Hydrogen sorption properties of compounds based on BCC $Ti_{1-x}V_{1-y}Cr_{1+x+y}$ alloys*. Journal of Alloys and Compounds, 2012. **536**: p. 1-6.
13. Tamura, T., et al., *Protium absorption properties of Ti-Cr-V alloys in low hydrogen pressure regions*. Materials transactions, 2001. **42**(9): p. 1862-1865.
14. Tamura, T., et al., *Effects of protide structures on hysteresis in Ti-Cr-V protium absorption alloys*. Materials Transactions, 2002. **43**(11): p. 2753-2756.
15. Yoo, J.-H., et al., *Influence of Mn or Mn plus Fe on the hydrogen storage properties of the Ti-Cr-V alloy*. International journal of hydrogen energy, 2009. **34**(22): p. 9116-9121.
16. Lin, H., et al., *Cyclic hydrogen absorption-desorption characteristics of TiCrV and Ti_{0.8}Cr_{1.2}V alloys*. International Journal of Hydrogen Energy, 2007. **32**(18): p. 4966-4972.
17. Cho, S.-W., et al., *Hydrogen isotope effects in Ti_{1.0}Mn_{0.9}V_{1.1} and Ti_{1.0}Cr_{1.5}V_{1.7} alloys*. Journal of Alloys and Compounds, 2000. **297**(1): p. 253-260.
18. Towata, S.-i., et al., *Effect of partial niobium and iron substitution on short-term cycle durability of hydrogen storage Ti-Cr-V alloys*. International Journal of Hydrogen Energy, 2013. **38**(7): p. 3024-3029.
19. Tsukahara, M., et al., *Phase structure of V-based solid solutions containing Ti and Ni and their hydrogen absorption-desorption properties*. Journal of alloys and compounds, 1995. **224**(1): p. 162-167.
20. Rönnebro, E., et al., *Structural studies of a new Laves phase alloy (Hf, Ti)(Ni, V)₂ and its very stable hydride*. Journal of alloys and compounds, 1995. **231**(1-2): p. 90-94.
21. Tsukahara, M., et al., *V-based solid solution alloys with Laves phase network: hydrogen absorption properties and microstructure*. Journal of alloys and compounds, 1996. **236**(1-2): p. 151-155.
22. Tsukahara, M., et al., *Vanadium-based solid solution alloys with three-dimensional network structure for high capacity metal hydride electrodes*. Journal of alloys and compounds, 1997. **253**: p. 583-586.
23. Akiba, E. and H. Iba, *Hydrogen absorption by Laves phase related BCC solid solution*. Intermetallics, 1998. **6**(6): p. 461-470.

24. Dixit, V. and J. Huot, *Structural, microstructural and hydrogenation characteristics of Ti-V-Cr alloy with Zr-Ni addition*. Journal of Alloys and Compounds, 2018. **776**: p. 614-619.
25. Collins, T., *Image J for Microscopy*. BioTechniques, 43, S25-S30. 2007.
26. Coelho, A., *TOPAS-Academic; A Computer Programme for Rietveld Analysis*. 2004.
27. Nakamura, Y., et al., *Crystal structure of two hydrides formed from a Ti-V-Mn BCC solid solution alloy studied by time-of-flight neutron powder diffraction—a NaCl structure and a CaF₂ structure*. Journal of alloys and compounds, 2001. **316**(1-2): p. 284-289.

REFERENCES:

1. Momirlan, M. and T.N. Veziroglu, *The properties of hydrogen as fuel tomorrow in sustainable energy system for a cleaner planet*. International Journal of Hydrogen Energy, 2005. **30**(7): p. 795-802.
2. Rusman, N. and M. Dahari, *A review on the current progress of metal hydrides material for solid-state hydrogen storage applications*. International Journal of Hydrogen Energy, 2016. **41**(28): p. 12108-12126.
3. Züttel, A., A. Borgschulte, and L. Schlapbach, *Hydrogen as a future energy carrier*. 2011: John Wiley & Sons.
4. Ouyang, L., et al., *Excellent hydrolysis performances of Mg₃RE hydrides*. International Journal of Hydrogen Energy, 2013. **38**(7): p. 2973-2978.
5. Elshout, R., *HYDROGEN PRODUCTION BY STEAM REFORMING*. Chemical Engineerinh, 2010.
6. Principi, G., et al., *The problem of solid state hydrogen storage*. Energy, 2009. **34**(12): p. 2087-2091.
7. Bowman, R.C. and B. Fultz, *Metallic hydrides I: hydrogen storage and other gas-phase applications*. MRS bulletin, 2002. **27**(9): p. 688-693.
8. Sandrock, G. and R.C. Bowman Jr, *Gas-based hydride applications: recent progress and future needs*. Journal of Alloys and Compounds, 2003. **356**: p. 794-799.
9. Schlapbach, L., *Hydrogen in intermetallic compounds II. Surface and dynamic properties, applications, Vol. 67 of Topics in Applied Physics*. 1992, Springer-Verlag.
10. Hirose, K., *Handbook of hydrogen storage: new materials for future energy storage*. 2010: John Wiley & Sons.
11. Ivey, D.G. and D.O. Northwood, *Storing energy in metal hydrides: a review of the physical metallurgy*. Journal of Materials Science, 1983. **18**(2): p. 321-347.
12. Broom, D.P., *Hydrogen storage materials: the characterisation of their storage properties*. 2011: Springer Science & Business Media.
13. Cho, S.-W., et al., *Hydrogen absorption-desorption properties of Ti_{0.32}Cr_{0.43}V_{0.25} alloy*. Journal of Alloys and Compounds, 2007. **430**(1-2): p. 136-141.

14. Seo, C.-Y., et al., *Hydrogen storage properties of vanadium-based bcc solid solution metal hydrides*. Journal of Alloys and Compounds, 2003. **348**(1-2): p. 252-257.
15. Song, X., et al., *The influence of alloy elements on the hydrogen storage properties in vanadium-based solid solution alloys*. Journal of Alloys and Compounds, 2008. **455**(1-2): p. 392-397.
16. Mazzolai, G., et al., *Hydrogen-storage capacities and H diffusion in bcc TiVCr alloys*. Journal of Alloys and Compounds, 2008. **466**(1-2): p. 133-139.
17. Wang, J.-Y., *Comparison of hydrogen storage properties of Ti₀. 37V₀. 38Mn₀. 25 alloys prepared by mechanical alloying and vacuum arc melting*. International Journal of Hydrogen Energy, 2009. **34**(9): p. 3771-3777.
18. Ono, S., K. Nomura, and Y. Ikeda, *The reaction of hydrogen with alloys of vanadium and titanium*. Journal of the Less Common Metals, 1980. **72**(2): p. 159-165.
19. Akiba, E. and H. Iba, *Hydrogen absorption by Laves phase related BCC solid solution*. Intermetallics, 1998. **6**(6): p. 461-470.
20. Maeland, A.J., et al., *Hydride formation rates of B.C.C. group V metals*. Journal of the Less Common Metals, 1984. **104**(1): p. 133-139.
21. Maeland, A.J., G.G. Libowitz, and J.P. Lynch, *Hydride formation rates of titanium-based b.c.c. solid solution alloys*. Journal of the Less Common Metals, 1984. **104**(2): p. 361-364.
22. Manchester, F., *Phase Diagrams of Binary Hydrogen Alloys; Monograph Series on Alloy Phase Diagrams, 13; ASM International: Materials Park, OH, USA, 2000*. There is no corresponding record for this reference.
23. Miraglia, S., et al., *Hydrogen sorption properties of compounds based on BCC Ti_{1-x}V_{1-y}Cr_{1+x+y} alloys*. Journal of Alloys and Compounds, 2012. **536**: p. 1-6.
24. Yoo, J.-H., et al., *Influence of Mn or Mn plus Fe on the hydrogen storage properties of the Ti-Cr-V alloy*. International Journal of Hydrogen Energy, 2009. **34**(22): p. 9116-9121.

25. Lin, H., et al., *Cyclic hydrogen absorption–desorption characteristics of TiCrV and Ti_{0.8}Cr_{1.2}V alloys*. International Journal of Hydrogen Energy, 2007. **32**(18): p. 4966-4972.
26. Tsukahara, M., et al., *Phase structure of V-based solid solutions containing Ti and Ni and their hydrogen absorption-desorption properties*. Journal of Alloys and Compounds, 1995. **224**(1): p. 162-167.
27. Rönnebro, E., et al., *Structural studies of a new Laves phase alloy (Hf, Ti)(Ni, V)₂ and its very stable hydride*. Journal of Alloys and Compounds, 1995. **231**(1-2): p. 90-94.
28. Tsukahara, M., et al., *V-based solid solution alloys with Laves phase network: hydrogen absorption properties and microstructure*. Journal of Alloys and Compounds, 1996. **236**(1-2): p. 151-155.
29. Tsukahara, M., et al., *Vanadium-based solid solution alloys with three-dimensional network structure for high capacity metal hydride electrodes*. Journal of Alloys and Compounds, 1997. **253**: p. 583-586.
30. Mazzolai, G., et al., *Hydrogen-storage capacities and H diffusion in bcc TiVCr alloys*. Vol. 466. 2008. 133-139.
31. Tamura, T., et al., *Effects of protide structures on hysteresis in Ti-Cr-V protium absorption alloys*. Materials Transactions, 2002. **43**(11): p. 2753-2756.
32. Bibienne, T., et al., *Synthesis, characterization and hydrogen sorption properties of a Body Centered Cubic 42Ti–21V–37Cr alloy doped with Zr₇Ni₁₀*. Journal of Alloys and Compounds, 2015. **620**: p. 101-108.
33. Young, K., D. Wong, and L. Wang, *Effect of Ti/Cr content on the microstructures and hydrogen storage properties of Laves phase-related body-centered-cubic solid solution alloys*. Journal of Alloys and Compounds, 2015. **622**: p. 885-893.
34. Yu, X.B., et al., *Enhancement of hydrogen storage capacity of Ti–V–Cr–Mn BCC phase alloys*. Journal of Alloys and Compounds, 2004. **372**(1): p. 272-277.
35. Coelho, A., *TOPAS-Academic; A Computer Programme for Rietveld Analysis*. 2004.
36. <https://en.wikipedia.org/wiki/Diffractometer>.

37. Beiser, A., *Concepts of modern physics*. 2003: Tata McGraw-Hill Education.
38. S.J.B.Reed, *Electron microscopy analysis and scanning electron microscopy in geology*. second ed. 2005.
39. Ressler, T., *WinXAS: A new software package not only for the analysis of energy-dispersive XAS data*. Le Journal de Physique IV, 1997. 7(C2): p. C2-269-C2-270.
40. Xu, G., et al., *Non-patchy strategy for inter-atomic distances from Extended X-ray Absorption Fine Structure*. Scientific Reports, 2017. 7: p. 42143.
41. Calvin, S., *XAFS for Everyone*. 2013: CRC press.
42. McCleverty, J.A. and T.J. Meyer, *Comprehensive coordination chemistry II- From biology to nanotechnology*. Elsevier Vol. 2. 2003.
43. Blach, T.P. and E.M. Gray, *Sieverts apparatus and methodology for accurate determination of hydrogen uptake by light-atom hosts*. Journal of Alloys and Compounds, 2007. **446-447**: p. 692-697.
44. Toby, B.H. and R.B. Von Dreele, *What's new in GSAS-II*. Powder Diffraction, 2014. **29**(S2): p. S2-S6.
45. Fritzsche, H., J. Huot, and D. Fruchart, *Neutron scattering and other nuclear technique for hydrogen in materials*. 2016.
46. Nakamura, Y., et al., *Crystal structure of two hydrides formed from a Ti-V-Mn BCC solid solution alloy studied by time-of-flight neutron powder diffraction—a NaCl structure and a CaF₂ structure*. Journal of Alloys and Compounds, 2001. **316**(1-2): p. 284-289.
47. Dixit, V. and J. Huot, *Structural, microstructural and hydrogenation characteristics of Ti-V-Cr alloy with Zr-Ni addition*. Journal of Alloys and Compounds, 2018.
48. https://www.engineeringtoolbox.com/linear-expansion-coefficients-d_95.html.